



HAL
open science

Internal waves and mean flow in the presence of topography

Keshav Jayakrishnan Raja

► **To cite this version:**

Keshav Jayakrishnan Raja. Internal waves and mean flow in the presence of topography. Earth Sciences. Université Grenoble Alpes, 2018. English. NNT : 2018GREAU006 . tel-01799047

HAL Id: tel-01799047

<https://theses.hal.science/tel-01799047v1>

Submitted on 24 May 2018

HAL is a multi-disciplinary open access archive for the deposit and dissemination of scientific research documents, whether they are published or not. The documents may come from teaching and research institutions in France or abroad, or from public or private research centers.

L'archive ouverte pluridisciplinaire **HAL**, est destinée au dépôt et à la diffusion de documents scientifiques de niveau recherche, publiés ou non, émanant des établissements d'enseignement et de recherche français ou étrangers, des laboratoires publics ou privés.

THÈSE

Pour obtenir le grade de

DOCTEUR DE L'UNIVERSITÉ GRENOBLE ALPES

Spécialité : Sciences de la Terre et de l'Univers et
de l'Environnement (CESTUE)

Arrêté ministériel : 25 Mai 2016

Présentée par

Keshav Jayakrishnan RAJA

Thèse dirigée par **Joël SOMMERIA**, Directeur de Recherche, CNRS

préparée au sein :

Laboratoire des Écoulements Géophysiques et Industrielles
dans l'École Doctorale Terre Univers Environnement

Internal waves and mean flow in the presence of topography

Les ondes internes et l'écoulement moyen en
présence de topographie

Thèse soutenue publiquement le **5 Février, 2018**,
devant le jury composé de :

Thierry DAUXOIS

Ecole Normale Supérieure, Lyon, Président

Triantaphyllos AKYLAS

Massachusetts Institute of Technology, Rapporteur

Victor SHRIRA

Keele University, Rapporteur

Caroline MULLER

Ecole Normale Supérieure, Paris, Examinatrice

Chantal STAQUET

Université Grenoble Alpes, Examinatrice

Joël SOMMERIA

Université Grenoble Alpes, Directeur de thèse





Internal waves and mean flow in the presence of topography

A DISSERTATION PRESENTED
BY
KESHAV J. RAJA
TO
THE ÉCOLE DOCTORALE TERRE, UNIVERS ET ENVIRONNEMENT

IN PARTIAL FULFILLMENT OF THE REQUIREMENTS
FOR THE DEGREE OF
DOCTOR OF PHILOSOPHY
IN THE SUBJECT OF
GEOPHYSICAL FLUID MECHANICS

UNIVERSITÉ GRENOBLE ALPES
GRENOBLE, FRANCE
FEBRUARY 2018

© 2018 - *KESHAV J. RAJA*

PRINTED IN FRANCE

Coverpage figure : Satellite image of the South China Sea with colors added to indicate the calculated vertical displacement of ocean layers near 200 meters deep, based on simulated model data and calculations run by Harper Simmons at the University of Alaska at Fairbanks and depicted by a graphics team at the University of Washington. Orange indicates upward movement, and blue indicates downward movement.

Internal waves and mean flow in the presence of topography

ABSTRACT

IN ENGLISH

INTERNAL WAVES play an important role in many processes in oceans. The interaction between internal waves and ocean topography has been an active field of research for long. Yet there are many questions remaining on the topic. In this thesis, two main processes are examined namely, the reflection of internal wave beams on a slope, and generation of lee waves over a three-dimensional obstacle, using laboratory experiments and numerical simulations.

The nonlinear reflection of an internal wave beam on a uniform slope is studied using two-dimensional inviscid theory and numerical simulations. The resonant triadic interactions among the incident, reflected and second harmonic wave beams are investigated developing on existing theory and verifying them with results for numerical simulations.

In the case of reflection of three-dimensional internal wave beams, a strong mean horizontal flow is found to be induced by the wave beam, which perturbs the wave field and weakens the second harmonics. The generation of this wave-induced mean flow is examined using results from experiments and three-dimensional numerical simulations. Furthermore, the effects of background rotation on the wave induced mean flow are also studied using numerical simulations.

The Antarctic Circumpolar Current is considered as one of the main sources of mixing in oceans. Laboratory modelling of the Antarctic Circumpolar Current was done in the Coriolis platform at LEGI to study the topography induced drag on the current. The experiment and its results are also presented.

IN FRENCH

LES ONDES INTERNES jouent un rôle important dans de nombreux processus dans les océans. L'interaction entre les vagues internes et la topographie océanique a longtemps été un champ de recherche actif. Pourtant, il reste beaucoup de questions sur le sujet. Dans cette thèse, deux processus principaux sont examinés, à savoir la réflexion de faisceaux d'ondes internes sur une pente, et la génération d'ondes sous le vent sur un obstacle tridimensionnel, en utilisant des expériences de laboratoire et des simulations numériques.

La réflexion non linéaire d'un faisceau d'onde interne sur une pente uniforme est étudiée à l'aide de la théorie des invisques bidimensionnels et de simulations numériques. Les interactions triadiques résonnantes entre les faisceaux d'ondes incidentes, réfléchies et de deuxième harmonique sont étudiées en développant la théorie existante et en les vérifiant avec des résultats pour des simulations numériques.

Dans le cas de la réflexion de faisceaux d'ondes internes tridimensionnels, un fort flux horizontal moyen est induit par le faisceau d'onde, qui perturbe le champ d'onde et affaiblit les secondes harmoniques. La génération de ce flux moyen induit par les vagues est examinée à l'aide des résultats d'expériences et de simulations numériques tridimensionnelles. De plus, les effets de la rotation de fond sur le débit moyen induit par les vagues sont également étudiés à l'aide de simulations numériques.

Le courant circumpolaire antarctique est considéré comme l'une des principales sources de mélange dans les océans. La modélisation en laboratoire du courant circumpolaire antarctique a été réalisée sur la plate-forme de Coriolis à LEGI pour étudier la traînée induite par la topographie sur le courant. L'expérience et ses résultats sont également présentés.


Thanks

Joel and Chantal deserve the foremost gratitude for helping me complete this thesis. Their encouragement, patience and immense knowledge were invaluable during these three years. I consider it my fortune to be able to work with them.

I learned a lot of things from Caroline Muller during my masters that helped me tremendously during this thesis preparation. From plotting a figure properly to making a nice presentation, I remember her lessons to this day. She mentored the researcher that I am.

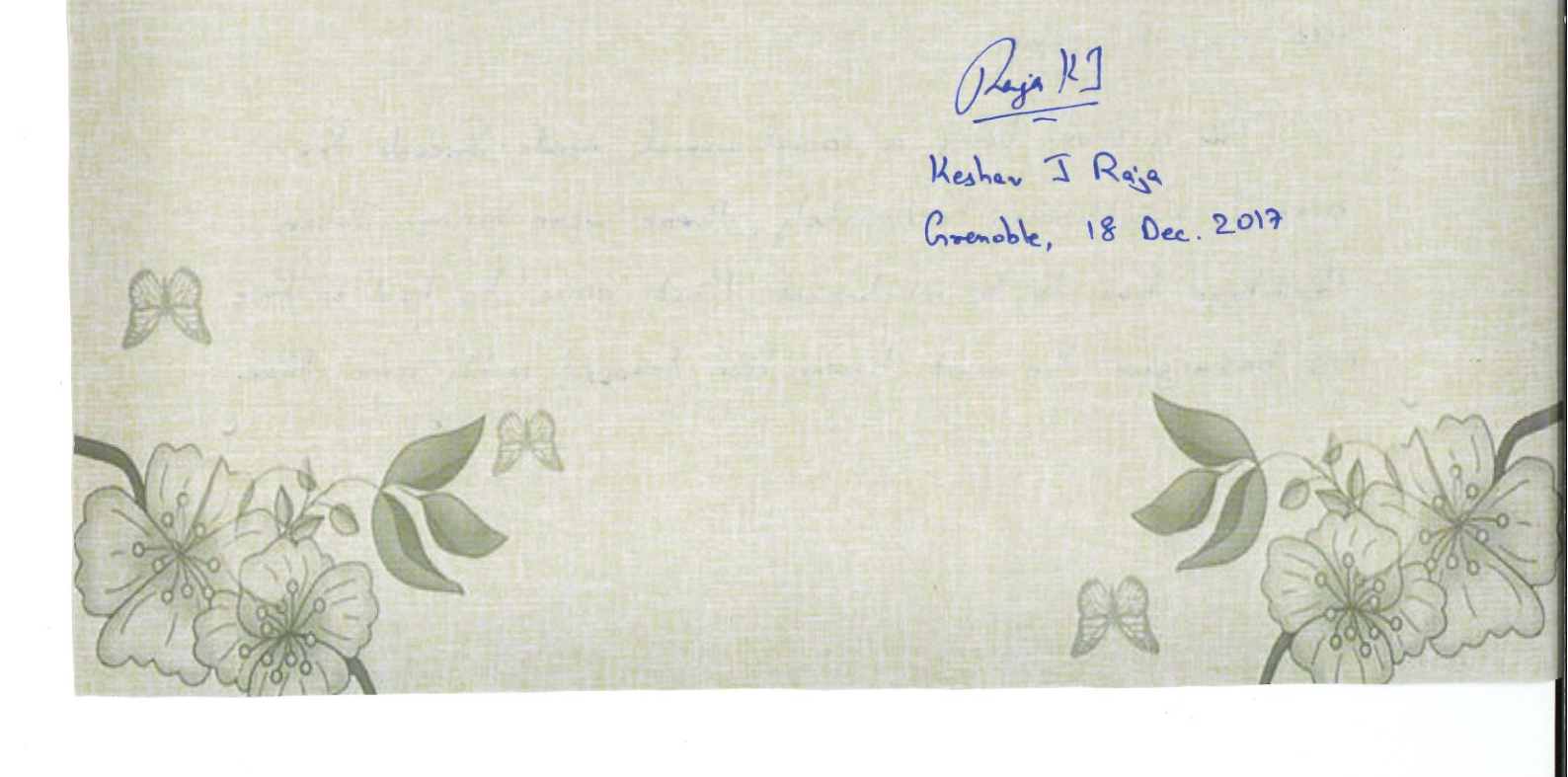
During the preparation of this thesis, there had been difficult, boring and ~~as~~ exciting times. If I could pass through them all, it was mainly because I knew I could pick up the phone and call my parents anytime. They were a constant moral support during these years. My brother, Madhav, deserves special mention for the hours-long conversations that helped me keep myself sane.

This author being a social animal, needs friends for normal functioning. Fortunately, there were many. Julian Quimbayo has to be mentioned first since he had to face my harangue the most having been trapped in the same office.



Julian knows most of my stupidities, complaints and dreams, and he has helped me to get myself together more than once when life was heavy. Many others in the lab have made my time here wonderful and enjoyable. I thank them all.

From outside the lab, I would like to thank Deepak for organising weekend "herbal" parties and Malavika for constantly cheering me to finish writing this thesis. You helped me regain focus and get back to work whenever I felt dispirited. I would also like thank Sean Symon and Felix Beckebanze for all the insightful discussions on science and politics. The love and support of Selma Moussaoui are irreplaceable and have helped me to boost my confidence and enthusiasm during the writing of this thesis, making this process much easier.



Raja KJ

Keshav J Raja

Grenoble, 18 Dec. 2017

Contents

1	INTRODUCTION	1
1.1	Internal gravity waves	2
1.2	Generation of internal waves in oceans	6
1.3	Role of internal waves in oceans	8
1.4	Internal waves in the laboratory	14
1.5	This thesis	16
2	PHYSICS OF INTERNAL WAVES	19
2.1	Stably stratified fluid	19
2.2	Linear internal waves	21
2.3	Linear reflection of plane internal waves	25
2.4	Internal wave beams	27
3	NONLINEAR REFLECTION OF TWO-DIMENSIONAL INTERNAL WAVE BEAMS	31
3.1	Introduction	32
3.2	Nonlinear reflection of a plane wave	34
3.3	Resonant interactions for nonlinear reflection of a wave beam	40
3.4	Eulerian mean flow and Stokes drift	44
3.5	Numerical simulations	44
3.6	Conclusions	51
4	REFLECTION OF THREE-DIMENSIONAL INTERNAL WAVE BEAMS	53
4.1	Forcing of mean flows by the reflection of three-dimensional internal wave beams (article)	54

5	THREE-DIMENSIONAL INERTIA-GRAVITY WAVE BEAMS	83
5.1	Numerical model and forcing	84
5.2	Induced mean flow and effect of Coriolis force	87
5.3	Energy budget	92
5.4	Conclusions	93
6	LABORATORY MODELLING OF ANTARCTIC CIRCUMPOLAR CURRENT	95
6.1	Dissipation of energy in the Southern Ocean	97
6.2	Stratified flow over three-dimensional topography	99
6.3	Experimental method	102
6.4	Results	106
6.5	Conclusions	116
7	DENOUEMENT	119
A1	NHM MODEL	123
	REFERENCES	135

Gaveshanam

noun

origin : *Sanskrit* (an ancient Indo-European language)

1. research
2. (literal) looking for cows

Nature uses only the longest threads to weave her patterns, so that each small piece of her fabric reveals the organisation of the entire tapestry.

Richard Feynman, The Character of Physical Law (1965)

1

Introduction

ONE OF THE KEY FEATURES that helped life to flourish on earth is its ability to continuously adapt and evolve to its environment. Life on earth survived aeons of hardships, environmental catastrophes and natural disasters by adapting and evolving to the environment. The evolution follows Darwinian natural selection, wherein a genetic trait that appears randomly in a species is naturally selected if it is beneficial for the survival of the species and is heritable. This form of generation, transmission and assimilation of information (genetic in this case) was critical for life to thrive in one form or the other on earth. We, human beings, though very much part of the said process and through the said process, have developed the concept of information beyond just genetic information. Our curiosity has led to the emergence of what is called a culture, which is the totality of all the generated information in the population, and perfected tools and methods for much faster transmission of these information so that it may be assimilated if found beneficial. One important aspect of the human culture is the emergence of what is called scientific method, a systematic way of organising knowledge through observations, experiments and forming testable explanations and predictions. Understanding the natural world helps us to adapt to the environment and survive, and in some cases, engineer the environment for our benefit. Moreover, it is important to be able to accurately predict the effects of human activities on the environment, so that we avoid taking actions that threaten our own survival in the environment. Thus, studying the natural world systematically and transmitting the knowledge, so that it can be assimilated in order to guide future actions, is an essential function for our survival.

We as living things are composed of and surrounded by fluids. Our planet is enveloped with an atmosphere and is mostly covered with vast oceans. A major part of the natural world around us involve fluid phenomena. Oceans and atmosphere are hosts to myriads of fluid

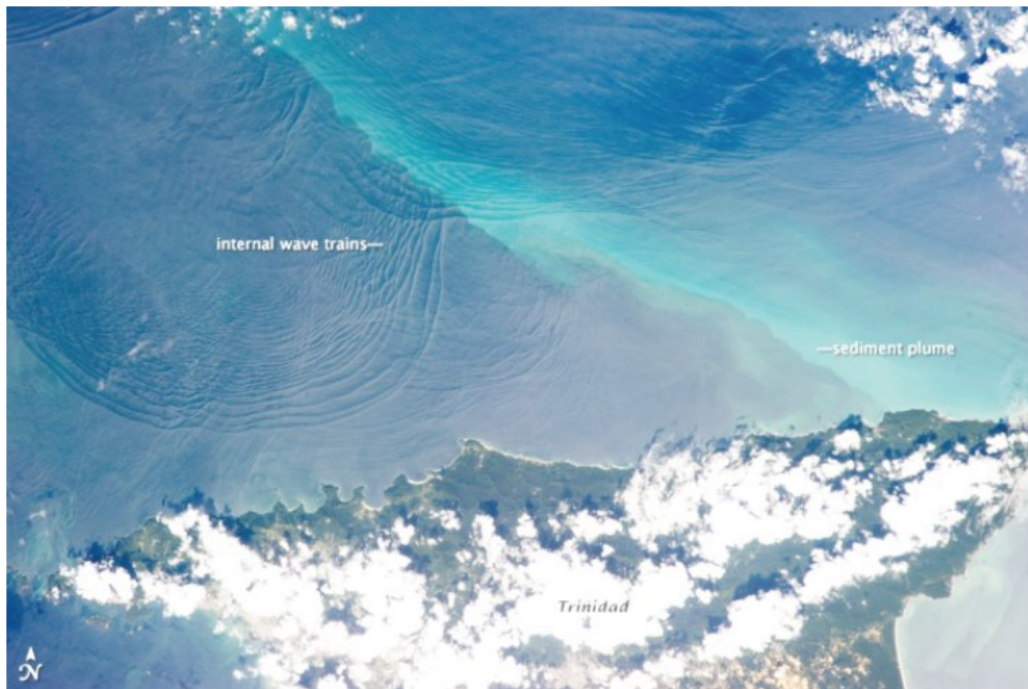
phenomena varying different space and time scales forced by primarily the energy from the sun. The interaction between the oceans and atmosphere and the land, and spontaneous instabilities that arise in the fluids lead to the appearance of different structures such as jets, vortices, waves and turbulence. These dynamical processes play an important role in shaping the larger climate system on the scale of the planet.

Recent observations have found that the global mean surface temperature has been rising since the beginning of the last century. The Intergovernmental Panel on Climate Change (IPCC) Fifth Assessment Report concluded that “*It is extremely likely that human influence has been the dominant cause of the observed warming since the mid-20th century.*” [Stocker et al. \(2013\)](#) In order to understand the response of climate to a forcing (climate sensitivity), it is crucial to precisely understand the various feedbacks that are present in the climate system. This requires a better knowledge of the physics of various fluid processes in the oceans and atmosphere. The global climate model cannot take into account many of the processes that are too small in scale or too short in time compared to the resolution of the model. However, the effect of all those processes has to be included in the model by parameterising those processes. The accuracy of the parameterisation depends on how well we understand the dynamics of the said process. Thus, these processes have to be studied in detail independently. One of such processes is internal gravity waves, the topic of this thesis.

1.1 INTERNAL GRAVITY WAVES

Waves are familiar to all of us. Yet, defining what is a wave is not as easy as perceiving one. [Scales and Snieder \(1999\)](#) explored this issue of the definition of a wave and concluded it to be an organised propagating imbalance. Nature loves stable equilibria. Whenever this stable equilibrium is perturbed it tries to restore using the forces that are present. The perturbation and the force trying to restore the equilibrium create an oscillation. This oscillation can propagate as long as it is in the field of the force, as a wave. While doing so, the wave transports energy with or without actual transport of matter. This creates many interesting physics related to waves.

Waves in the surface of the oceans are a pretty familiar sight. The interface between air and water in oceans is in stable equilibrium owing to the force of gravity. Any perturbation to this stable equilibrium can generate wave motions with gravity as the restoring force. The oceans and the atmosphere are also stratified within. The density varies with height in the oceans because of variations in salinity and temperature. The temperature (and density) varies with height in the atmosphere too. This stable density stratification of the oceans and atmosphere can be imagined as having an infinite number of interfaces within them. Although these interfaces are not as strong as the one between air and water on the surface of the ocean, they can support wave motions when perturbed. Owing to the uniform stratification of the medium, the waves can propagate not just on one of the interfaces but across the interfaces too. These waves, which exist inside the fluid medium, are called ‘internal gravity waves’.



*Ceux-ci ne sont pas des ondes internes.**

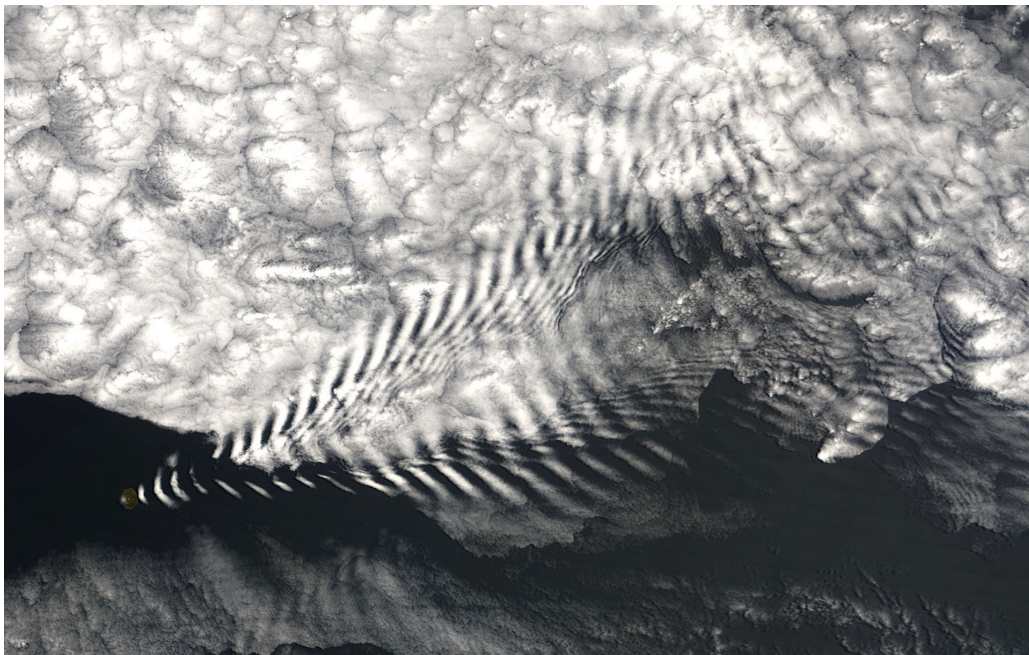


Figure 1.1.1: (Top) Image of internal waves off northern Trinidad, taken from International Space Station (ISS) on 18 January 2013; (Bottom) NASA satellite image (MODIS imager on board the Terra satellite) of a wave cloud forming off of Amsterdam Island in the far southern Indian Ocean taken on 19 December 2005.

* A small high-five to René Magritte

Depending on the scale of the motions, the earth's diurnal rotation can also affect the wave propagation. Since we are in a rotating frame of reference that is earth, motions in this frame will appear to be affected by the Coriolis force. Since it is always perpendicular to the velocity vector, the Coriolis force does not do any work. It cannot initiate any motion, but can deflect an already existing motion. The Coriolis force can also act as a restoring force on internal waves through this deflection. The internal waves with Coriolis force as the only restoring force are called 'inertial waves', and those waves for which both gravity and Coriolis force act as restoring forces are called 'inertia-gravity waves'. In this thesis, the term 'internal waves' is used to refer 'inertia-gravity waves' unless in the case of no rotation, where the term 'internal gravity waves' is used. Furthermore, in this thesis, we deal with only internal waves in oceans. Though the physics of internal waves in oceans and atmosphere is similar, the main focus in this thesis will be on internal wave dynamics in oceanic context.

Even though internal waves propagate inside the fluid, their presence can be revealed occasionally through a visible response. The velocity fluctuations associated with internal waves in oceans can extend to the surface, which then modify the roughness of surface waves. This can be detected by satellites, thereby observing indirectly, the presence of internal waves in the ocean. Clouds at times make it possible to visualise internal waves in the atmosphere. The adiabatic expansion cooling in the wave's crests will take the moisture in the atmosphere to its dew point, thereby forming clouds in the wave crests. In the troughs, adiabatic heating will lead to the evaporation of the clouds. Thus, clouds get arranged in bands, forming wave clouds. Figures 1.1.1 show the manifestation of internal waves in oceans and atmosphere. Internal waves may also dominate fluctuations in stratosphere, which can be studied using star scintillation. Signatures of internal waves can also be detected on other planets and even in stellar interiors.

The presence of internal waves has been reported long back. Sailors travelling close to the mouth of a river or a fjord, where fresh water flows into salty sea water without much mixing, sometimes find a puzzling resistance on their ship. Sailing ships at times stop completely and will not respond to the tiller. Motor boats would lose their speed suddenly and might stop dead in the water. Sailors called it 'dead water phenomenon'. Various methods were used by the mariners to beat the 'dead water'. In the olden days, it was believed that the dead water was caused by remoras or sucker-fish getting attached to the hull. Sailors would, therefore, fire guns into the water, beat and slash the water beside the boat with oars, drag a hawser beneath the vessel and so on. They also found that when they stopped their vessel for a few minutes and allowed the stern waves to pass, they seemed to have gotten rid of the dead water.

The dead water phenomenon was encountered by the Norwegian oceanographer, Fridtjof Nansen, during his *Fram* expedition in August 1893 in the Nordenskiöld Archipelago near the Taymyr Peninsula. Later, based on the observations by Nansen, his student V. W. Ekman studied this phenomenon during his PhD (Ekman, 1904) and explained the origin of dead water. When fresh water flows into the sea without mixing, it forms a layer atop the denser salty water. When the ship travels in this two layers of different density water, the disturbance creates underwater waves in the interface of the two layers. The energy of the boat is spent on

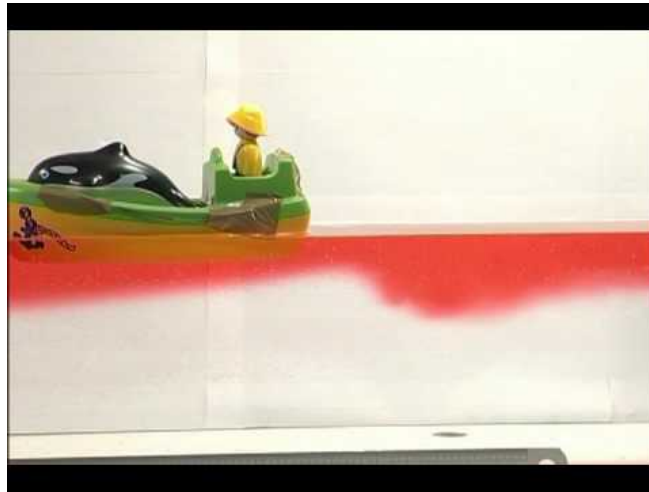


Figure 1.1.2: Image from the experiment performed by [Mercier et al. \(2011\)](#). Shown here is a toy boat dragged by a falling weight in a two layer fluid. The boat excited waves in the density interface of the two layers, spending energy in the process. This causes the drag experienced by the boat.

exciting the internal wave rather than propelling it forward, thus experiencing a wave-induced drag. Dead water phenomenon was revisited experimentally in the laboratory using modern techniques by [Mercier et al. \(2011\)](#), extending its description to more general situations such as a three-layer fluid or a linearly stratified fluid in the presence of a pycnocline.

During the *Fram* expedition, Nansen also noticed that temperature profiles below the surface in oceans sometimes change substantially within the course of just a few hours. [Helland-Hansen and Nansen \(1909\)](#) referred to the presence of some ‘puzzling waves’ from his observation. He reports, *“the most feasible explanation, according to our view, is therefore, that the changes of temperature, observed at the same depths, are due to oscillatory movements of the horizontal water-strata, at intermediate depths; and owing to their difference of density, these strata rest one on the top of another for a very long time, with more or less sharply defined boundaries horizontally.”* [p. 90] These internal waves are excited due to the stratification of the ocean below the surface. Typical time period and amplitude of these internal waves are larger than surface gravity waves in oceans because the density gradient inside the fluid is much smaller. Wavelength of an internal wave can vary from centimetres to kilometres and time periods vary from seconds to hours. Nevertheless, the internal waves provide the source for the ‘inner unrest’ in the oceans ([Gerkema and Zimmerman, 2008](#)). [Helland-Hansen and Nansen \(1909\)](#) concluded that the knowledge of the exact nature and causes of these waves are of signal importance to oceanography and is one of its greatest problems that urgently calls for a solution.

1.2 GENERATION OF INTERNAL WAVES IN OCEANS

The sources of internal waves can include interaction of a mean current or ocean tides with topography, wind stress fluctuation and many others. The cascades of nonlinear interaction often makes it impossible to trace the source of the waves (Staquet and Sommeria, 2002). Principal sources of internal waves in most of the oceans are wind and internal tides.

The winds force the top layer of the ocean. The top layer is typically not stratified and is called the mixed layer. However, the disturbances caused by the atmosphere in the mixed layer close to the surface of the ocean through wind can lead to variations in the bottom of the mixed layer. As these variations evolve towards equilibrium through geostrophic adjustment, internal waves are emitted. These internal waves have frequencies very close to the inertial frequency associated with Earth's diurnal rotation and therefore can be called as near-inertial waves. They are found to be the most energetic part of the internal-wave spectrum in the oceans. The energy input of the winds into near-inertial internal wave band can be studied using a slab model representation of the ocean's mixed layer. The estimates of winds' energy input can range from 0.3 TerraWatt to 1.3 TerraWatt. Alford (2003a) has estimated the energy input to be 0.5 TerraWatt from his slab model (figure 1.2.1b).

Another major source of internal waves in oceans is internal tides. These are formed by the motion of barotropic tides over the rough features at the bottom of the ocean, such as ridges, canyons and sea-mounts. The barotropic tides moving over the ocean topography give rise to a baroclinic response, allowing pressure anomalies to travel across the isopycnals. This baroclinic response leads to the generation of internal tides. Internal tides have the same frequency of that of the tides. The theory of internal tide generation in the oceans was given by Bell (1975a), Bell (1975b), Baines (1982) and was reviewed recently by Garrett and Kunze (2007).

Barotropic tides are generated by the gravitational pull of the moon and to some extent, the sun. These forces together with the rotation of Earth, create barotropic tides in the oceans. The generation of barotropic tides in the oceans on Earth affects as a drag on the angular velocity of the moon. This leads to the increase of the moon's orbit which can be measured from observations. This gives us a measure of how much energy is input into the barotropic tides in oceans (the oceanic tides extract major part of the energy compared to the tides in the mantle and the atmosphere; see figure 1.3.1). The energy that goes into the barotropic tides in the oceans is estimated to be about 3.5 TerraWatt. Most of this power is dissipated by bottom friction. About 1 TerraWatt of barotropic tidal power was found to be transferred to internal tides. The first large-scale estimates of global internal tide energy flux were provided by Egbert and Ray (2000), using sea surface altimetry data from satellites (figure 1.2.1a).

Apart from the tidal motions, a steady mean current over the ocean topography can also generate internal waves. These are usually high frequency internal waves propagating from the lee-side of the topography and therefore are called lee waves. The mean current could be strong tidal currents over topographic features with widths less than a tidal excursion (Garrett and Kunze, 2007), or it could be strong bottom flows such as in the Southern Ocean

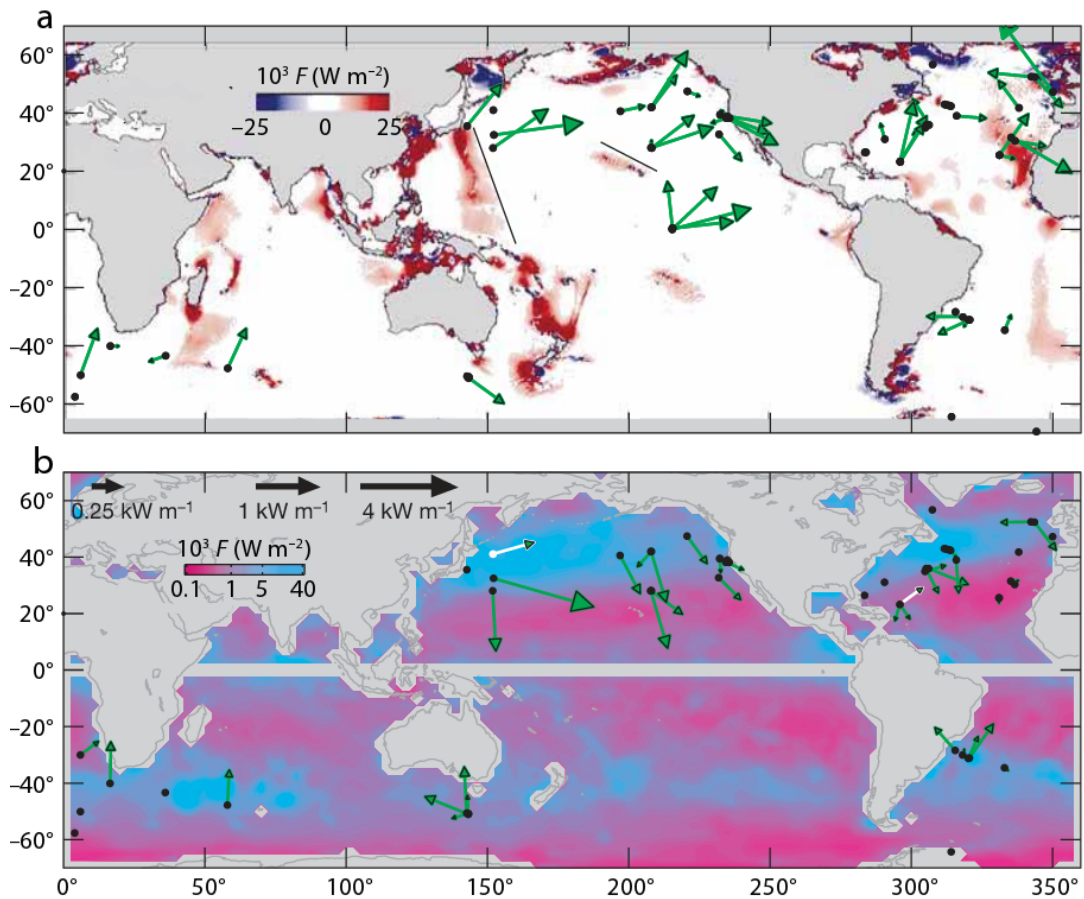


Figure 1.2.1: Maps showing energy input into internal waves by (a) semidiurnal tides, and (b) winds. (a) The semi-diurnal internal tide energy input was estimated using the TopeX poseidon Global inverse solution tidal assimilation model (Egbert and Ray, 2000). (b) Annual-mean wind energy input to near-inertial mixed-layer motions as estimated by the model of Alford (2003a). Both panels show vectors of energy flux as measured by mooring records at various sites in the global ocean. Alford (2003b) provides additional details of these maps. Figure adapted from Alford (2003b).

1.3 ROLE OF INTERNAL WAVES IN OCEANS

In the oceans, diapycnal mixing is essential to compensate the deep water formation in high latitudes in order to maintain the meridional overturning circulation (MOC). The strength of the MOC depends upon the intensity and distribution of the ocean mixing. In the absence of diapycnal mixing, in a few millenia, the ocean would turn into a stagnant reservoir of cold saline water with near-surface mixing and weak convectively driven circulation maintaining a local equilibrium (Munk and Wunsch, 1998). The stable stratification of the oceans makes this diapycnal mixing difficult.

It has been showed by Munk (1966) that in order to balance the effects of downward diffusion and upwelling in the global ocean, a basin averaged eddy diffusivity of about $10^{-4}m^2s^{-1}$ is needed. This particular value was reached by Munk (1966) by assuming the global balance of downward diffusion and upwelling to be applicable point-wise and using density and radio-carbon data from central Pacific ocean.

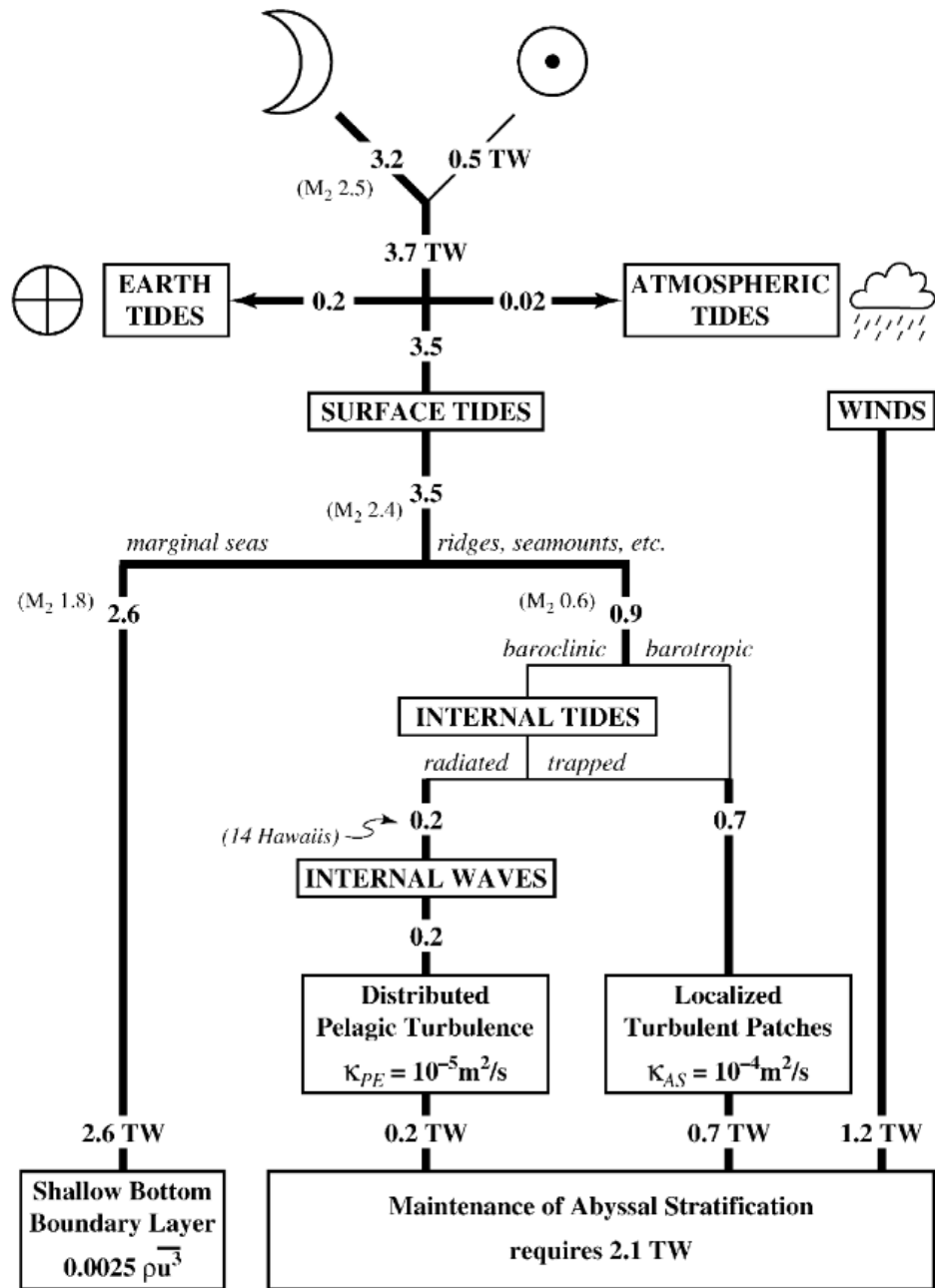
However, Ledwell et al. (1993) using direct dye release in the open ocean at a depth of about 310m noticed that the mixing coefficient in the interior of the ocean is almost an order of magnitude lesser than the prediction of Munk (1966). This is in agreement with micro-structure measurements done to measure diapycnal mixing in the ocean (Polzin et al., 1997, Gregg, 1998). Osborn (1980) had proposed the relation between diapycnal diffusivity κ and the mixing rate ϵ using flux Richardson number R_f and buoyancy frequency N as

$$\kappa = \frac{R_f}{1 - R_f} \frac{\epsilon}{N^2} < 0.2 \frac{\epsilon}{N^2} \quad (1.1)$$

Using this relation, from the micro-structure data from South Atlantic Ocean, Polzin et al. (1997) noted that the diapycnal diffusivity is about $10^{-5}m^2s^{-1}$ above smooth abyssal terrain, however, the diffusivity is very large throughout the water column (about $5 \times 10^{-4}m^2s^{-1}$ close to the bottom) above the Mid-Atlantic ridge.

(Munk and Wunsch, 1998) suggests that it is not fruitful to compare the basin averaged

Figure 1.3.1 (following page): From Munk and Wunsch (1998). An impressionistic budget of tidal energy flux. The traditional sink is in the bottom boundary layer (BBL) of marginal seas. Preliminary results from Egbert (1997) based on TOPEX/-POSEIDON altimetry suggest that 0.9 TW (including 0.6 TW of M2 energy) are scattered at open ocean ridges and sea-mounts. Light lines represent speculation with no observational support. "14 Hawaiis" refers to an attempted global extrapolation of surface to internal tide scattering measured at Hawaii, resulting in 0.2 TW available for internal wave generation. The wind energy input is estimated from Wunsch (1998), to which 0.2 TW was added to balance the energy budget. This extra energy is identified as wind-generated internal waves - radiating into the abyss and contributing to mixing processes.



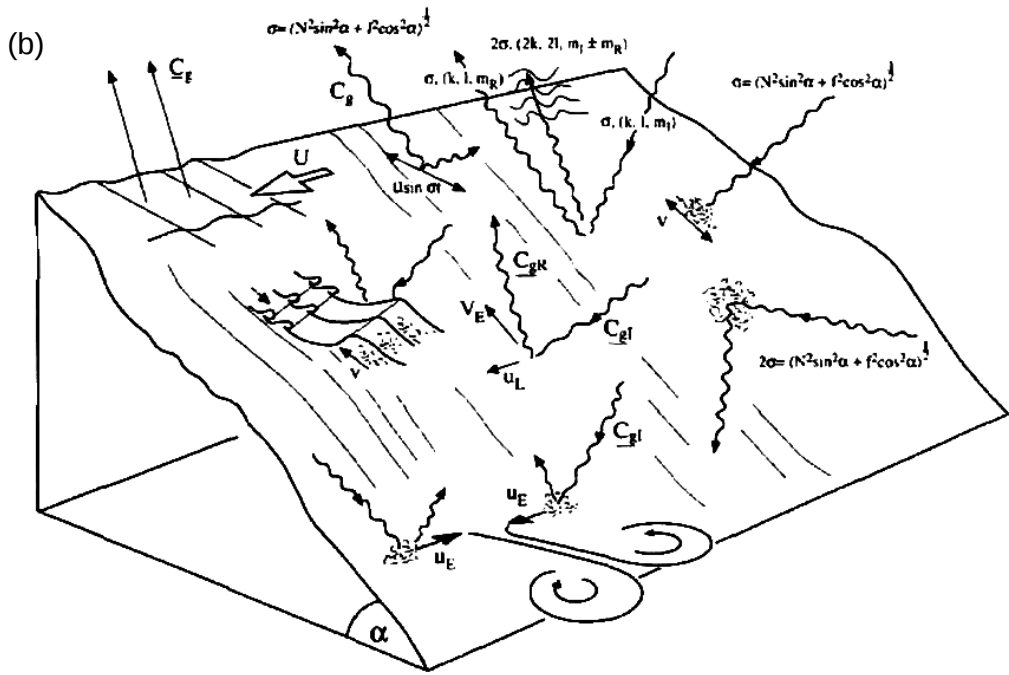
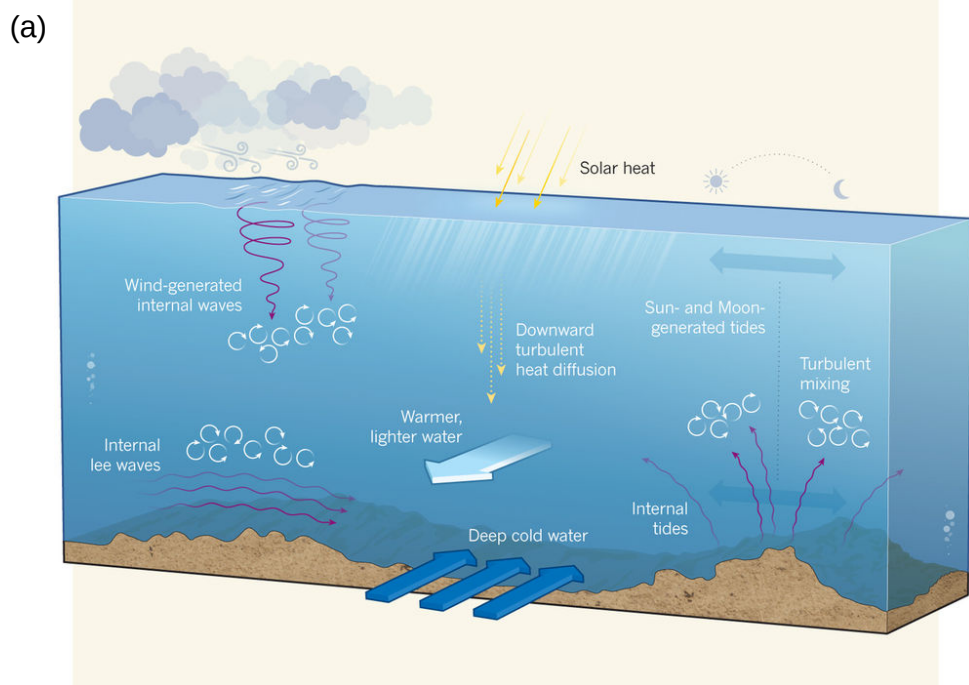
eddy diffusivity calculated by Munk (1966) with point-measurements at different places in the ocean. They argue that the ocean mixing is not uniform with very high mixing in concentrated source regions of buoyancy flux.

Mixing across density layers requires power. Various processes have been proposed to be the source of the power for diapycnal mixing. (Munk and Wunsch, 1998) argues that tides and wind are the dominant sources (figure 1.3.1). The power available from tides and wind matches with the power required to maintain the abyssal stratification in the oceans, as proposed in figure 1.3.1. In the open ocean, far from the topography, internal wave field is the major contributor of vertical mixing. Using fine and micro-structure data from a free falling profiler, Polzin et al. (1995) have found that the breaking of internal waves is the leading contributor to turbulent mixing in the interior of the ocean away from the surface or bottom boundary layers. They show that the internal wave activity correlates well with the intensity of turbulent fluctuations. This ‘pelagic’ (ocean interior) dissipation is the one measured to be giving a diffusivity of around $10^{-5} m^2 s^{-1}$. Internal waves can interact with the bottom topography and these interactions can cause localised turbulent patches, which account for the high value of diffusivity measured close to the topography.

Internal tides generated from deep ocean ridges or sea mounts can propagate large distances before breaking and transferring energy to small scales. Lefauve et al. (2015) have created a three dimensional map of tidal dissipation over abyssal hills based on linear wave theory with a nonlinear parameterisation for wave breaking and have found that the dissipation drops exponentially with height from the bottom but has a maximum at mid-depth due to the interplay of wave amplitude with stratification.

Observations have shown that the internal wave kinetic energy and turbulent energy dissipation are enhanced in the first kilometre above the ocean topography in the Southern Ocean where ACC is active ((Garabato et al., 2004b), (Sloyan, 2005)). From these observations, we can surmise that the internal lee waves generated by the flow of ACC over ocean topog-

Figure 1.3.2 (following page): (a) Turbulent mixing (curly arrows) is driven by breaking internal waves in the ocean interior. (b) Physical processes involving the interaction of internal waves on sloping topography. Moving from the top left to right these are (i) lee wave generation by flow over topography, (ii) wave generation by oscillatory flow, particularly those of tidal period, (iii) resonant interaction between incident and reflected waves and, (iv) wave breaking when the incident is near or at critical frequency. The second row, left to right, shows (v) wave steepening and the formation of fronts upon reflection, (vi) the generation of upslope Eulerian mean flows, V_E , and along-slope Lagrangian mean flows, U_L , as waves reflect, and (vii) mixing produced by reflecting sub-critical waves when the first harmonic is near critical. The final illustration, bottom left, represents Eulerian mean flows, U_E , generated by waves, which break and lose momentum at the boundary (courtesy of S. Thorpe; taken from Muller and Briscoe (2000)).



raphy break in the ocean bottom layer causing the enhanced turbulence in those regions. [Nikurashin and Ferrari \(2010\)](#) uses a weakly nonlinear theory to study the generation of internal lee waves by geostrophic motions interacting with small scale topography. They found that strong inertial oscillations are driven by the internal waves generated at steep topography, and this along with geostrophic flow result in enhanced wave breaking and mixing. The impact of realistic, multi-scale abyssal hill topography on internal wave generation in the Drake passage of the Southern Ocean was discussed using 2D and 3D simulations by [Nikurashin et al. \(2014\)](#).

Internal waves play a crucial role in promoting mixing in the ocean. Identifying and quantifying the various mechanisms that act as a sink of energy in the internal waves spectrum is still to be done exhaustively. [Thorpe \(1975\)](#) presents an early review of various physical processes affecting the interaction and dissipation of internal waves in deep ocean. Among many of the processes that involve internal waves, a major share of them are close to the ocean bottom topography. Internal waves generated by wind close to the surface of the ocean may interact with themselves and contribute towards mixing. However, the major contributions come from regions close to the topography (figure 1.3.2(a)).

The nonlinear interactions of internal waves form a major part of the dynamics of internal waves. Nonlinear interactions facilitate the energy cascade from large scales to smaller scales and promote mixing. [Muller et al. \(1986\)](#) review the nonlinear interactions of internal waves. They describe resonant interactions of internal waves and mention a few strong interactions as well. Resonant interactions are one of the ways in which internal waves steepen and ultimately break to induce mixing. In the inviscid, diffusionless case, a pure plane wave in uniform stratification feeds secondary waves through resonant interactions, and is therefore always unstable. Many of these processes have a chance of occurring when internal waves interact with the bottom topography (figure 1.3.2(b)).

[Staquet and Sommeria \(2002\)](#) have described different mechanisms by which internal waves steepen and break to form wave turbulence of which one of the main mechanisms is internal wave reflection. Internal waves get focused upon reflection on a slope of suitable angle. Due to the simple, but unusual, reflection laws for internal waves, there exists a critical angle for which the reflected wave will have infinite amplitude, zero group velocity and infinitesimal wavelength according to the linear theory. Thus, the linear theory breaks down near critical angle ([Dauxois and Young, 1999](#)). Numerous studies have been done on the breaking of internal waves during reflection on a slope close to the critical angle, and has been observed in the oceans as well ([Eriksen, 1998](#)).

Reflection of internal waves from boundaries creates higher harmonics ([Rodenborn et al., 2011](#)) which can interact resonantly with the primary waves leading to energy cascade from the primary waves. [Teoh et al. \(1997\)](#) and [Javam et al. \(2000\)](#) have observed non-resonant wave-wave interactions in colliding waves which create evanescent modes that lead to trapping of wave energy in the interaction region and ultimate overturning of the density fields in the interaction region. This can occur close to the topography where several rays of internal waves are generated as reflected waves or higher harmonics.

Waves are known to irreversibly induce a mean flow when propagating in a dissipative medium (Lighthill, 1978). This is much more familiar in the context of surface water waves. The mean Lagrangian velocity (velocity following the fluid parcels) due to the wave is the sum of the Eulerian mean velocity (mean velocity of the fluid at a given point) and a Stokes drift. Longuet-Higgins (1953) derived an expression for Stokes drift for viscous water waves. These calculations have been further extended and used in some particular cases such as waves propagating along a sloping sea bed in Longuet-Higgins (1969). When a surface wave approaches a beach at an oblique angle, a mean current parallel to the coastline is generated by the wave through radiation stress facilitating sediment transport (Longuet-Higgins, 1970). Surface wave driven currents in barred beaches were studied analytically and numerically by Bühler and Jacobson (2001).

Internal waves in oceans also play an important role with their ability to transport energy and momentum over large distances. Bretherton (1969b) showed that internal waves can induce mean motions of second order in the wave amplitude. He also derived an expression for the mean flow caused by an internal wave packet propagating into a quiescent fluid. In the oceans, the mean motions induced by internal waves have many consequences. New (1988) have found enhanced phytoplankton activity near the continental shelf-break in the Bay of Biscay because of the internal tide assisted vertical transport of nutrient rich abyssal water to the sunlit upper layers of the ocean. Cacchione et al. (2002) have proposed that internal tides reflecting and the associated sediment transport can shape continental slopes in ocean basins.

Internal waves interacting with a vertically varying mean flow can lead to acceleration of the mean flow at a level. This is famous in the atmospheric context where a vertically varying horizontal wind traps vertically propagating internal waves at the altitude where the phase speed of the wave is equal to the wind velocity. The trapped waves break at that altitude and thereby in effect act as a transporting mechanism for energy and momentum in vertical direction. This process can be imagined to happen in oceans too where there is strong mean flows, for instance in the Southern Ocean. This vertical transport of momentum and energy by internal waves has profound dynamical significance in oceans (Bretherton, 1969a). Furthermore, close to the bottom topography, internal waves may get refracted by a background mean flow and may reach critical condition before reflecting from a slope. Internal waves reflecting from a slope are also known to induce a mean flow in the region where the incident and reflected waves interact. Sutherland (2001) proposed that the reflecting internal wave can resonantly interact with this induced mean flow and become unstable. Thus, in various ways, mean flow and internal waves interaction can lead to instability and breaking of the waves.

Internal waves, thus, play an important role in many processes in oceans. The dynamics of internal waves is an active field of research today. Further insights into the ways in which internal waves contribute towards ocean dynamics can be obtained by detailed study of internal waves in idealised setting through laboratory experiments and numerical simulations wherein we can isolate and understand each of the many aspects of it.

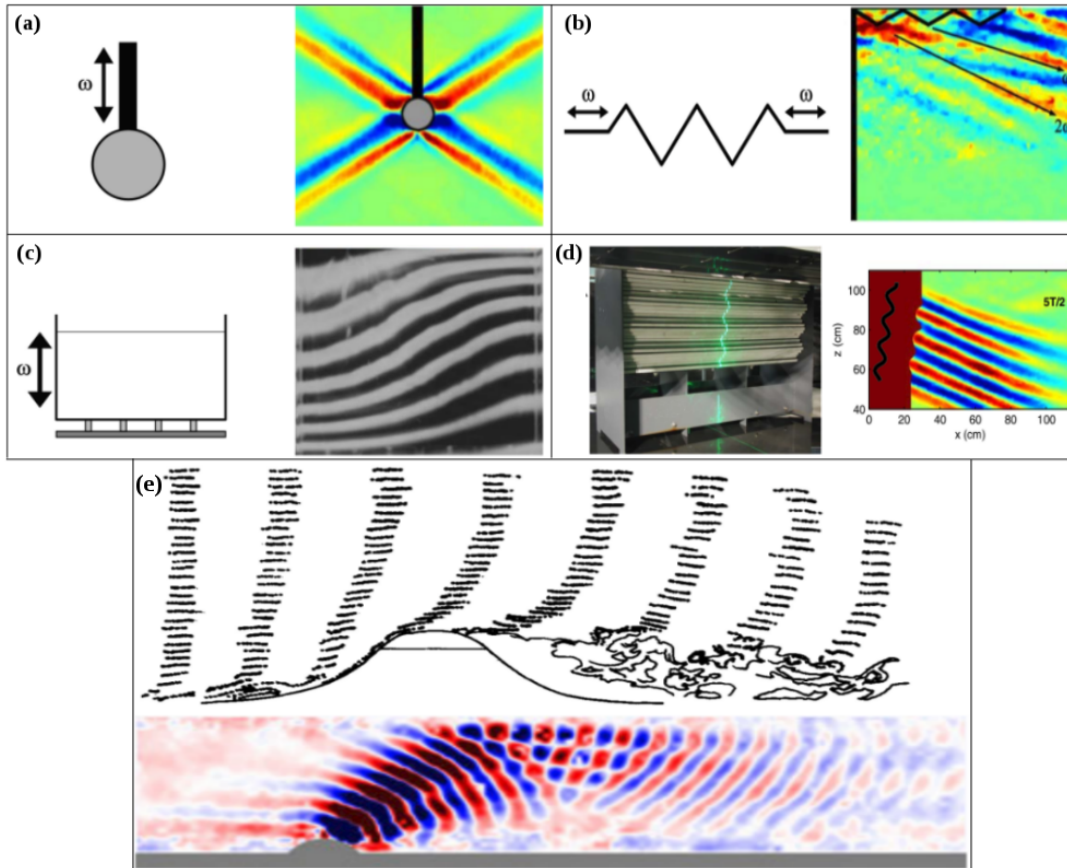


Figure 1.4.1: Various ways of generating internal waves in laboratories. The generating mechanism and the resulting wave field are shown for (a) a vertically oscillating cylinder, (b) paddle-like generator, (c) parametric excitation principle, (d) wave beam generator and (e) mean flow over topography. Images from [Gostiaux et al. \(2007\)](#), [Hunt and Snyder \(1980\)](#) and [Dalziel et al. \(2011\)](#).

1.4 INTERNAL WAVES IN THE LABORATORY

Internal waves have been investigated in laboratories starting from the second half of the last century. One of the first instances of visualising internal waves in a laboratory was done by [Görtler \(1943\)](#) in Göttingen, using a two dimensional setup of vertically oscillating cylinder as shown in figure 1.4.1 (a). Perhaps because of the complications of the war, this experiment was largely forgotten. The next similar experiment was performed by [Mowbray and Rarity \(1967b\)](#), which paved way for further experiments on internal waves.

The development of the Particle Image Velocimetry (PIV) technique by the end of the last century spurred numerous experimental studies on internal waves. Similarly the advent of synthetic Schlieren method also lead to quantitative analysis of internal waves in labora-

tories. PIV technique gives access to time resolved velocity fields, while synthetic Schlieren method provides time resolved density fields (in narrow vertical tanks). These methods may be used to study internal waves generated by different methods. [Gostiaux et al. \(2007\)](#) has given a short review of different methods of exciting internal waves in the laboratory, while presenting their own wave generator.

The simplest internal wave generation method is using oscillating bodies in a stratified medium. The internal wave forcing using an oscillating cylinder is already mentioned above. An oscillating cylinder produces four beams of internal waves (figure 1.4.1(a) right side) making a constant angle with the vertical (dictated by the dispersion relation). Three dimensional experiments of a moving sphere in a stratified medium were carried out by [Mowbray and Rarity \(1967a\)](#) with the aim of verifying the linear theory of internal waves. Later, [Peacock and Weidman \(2005\)](#) performed three dimensional experiments using an oscillating sphere in a stratified and rotating medium and they observed a double cone wave pattern. They claim to be the first ones to compare the theoretically predicted dispersion relation of inertia-gravity waves with real experimental data.

Another way of exciting internal waves is by using a multi-bladed folding paddle as shown in figure 1.4.1 (b) being moved horizontally with a frequency ([Cacchione and Wunsch, 1974](#), [Teoh et al., 1997](#), [Gostiaux, 2006](#)). Such a forcing generates two wave beams that propagate in opposite directions. In figure 1.4.1 (b) right side, we can see that a vertical wall in the west side of the domain prevents the propagation of one of the beams (left propagating beam), which reflect on the wall and continue propagating rightwards.

Internal waves can also be generated by a vertical periodic motion of the fluid tank itself as in the experiments of [Benielli and Sommeria \(1998\)](#). Figure 1.4.1 (c) shows the experimental setup and the generated waves. This kind of motion acts as a perturbation of the gravitational force on the system. Among the many modes that are possible, the resonant modes in accordance with the geometry of the fluid domain will grow.

All the above methods have limitations in controlling different parameters of the internal wave. In order to generate a monochromatic plane internal wave beam, [Gostiaux et al. \(2007\)](#) proposed a new solution for generating internal waves, a wave generator. Their wave generator consists of horizontal plates attached to camshafts placed in a sinusoidally shifted position when at rest. These plates oscillate back and forth when the camshafts rotate. The motion of the plates create an upward propagating sinusoid on the surface of the wave generator. The wave generator is shown in the figure 1.4.1 (d), left side. This wave generator can excite internal wave beams of finite width in the horizontal and vertical directions. Figure 1.4.1 (d) right side shows the propagating monochromatic internal wave beam.

Internal waves have been investigated in laboratories using topographies to generate them. In the previous section, we mentioned that a major source of internal waves in the environment is through large scale fluid motion over ocean topography or mountains. The tidal motion over ocean topography generates internal tides, and a mean flow over the topography generates internal lee waves. [Hunt and Snyder \(1980\)](#) have studied the generation of lee waves and eddies when stratified fluid flows over a three dimensional mountain as sketched

in figure 1.4.1 (e) top panel. Similar experiments were also done by Dalziel et al. (2011) where they studied lee waves generated by a hemisphere as shown in the bottom panel of figure 1.4.1 (e).

Recent improvements in the visualisation techniques and advancements in image processing have stimulated more and more research on internal waves in the laboratories. Developments such as the wave generators have opened new vistas for internal wave research. Laboratory experiments compliment as well as motivate theoretical developments, and our understanding of the dynamics of internal waves is increasing day after day. This thesis is the latest example of laboratory experiments triggering an investigation, adding on to what we know of internal waves.

1.5 THIS THESIS

There are two aspects of internal waves and mean flows that are dealt with in this thesis. One is the reflection of an internal wave beam on a simple slope and forcing of mean flows in the process. The other is the interaction of a mean flow with a bottom topography to generate internal lee waves.

The present chapter introduced internal waves in general, its role in ocean dynamics and the ways in which it is studied in laboratories. In chapter 2, the physics of linear internal waves are presented, in order to establish the notations and definitions we use in this thesis. A short introduction to internal wave beams is also presented in chapter 2 in order to setup the discussions in the following chapters.

The nonlinear reflection of two-dimensional internal wave beams is discussed in chapter 3. The resonant interactions among the incident, reflected and second harmonic waves during the reflection of internal waves on a simple slope was examined by Thorpe (1987). In chapter 3, we present an extension of this theory to internal wave beams in the presence of background rotation. The theoretical work was done by Dr. Matthieu Leclair (ETH Zurich) during his post-doctoral work in LEGI. The theory was tested using two-dimensional numerical simulations by this author. The results presented in chapter 3 are planned to be submitted as an article in *Journal of Fluid Mechanics*.

The three-dimensional internal wave beams reflecting on a slope was studied using laboratory experiments in LEGI in 2009-2012. The results from the experiments were published in Grisouard (2010) and Grisouard et al. (2013). However, the mechanism of generation of strong horizontally recirculating mean flow was not clear. Three-dimensional numerical simulations were done by this author to understand the wave-induced mean flow for different wave parameters. The results from the laboratory experiment and numerical simulations are presented in chapter 4 in the form of the draft of an article that is planned to be submitted in *Journal of Fluid Mechanics*.

The effects of background rotation on the reflection of three-dimensional internal wave beams are presented in chapter 5. This problem has not been addressed so far to the best of our knowledge. We find that the Coriolis force discourages the streaming of Eulerian mean

flow by the wave beams.

The last chapter (chapter 6) presents the laboratory modelling of Antarctic Circumpolar Current (ACC) performed in the Coriolis platform of LEGI in March-April 2016. The internal lee waves and the wake of eddies formed by a spherical in a mean geostrophic flow was studied with and without background rotation. Furthermore, the effect of bottom drag by a random topography in the Southern ocean was examined using several spherical caps in the mean flow, with and without background rotation.

Physics is like sex: sure, it may give some practical results, but that's not why we do it.

Richard Feynman, *Scary Monsters and Bright Ideas*
(2000)

2

Physics of Internal Waves

THE PRINCIPLE OF ARCHIMEDES states that a body immersed in a fluid experiences an upward force equal to the weight of the fluid displaced by it. This upward force, called the force of buoyancy (indicated as b) is due to the difference in pressure between the top and bottom of the submerged body. The pressure is different at different depths because the weight of the fluid above a certain depth is balanced by the pressure at that depth, in order to maintain the hydrostatic equilibrium.

If we consider a system with fluids of different densities, the buoyancy force tends to raise the lighter fluids above the heavier fluids, so that in equilibrium in such a system, a stable stratification of density develops. When a perturbation is applied on this system the buoyancy acts as a restoring force to bring back the system into its initial status. The action of restoring force creates oscillations which may propagate in the fluid. Internal gravity waves are propagating disturbances in stratified fluids. We, thus, begin our discussion of physics of internal waves through a brief introduction to stably stratified fluids.

The fundamental results for linear internal waves are presented in this chapter to establish the notations and conventions we will use in this thesis. A more exhaustive treatment of the subject has been done in several textbooks such as [Gerkema and Zimmerman \(2008\)](#), [Sutherland \(2010\)](#) or [Vallis \(2017\)](#).

2.1 STABLY STRATIFIED FLUID

A fluid medium is said to be stratified if there is a mean vertical gradient of (potential) density that is large compared with its horizontal gradient. Let us consider a parcel of fluid that is

displaced adiabatically from z to $z + \delta z$. The parcel preserves its potential density ρ_θ when it is moved adiabatically. Without loss of generality, let the pressure at $z + \delta z$ be the reference pressure. Then we have,

$$\rho(z + \delta z) = \rho_\theta(z + \delta z) \quad (2.1)$$

The density ρ can be written as,

$$\rho = \rho_0 + \widehat{\rho}(z) + \rho'(x, y, z, t) \quad (2.2)$$

where ρ' is the density perturbation over the vertical density profile $\widehat{\rho}$ and ρ_0 is a constant reference density. When the parcel at z with the density $\rho_0 + \widehat{\rho}(z)$ is moved to $z + \delta z$, it finds that the ambient density is $\rho_0 + \widehat{\rho}(z + \delta z)$. The difference in the densities of the parcel and the ambient $\delta\rho$ can be written as,

$$\delta\rho = \rho_{\text{parcel}}|_{z+\delta z} - \rho_{\text{ambient}}|_{z+\delta z} \quad (2.3)$$

$$= \rho(z + \delta z) - \widehat{\rho}(z + \delta z) \quad (2.4)$$

$$= \rho_\theta(z + \delta z) - \widehat{\rho}_\theta(z + \delta z) \quad (2.5)$$

$$= \rho_\theta(z) - \widehat{\rho}_\theta(z + \delta z) \quad (2.6)$$

$$= \widehat{\rho}(z) - \widehat{\rho}_\theta(z + \delta z) \quad (2.7)$$

$$= -\frac{\partial \widehat{\rho}_\theta}{\partial z} \delta z \quad (2.8)$$

The net force on the displaced fluid parcel is the buoyancy force on that fluid minus its weight, which is given by,

$$F = -\delta\rho g = g \frac{\partial \widehat{\rho}_\theta}{\partial z} \delta z \quad (2.9)$$

$$\frac{\partial^2 \delta z}{\partial t^2} = \left(\frac{g}{\rho} \frac{\partial \widehat{\rho}_\theta}{\partial z} \right) \delta z \quad (2.10)$$

If the displacement and the acceleration have the same direction then the system is unstable. This will give us the condition for stability as follows.

$$\frac{\partial \widehat{\rho}_\theta}{\partial z} = \begin{cases} < 0, & \text{Stably stratified} \\ > 0, & \text{Unstably stratified} \end{cases} \quad (2.11)$$

2.1.1 BRUNT-VÄISÄLÄ FREQUENCY

From equation 2.10, we can notice that for a stably stratified fluid, a perturbation on its equilibrium will setup oscillations with a frequency N given by,

$$N^2 = -\left(\frac{g}{\rho} \frac{\partial \widehat{\rho}_\theta}{\partial z} \right) \quad (2.12)$$

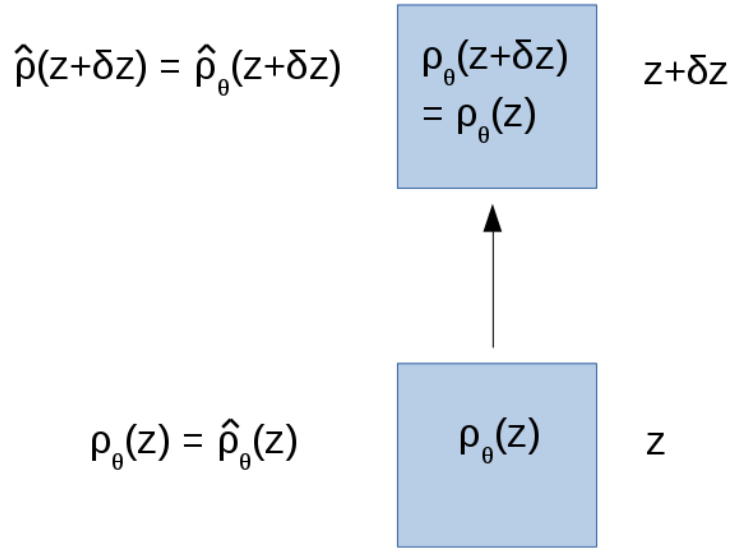


Figure 2.1.1: A parcel is adiabatically displaced upward from level z to $z + \delta z$, preserving its potential density, which it takes from the environment at level z . If $z + \delta z$ is the reference level, the potential density there is equal to the actual density. The parcel's stability is determined by the difference between its density and the environmental density; if the difference is positive the displacement is stable, and conversely.

This is the natural frequency of the stratified system and is called Brunt-Väisälä or buoyancy frequency.

2.2 LINEAR INTERNAL WAVES

The vertical variation of density in many naturally occurring continuously stratified media is rather small compared to the reference density ρ_0 . We may exploit this smallness of density variation and use an approximation in the governing equations. In the equation 2.2, we can fairly assume that $\rho_0 \gg |\hat{\rho}(z)|, |\rho'(x, y, z, t)|$. This is called the *Boussinesq approximation*. The consequence of this assumption is that the vertical variation of density in the momentum equation is taken into account only in the buoyancy term.

Similarly, we may also attempt another approximation. The angular velocity of the Earth, Ω , has two components, Ω_y and Ω_z at any point on Earth. However, if our system does not involve flows over large length scales (compared to the radius of Earth), we can assume that Ω_y is negligible compared to Ω_z . Then, the Coriolis parameter $f = 2\Omega_z$ can be considered to be a constant in our equations. This is called the *f-plane approximation*.

Using these approximations we can simplify the governing equations. For the velocity vector \mathbf{u} , pressure p and density ρ with a reference density ρ_0 , the governing equations after

using the above approximations are as follows.

$$\frac{\partial \mathbf{u}}{\partial t} + \mathbf{u} \cdot \nabla \mathbf{u} = -\nabla p - f \hat{\mathbf{e}}_z \times \mathbf{u} - \frac{\rho g}{\rho_0} \hat{\mathbf{e}}_z + \nu \nabla^2 \mathbf{u} \quad (2.13a)$$

$$\frac{\partial \rho}{\partial t} + \nabla \cdot (\mathbf{u} \rho) = \kappa \nabla^2 \rho \quad (2.13b)$$

$$\nabla \cdot \mathbf{u} = 0 \quad (2.13c)$$

We can use the decomposition of ρ given in equation 2.2. The pressure p can also be decomposed as,

$$p = \hat{p}(z) + p'(x, y, z, t) \quad (2.14)$$

where p' is the pressure perturbation over the background pressure field \hat{p} . We also have the hydrostatic balance given by,

$$\frac{d\hat{p}(z)}{dz} = -g \left(\frac{\rho_0 + \hat{\rho}}{\rho_0} \right) \quad (2.15)$$

Using the definition of Brunt-Väisälä frequency, we can write,

$$\frac{d\hat{p}(z)}{dz} = -\frac{\rho_0}{g} N^2 \quad (2.16)$$

Using these definitions and neglecting the nonlinear term we get the following linearised system of equations.

$$\frac{\partial u}{\partial t} + \frac{\partial p'}{\partial x} - f v - \nu \nabla^2 u = 0 \quad (2.17a)$$

$$\frac{\partial v}{\partial t} + \frac{\partial p'}{\partial y} + f u - \nu \nabla^2 v = 0 \quad (2.17b)$$

$$\frac{\partial w}{\partial t} + \frac{\partial p'}{\partial z} - b - \nu \nabla^2 w = 0 \quad (2.17c)$$

$$\frac{\partial b}{\partial t} + N^2 w - \kappa \nabla^2 b = 0 \quad (2.17d)$$

$$\frac{\partial u}{\partial x} + \frac{\partial v}{\partial y} + \frac{\partial w}{\partial z} = 0 \quad (2.17e)$$

where b is the buoyancy defined as,

$$b = -\frac{\rho'g}{\rho_0} \quad (2.18)$$

If we write,

$$\phi = [u \quad v \quad w \quad p \quad b]^T \quad (2.19)$$

then the equations 2.17 can be written as,

$$\begin{bmatrix} (\frac{\partial}{\partial t} - \nu \nabla^2) & -f & 0 & \frac{\partial}{\partial x} & 0 \\ f & (\frac{\partial}{\partial t} - \nu \nabla^2) & 0 & \frac{\partial}{\partial y} & 0 \\ 0 & 0 & (\frac{\partial}{\partial t} - \nu \nabla^2) & \frac{\partial}{\partial z} & -1 \\ 0 & 0 & N^2 & 0 & (\frac{\partial}{\partial t} - \kappa \nabla^2) \\ \frac{\partial}{\partial x} & \frac{\partial}{\partial y} & \frac{\partial}{\partial z} & 0 & 0 \end{bmatrix} \phi = 0 \quad (2.20)$$

The system has non-trivial solutions only if the coefficient matrix is singular. The determinant of the coefficient matrix equals to zero leads to the following equation,

$$\left\{ \frac{\partial}{\partial t} \left(\frac{\partial^2}{\partial t^2} \nabla^2 + N^2 \nabla_h^2 + f^2 \frac{\partial^2}{\partial z^2} \right) - \nu \nabla^2 \left(2 \frac{\partial^2}{\partial t^2} \nabla^2 - \nu \frac{\partial}{\partial t} \nabla^4 + N^2 \nabla_h^2 \right) \right\} \phi = 0 \quad (2.21)$$

We shall consider the inviscid case here to further simplify the equation. Thus neglecting the viscosity, we obtain,

$$\left(\frac{\partial^2}{\partial t^2} \nabla^2 + N^2 \nabla_h^2 + f^2 \frac{\partial^2}{\partial z^2} \right) \phi = 0 \quad (2.22)$$

This is a wave equation. We can use the following ansatz to seek a wave solution.

$$\phi = \Phi e^{i(\mathbf{K} \cdot \mathbf{x} - \omega t)} = \Phi e^{i(kx + ly + mz - \omega t)} \quad (2.23)$$

Using the ansatz in the wave equation, we get the following dispersion relation.

$$\omega^2 = N^2 \frac{k^2 + l^2}{k^2 + l^2 + m^2} + f^2 \frac{m^2}{k^2 + l^2 + m^2} \quad (2.24)$$

We can re-write the dispersion relation as,

$$\omega^2 = N^2 \sin^2 \theta + f^2 \cos^2 \theta \quad (2.25)$$

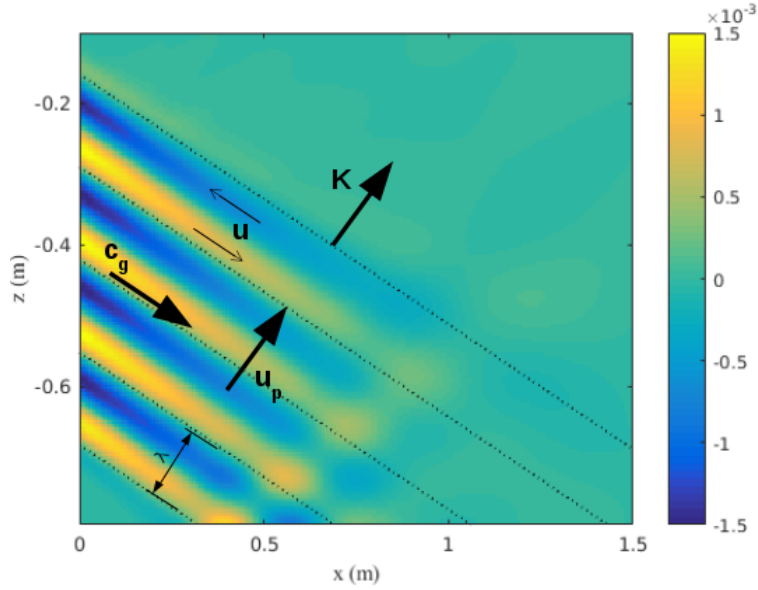


Figure 2.2.1: A snapshot from the simulation of an internal wave beam with a thickness of 4 wavelengths. The colour indicates the u -velocity ($m s^{-1}$) and dotted lines mark each wavelength. The wave propagates in the direction of its group velocity C_g but the phase propagates perpendicular to that in the direction of phase velocity u_p . The wave vector \mathbf{K} is in the same direction as the phase velocity. The fluid velocity is shown as u . The fluid particles oscillate forward or backward along the group velocity according to the phase.

where θ is then the angle between the wave vector and the direction of gravity.

The velocity of propagation of the phase of the wave (phase velocity u_p) can be written as,

$$\mathbf{u}_p = \frac{\omega}{|\mathbf{K}|^2} \mathbf{K} \quad (2.26)$$

The wave energy does not propagate at the same velocity as the phase. The velocity of propagation of wave energy (group velocity C_g) can be written as,

$$\mathbf{C}_g = \frac{\partial \omega}{\partial \mathbf{K}} = \frac{N^2 - f^2}{|\mathbf{K}|^2 \omega} (km^2, lm^2, -m(k^2 + l^2)) \quad (2.27)$$

We can rotate our coordinate system such that the wave vector is in the $x - z$ plane. This rotation will remove the wavenumber l and variations in y direction ($\partial/\partial y = 0$). With this simplification, we have the wave vector as follows.

$$\mathbf{K} = (k, m) = |\mathbf{K}|(\sin \theta, \cos \theta) \quad (2.28)$$

The phase velocity (the velocity in which the constant phase lines move) of internal waves can be calculated as the following.

$$\mathbf{u}_p = \frac{(N^2 \sin^2 \theta + f^2 \cos^2 \theta)^{1/2}}{|\mathbf{K}|} (\sin \theta, \cos \theta) \quad (2.29)$$

The group velocity of the internal wave can be calculated to be,

$$\mathbf{C}_g = \frac{(N^2 - f^2) \cos \theta \sin \theta}{|\mathbf{K}| \omega} (\cos \theta, -\sin \theta) \quad (2.30)$$

We can infer that θ is also the angle between constant phase lines and the horizontal axis. We also note that the group velocity and phase speed are perpendicular to each other. The propagation of energy of the internal wave is along the group velocity and therefore, perpendicular to the phase velocity.

2.3 LINEAR REFLECTION OF PLANE INTERNAL WAVES

Let us consider a uniform slope of angle α and a train of plane internal waves with a constant frequency, ω propagating towards the slope. Let us consider the case where the angle between the group velocity and the horizontal for the incident wave, θ , to be greater than the slope angle, α . Since we are considering plane waves, we can introduce a streamfunction, ψ , as,

$$u = \frac{\partial \psi}{\partial y} \quad \text{and} \quad w = -\frac{\partial \psi}{\partial x} \quad (2.31)$$

The streamfunctions of the incident and reflected waves can be written as,

$$\psi_i = \Psi_i e^{i(k_i x + m_i z - \omega_i t)} \quad \text{and} \quad \psi_r = \Psi_r e^{i(k_r x + m_r z - \omega_r t)} \quad (2.32)$$

Since we are considering the linear reflection here, the principle of superposition can be applied and therefore, the total wave field of internal waves reflecting on the slope is given by the sum of the incident and reflected streamlines. The total streamfunction must be a constant at the slope. Without any loss of generality, we can assume the total streamfunction to be zero at the slope. Therefore, along the slope, we have,

$$\psi_i|_{z=x \tan \alpha} + \psi_r|_{z=x \tan \alpha} = \Psi_i e^{i(k_i x + m_i \tan \alpha x - \omega_i t)} + \Psi_r e^{i(k_r x + m_r \tan \alpha x - \omega_r t)} = 0 \quad (2.33)$$

This can be satisfied only if

$$\omega_i = \omega_r \quad \text{and} \quad k_i + m_i \tan \alpha = k_r + m_r \tan \alpha \quad (2.34)$$

Thus we see that the wave frequency and the wave vector parallel to the slope of the internal

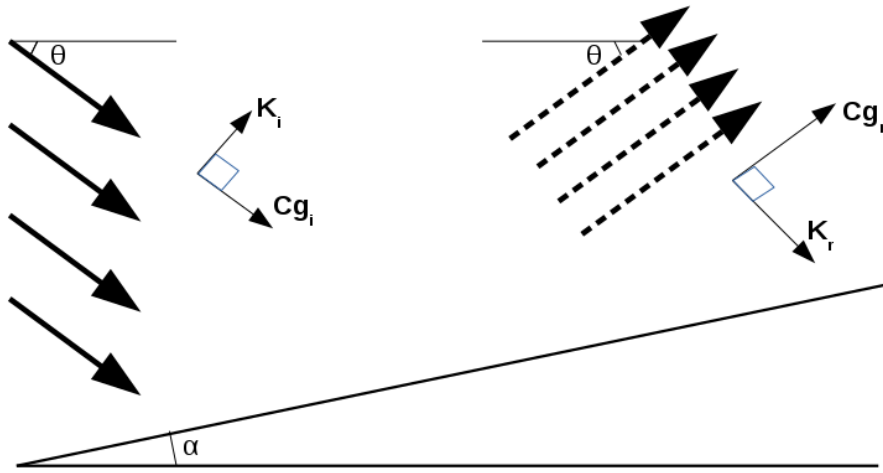


Figure 2.3.1: Schematic of a plane wave reflecting on a slope of angle α . The angle of the incident wave with the horizontal is given by θ and this angle is preserved during reflection. The reflected wave rays are shown in dashed lines. The incident and reflected wave group velocities and wave vectors are given by C_g and \mathbf{K} with respective subscripts.

wave are conserved during the reflection. The conservation of the wave frequency under reflection implies that the angle made by the incident wave with the horizontal is the same as the angle made by the reflected wave with the horizontal, which is unlike the more familiar reflection laws of optics.

Furthermore, from the conservation of the wave vector parallel to the slope, we find that the magnitude of wave vector of the reflected wave is amplified by a factor γ from the wave vector of the incident wave. The amplification factor, γ is given by,

$$\frac{|\mathbf{K}_r|}{|\mathbf{K}_i|} = \frac{\sin(\theta + \alpha)}{\sin(\theta - \alpha)} = \gamma \quad (2.35)$$

The wavelength of the reflected wave is therefore γ times less than that of the incident wave. This would mean that a ray tube reflecting on a sloping boundary may be focused. Since the flux of energy across the tube section is constant, the energy flux should increase upon reflection. Thus, the amplitude of the reflected wave will be γ times more than the amplitude of the incident wave in the linear case.

The reflection we described above is for a shallow slope ($\alpha < \theta$). Such reflections are called sub-critical reflection. If the slope is steep ($\alpha > \theta$), the reflection will be super-critical. In this case the incident wave will get de-focused after reflection. There is a critical condition when $\alpha = \theta$. The linear theory predicts the reflected wave to have infinite amplitude and infinitesimal wavelength. Thus, the linear theory is no more applicable in near critical reflections.

In this thesis, we will be dealing with only sub-critical reflections of internal waves, sufficiently far from the critical condition. Yet, if the amplitude of the incident wave is high enough, nonlinearities cannot be ignored in the reflection process. The incident and reflected wave overlap close to the slope during reflection. The nonlinear interactions of incident and reflected waves can generate higher harmonics and a mean flow. The higher harmonics can further interact resonantly (or not) with the primary waves and cause further energy transfers.

2.4 INTERNAL WAVE BEAMS

Internal wave beams are plane internal waves of finite extent in the wave vector direction. The earliest laboratory experiments using oscillating cylinder in uniformly stratified fluid generates four wave beams in the shape of ‘St Andrew’s cross’, as we mentioned in section 1.4. A localised monochromatic disturbance in a uniformly stratified medium generates internal gravity waves propagating away from the disturbance in the form of wave beams. In two dimensional setting, they form ‘St Andrew’s cross’ and in three dimensional setting they form a double cone structure.

In the oceans, internal tides have been observed to propagate as beams with a finite extent. [Pingree and New \(1989\)](#) were one of the first to observe and report internal wave beams in oceans. They deployed moorings and made a series of semi-diurnal period CTD stations in Bay of Biscay and observed a distinct internal tide beam. The internal tide beam was generated at regions of the continental slope where the slope angle matches the internal wave characteristics. There will be one wave propagating up the slope and another towards the bottom. These beams may reflect upon reaching the surface or the bottom topography. [Pingree and New \(1989\)](#) observed the beam propagating downwards stopping short of the predicted bottom reflection ([Pingree and New, 1991](#)).

Internal wave beams with its finite dimensions provide a localised region of wave-wave interaction when it reflects on a surface or when two different beams collide. Nonlinear interactions in this localised region of interaction can generate higher harmonic internal wave beams. [Teoh et al. \(1997\)](#) have studied the interaction of two colliding internal wave beams using laboratory experiments and [Javam et al. \(2000\)](#) studied internal wave-wave interaction in colliding beams using numerical simulations. They found that nonlinear interactions produced evanescent modes that are trapped in the interaction region. These evanescent modes caused accumulation of energy in the interaction region leading to overturning of the density fields.

Internal tidal beams generated by tidal forcing over mountains was studied using numerical simulations by [Lamb \(2004\)](#). The beams generated can interact nonlinearly while reflecting or colliding to generate new beams of higher harmonics (figure 2.4.1). He finds that the beams are narrower and higher harmonic beams are stronger for supercritical topography (slope of the topography steeper than the propagation angle of the internal waves).

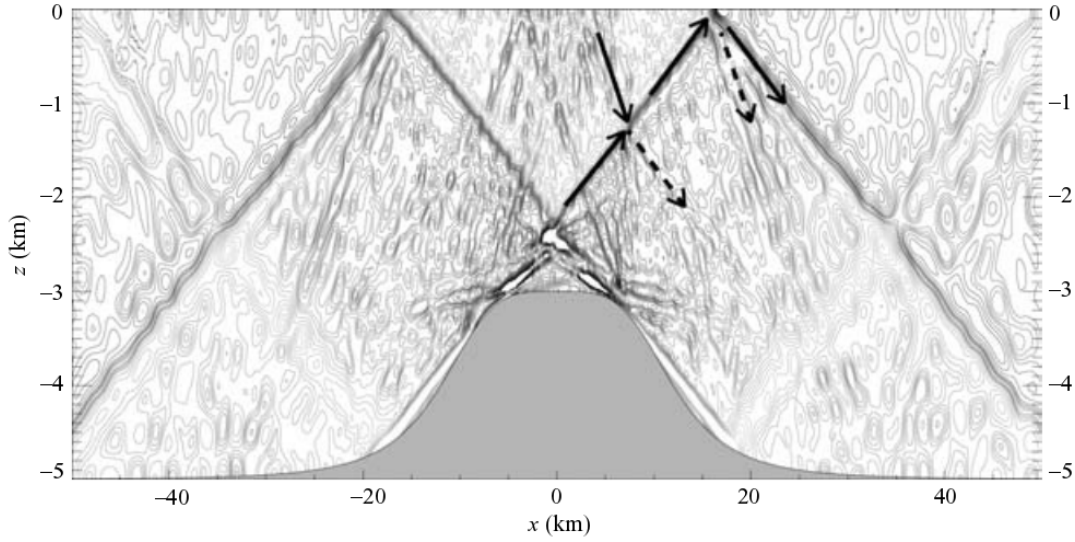


Figure 2.4.1: Horizontal velocity field generated by an oscillating tidal flow over a two-dimensional ridge (Lamb, 2004). Reflections and collisions of internal wave beams are shown by arrows with dashed arrows indicating secondary beams generated by nonlinear interactions. (Image from Tabaei et al. (2005))

Internal wave beams with finite extent in the wave vector direction have been studied for many years, and literature abounds in studies of their interactions and stability. However, internal wave beams of finite extent in lateral direction (in addition to wave vector direction) has been studied only recently. The finite lateral width of the beam allows it to diffract in the horizontal plane. Diffraction introduces lateral variations in the velocity fields allowing for nonlinear interactions of the internal wave beam with itself in the presence of viscosity to produce a mean dipole vortical structure in the horizontal plane (Dauxois et al., 2017). Bordes et al. (2012) performed laboratory experiments, studying wave beams generated using a wave generator (explained in section 1.4) of finite lateral width. They observed strong jet of mean flow in the centre of the wave beam and a recirculating mean flow outside the beam, with a mean dipole vertical vorticity field. They used asymptotic approximations to derive an equation for the evolution of mean vertical vorticity $\overline{\Omega}$ given as follows.

$$\frac{\partial \overline{\Omega}}{\partial t} = \frac{1}{(2 \cos \theta)^2} \frac{\partial A_u^2}{\partial x \partial y} + \nu \nabla^2 \overline{\Omega} \quad (2.36)$$

where A_u is the amplitude of the zonal velocity and θ is the angle made by the wave beam with the horizontal axis. We can note that the acceleration of the mean vertical vorticity is due to the horizontal spatial variation of the amplitude of the zonal velocity. The lateral (y-direction) variation is due to the diffraction of the beam in the horizontal plane and the zonal

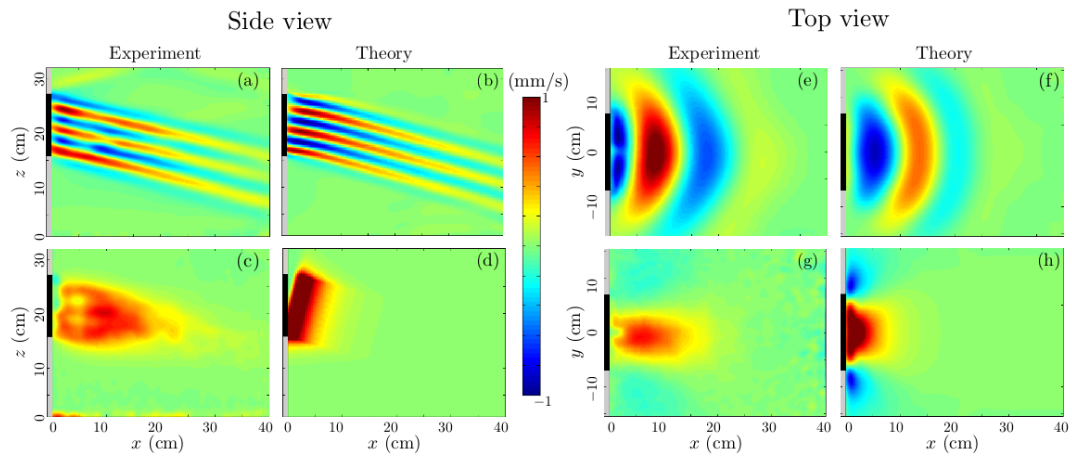


Figure 2.4.2: Comparison of results from the experiment performed by Bordes et al. (2012) (a,c,e,g) and theoretical solutions derived by Kataoka and Akyas (2015) (b,d,f,h). The horizontal u -velocity filtered at the forcing frequency is shown in the top row. The top view figures (e,f) show the finite width in the lateral direction of the wave beam and the resulting diffraction in the horizontal plane. The bottom row shows the Eulerian mean u -velocity. The mean flow can be seen recirculating in the horizontal plane in figures (g,h). The wave generator is shown in grey with its moving part in black. (Image from Dauxois et al. (2017))

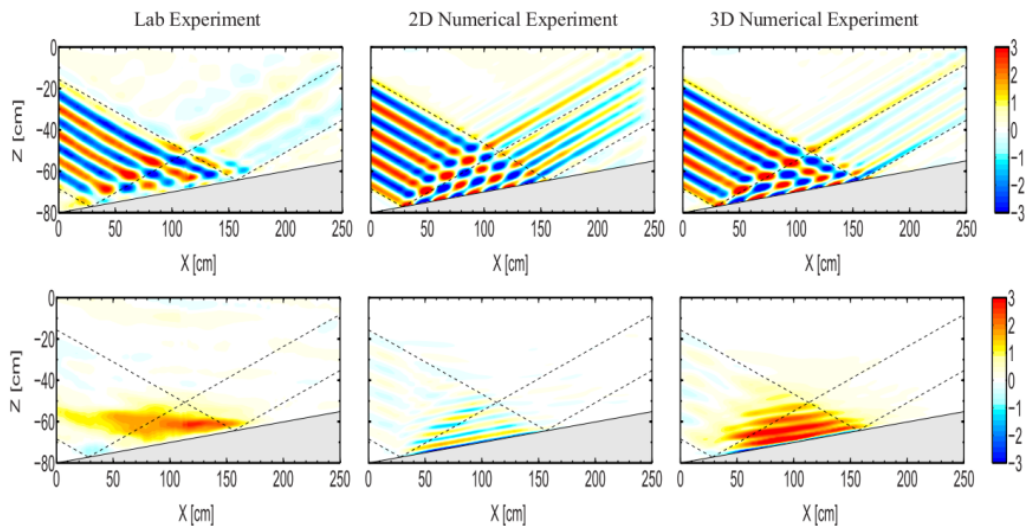


Figure 2.4.3: Comparison of experiment, 2D and 3D numerical simulations of reflection of an internal wave beam (of a finite lateral width in the experiment and 3D simulation). The top row shows the u -velocity ($mm\ s^{-1}$) filtered at the forcing frequency and the bottom row shows the mean u -velocity ($mm\ s^{-1}$). We can notice the strong jet like mean flow in the experiment and 3D simulation due to the finite width of the wave beam. (Image from Grisouard et al. (2013))

variation is due to the viscous attenuation of the beam.

Kataoka and Akylas (2015) used a more rigorous asymptotic theory with appropriate scalings to derive a set of coupled equations for the recirculating mean flow observed by Bordes et al. (2012). The equations of Kataoka and Akylas (2015) for the evolution of mean zonal velocity \bar{u} can be given as follows.

$$\partial_T U_X + \overline{W}_\eta U_X + i \cos \theta \left(\int^\eta \partial_X U_X d\eta' + \frac{\cot \theta}{2} \int^\eta \int^{\eta'} \partial_{Y Y'} U_X d\eta'' d\eta' \right) - \frac{\beta}{2} \partial_{\eta\eta} U_X = \delta(X) f \quad (2.37)$$

$$\partial_T \overline{W}_\eta = i \partial_Y \mathcal{H} \left(\int_{-\infty}^{\infty} \{ \partial_T (U_X^* \partial_\eta U_X) + \beta \partial_\eta U_X^* \partial_{\eta\eta} U_X \} d\eta \right) \quad (2.38)$$

where \mathcal{H} refers to Hilbert transform, U_X and W_η are the complex amplitudes of the scaled along beam and cross beam velocities of the primary harmonic wave beam (\overline{W}_η is the mean cross-beam velocity). Y , η , X and T are the scaled lateral coordinate, cross beam coordinate, along beam coordinate and time, respectively, $\delta(X)$ denotes the delta function, f is the external wave forcing component and β is the scaled viscosity parameter. The above expression clearly shows the importance of viscosity in the generation of recirculating mean flow. The first term in the right hand side is a contribution of unsteadiness. In a quasi-steady case, the horizontal spatial variations of the velocity field of the wave in the presence of viscosity generates the mean flow associated with three-dimensional internal wave beam. The wave beam and the mean flow observed by Bordes et al. (2012) and those predicted by Kataoka and Akylas (2015) are shown in figure 2.4.2.

Three dimensional internal wave beam of finite lateral width reflecting on a slope was studied by Grisouard et al. (2013) (see also Grisouard (2010)). They observed strong jet like mean flow in the centre of the beam close to the slope (figure 2.4.3). The mean flow also recirculates outside the beam. The strong mean flow in the beam centre was observed to be refracting the wave beam close to the slope and the reflected wave is nearly absent.

The worthwhile problems are the ones you can really solve or help solve, the ones you can really contribute something to ... No problem is too small or too trivial if we can really do something about it.

Richard Feynman, Letter to Koichi Mano, February 3, 1966

3

Nonlinear reflection of two-dimensional internal wave beams

THE REFLECTION OF INTERNAL WAVES ON A SLOPE was studied for more than half a century now. The study of ocean mixing and the increasing consensus that internal waves play a key role in enhancing mixing in oceans motivated several studies on interaction of internal waves on ocean topography. The study of nonlinear effects during reflection followed soon. Among them, the inviscid theory of reflection of a train of finite amplitude internal waves from a uniform slope by Thorpe (1987) stands apart due to its seminal work on resonance interactions among the reflecting internal waves and the higher harmonics produced during reflection.

In this chapter, the nonlinear reflection of a finite-width plane internal gravity wave incident onto a uniform slope is addressed, using the two-dimensional inviscid theory of Thorpe (1987). The aim of Thorpe's theory, derived for plane waves of infinite extent, is to determine the conditions under which the incident and the reflected waves may form a resonant triad with the second harmonic wave resulting from their nonlinear interaction. The theory leads to an indeterminacy of the amplitude of the second-order stream function at resonance, which leads to the common conclusion in the literature that this amplitude diverges at resonance. The indeterminacy can be waived and that the amplitude has a finite behaviour at resonance, increasing linearly from the slope, whether rotation is present or not. Thorpe's theory is then revisited for the case of an incident plane wave of finite-width, a simple model of an oceanic internal wave beam. In this case, nonlinear interactions are confined to the area where the incident and reflected waves meet implying that the amplitude of the second-order stream function is now bounded at resonance.

The theory presented in this chapter was developed by Dr. Matthieu Leclair (ETH Zurich)

during his post-doctoral work in LEGI. I performed the numerical simulations to verify Dr. Leclair's theory. The contents of this chapter is being prepared to be submitted to Journal of Fluid Mechanics.

3.1 INTRODUCTION

In the oceans, diapycnal mixing is essential to compensate the deep water formation in high latitudes in order to maintain the meridional overturning circulation. The stable stratification of the oceans makes this diapycnal mixing difficult. It has been showed by Munk (1966) that in order to balance the effects of downward diffusion and upwelling in the ocean, a basin averaged eddy diffusivity of about $10^{-4} m^2 s^{-1}$ is needed. However, from *in situ* measurements (Ledwell et al., 1993), the mixing in the interior of the ocean was observed to be almost an order of magnitude lesser than required.

The nonlinear interactions of internal waves are responsible for the canonical internal wave spectrum and play an important part in the cascade of energy from large scales to small scales by internal waves. The regions close to topographic features in the ocean provide ample opportunities for nonlinear interactions of internal waves to take place. Eriksen (1982) suggests that the increased energy levels at sites such as Muir Sea-mount are due to the reflection of internal waves on the topographic features.

The linear reflection of internal wave plane on a slope was presented in the last chapter. Even in the linear regime, reflection of plane internal waves can induce transfer of energy into smaller scales, as accounted for by a simple geometrical argument proposed by Phillips (1966). The dispersion relation for internal waves in a stratified rotating fluid is (introduced in equation 2.25)

$$\omega^2 = N^2 \sin^2 \theta + f^2 \cos^2 \theta \quad (3.1)$$

where ω is the wave frequency, N is the Brunt-Väisälä frequency of the fluid, assumed to be constant in a uniformly stratified fluid, θ is the angle that the group velocity makes with the horizontal and f is the Coriolis parameter. If the incident wave is propagating onto a slope of angle α (the scalar product of the incident group velocity and the normal to the slope is negative), the wave gets focused upon reflection due to the conservation of the wave frequency and the dispersion relation. If the angle of the slope α is shallower than the angle of propagation of the wave θ , then the reflection is called sub-critical reflection. The incident wave coming on to the slope gets reflected up away from the slope. If the slope is steeper so that $\theta < \alpha$, the reflection is called a super-critical reflection and the reflected wave propagate downwards. A critical case exists when θ is close to α . In this case, focusing leads to strongly nonlinear processes close to the boundary (McPhee-Shaw and Kunze, 2002, Dauxois and Young, 1999, Chalamalla et al., 2013); organised structures sometimes referred to as bores are then observed (Hosegood and van Haren, 2004).

The nonlinear processes were assumed to be weak for cases that are not close to the critical condition. However, Thorpe (1987) showed that the incident and the reflected plane waves can form a resonant triad with a second harmonic wave resulting from the interaction of these

waves. He used asymptotic expansion method to derive a solution for the second harmonic and explored the conditions for the resonant interactions. This result is valid when the slope is inclined ($\alpha \neq 0$) as no harmonics are produced when the incident plane wave reflects on a flat surface (Thorpe, 1968).

However, as we mentioned in the last chapter, in many of the natural flows, internal waves propagate as beams rather than plane waves (see section 2.4). Internal tides propagate as beams whose width is determined by the dimension of the source. When internal waves propagate as beams, harmonics motions are produced when a beam incident on a surface (whether flat or not) interacts with the reflected beam. A single beam is a solution of the inviscid Boussinesq equations (Tabaei and Akylas, 2003) while the superposition of two beams is not; this implies that harmonics will be generated close to the boundary, where the beams interact (Tabaei et al., 2005).

Tabaei et al. (2005) derived theoretical expressions of the higher-order harmonics generated by a time-harmonic beam reflecting on a simple slope; colliding beams located in the same plane were also considered. The generation of higher harmonics by beams (or by finite-width waves) reflecting either on a flat surface or on an inclined boundary have been addressed in several numerical and experimental works performed in a two-dimensional (or quasi-two-dimensional) vertical geometry (Gostiaux et al., 2006, Gostiaux, 2006, Echeverri et al., 2009, Paireaud et al., 2010, Rodenborn et al., 2011, e.g.). In Gostiaux et al. (2006), a finite-width incident wave field was produced by the wave generator referred to above and the structure of the higher harmonics was analysed. Rodenborn et al. (2011) considered a beam reflecting on a simple slope and investigated empirically the conditions that lead to the largest amplitude of the second harmonic wave.

This chapter examines the validity of the theory of Thorpe (1987) when the conditions of a resonant triad involving an incident and a reflected wave and their second-order harmonic wave are met for internal wave beams in a stratified and rotating fluid. In the first part of the chapter, we revisit that theory when resonance conditions are met, first by considering a monochromatic plane wave reflecting on a uniform slope. At resonance, it is unclear whether Thorpe (1987) theory predicts a finite amplitude of the second harmonic wave because the expression of this amplitude involves an indeterminacy: the numerator and denominator both vanish, which leads to the common inference in the literature that this amplitude is unbounded at resonance. In the second part, the predictions of Thorpe (1987) are considered when a wave packet of finite width (rather than a plane wave of infinite extent considered in the theory), to model the incident wave field generated in the laboratory experiments, reflects on a uniform slope. These predictions are next compared to the results of the two-dimensional numerical simulations, where viscous effects are present.

3.2 NONLINEAR REFLECTION OF A PLANE WAVE

The governing equations are presented in equations 5.1. Using the definition for buoyancy as given in equation 2.18 we can write them as follows.

$$\frac{\partial \mathbf{u}}{\partial t} + \mathbf{u} \cdot \nabla \mathbf{u} = -\nabla p - f \hat{\mathbf{e}}_z \times \mathbf{u} + b \hat{\mathbf{e}}_z \quad (3.2a)$$

$$\frac{\partial b}{\partial t} + \mathbf{u} \cdot \nabla b + N^2 w = 0 \quad (3.2b)$$

$$\nabla \cdot \mathbf{u} = 0 \quad (3.2c)$$

where \mathbf{u} is the velocity vector, p is the pressure and ρ is the density with ρ_0 is a reference density.

At the slope, we have the boundary condition of no flux through the slope which we can write as,

$$\mathbf{u} \cdot \mathbf{n}|_{slope} = 0 \quad (3.3)$$

Since the wave is infinite in the lateral direction, we can assume that $\partial/\partial y = 0$. This will let us use a streamfunction in the x-z plane defined as $u = \partial\psi/\partial z$ and $w = -\partial\psi/\partial x$. The definition of the streamfunction ensures that the continuity equation is satisfied. We can re-write the governing equations 5.1 using the streamfunction as,

$$\frac{\partial}{\partial t} \nabla^2 \psi + \frac{\partial b}{\partial x} - f \frac{\partial v}{\partial z} = J(\psi, \nabla^2 \psi) \quad (3.4a)$$

$$\frac{\partial v}{\partial t} + f \frac{\partial \psi}{\partial z} = J(\psi, v) \quad (3.4b)$$

$$\frac{\partial b}{\partial t} - N^2 \frac{\partial \psi}{\partial x} = J(\psi, b) \quad (3.4c)$$

where J is the Jacobian operator defined by

$$J(a, b) = \frac{\partial a}{\partial x} \frac{\partial b}{\partial z} - \frac{\partial a}{\partial z} \frac{\partial b}{\partial x} \quad (3.5)$$

We can combine the equations 3.4 by taking the time derivative of equation 3.4(a) and replacing the v and b terms using equations 3.4(b) and 3.4(c). The resulting equation is as follows.

$$\frac{\partial^2}{\partial t^2} \nabla^2 \psi + N^2 \frac{\partial^2 \psi}{\partial x^2} + f^2 \frac{\partial^2 \psi}{\partial z^2} = \frac{\partial}{\partial t} J(\psi, \nabla^2 \psi) - \frac{\partial}{\partial x} J(\psi, b) + f \frac{\partial}{\partial z} J(\psi, v) \quad (3.6)$$

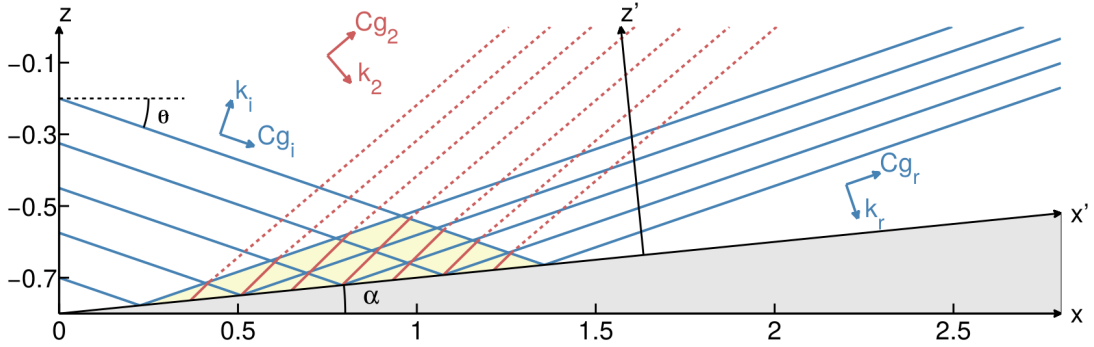


Figure 3.2.1: Sketch of the interaction between the incident and reflected waves in the (x, z) plane. The incident and reflected wave beams are indicated by blue lines and the second harmonic wave beam is indicated by red lines. The along slope and normal to slope coordinates (x' and z') are also shown.

We can rotate our coordinate system by the slope angle so that we have the coordinates (x', z') where x' is the along-slope coordinate and z' is the normal-slope coordinates. They are defined as,

$$x' = x \cos \alpha + z \sin \alpha \quad (3.7a)$$

$$z' = z \cos \alpha - x \sin \alpha \quad (3.7b)$$

The along-slope and normal-slope wavenumbers in this coordinate system can be written as k and nk . This is to make further calculations simpler as the along-slope wavenumber k is conserved during reflection. Then, the dispersion relation can be written as follows.

$$\omega^2 = N^2 \sin^2 \theta + f^2 \cos^2 \theta = N^2 \frac{(n \sin \alpha - \cos \alpha)^2}{1 + n^2} + f^2 \frac{(\sin \alpha + n \cos \alpha)^2}{1 + n^2} \quad (3.8)$$

This leads to a quadratic equation in n , in which N and f disappear (for $N \neq f$). The two roots of the resulting quadratic equation are,

$$n_I = \frac{\sin \theta \cos \theta - \sin \alpha \cos \alpha}{\sin^2 \theta - \sin^2 \alpha} \quad (3.9a)$$

$$n_R = -\frac{\sin \theta \cos \theta + \sin \alpha \cos \alpha}{\sin^2 \theta - \sin^2 \alpha} \quad (3.9b)$$

These roots correspond to the normal-slope wavenumber of the incident and reflected waves respectively.

We can non-dimensionalise the equations 3.4(b), (c) and 3.6 using the amplitude of the incident wave velocity U , as a velocity scale, its wavelength λ as a length scale and $1/N$ as a time scale. A Froude number can be defined using these scales as, $Fr = U/\lambda N$, which

may be interpreted as a non-dimensional amplitude of the incident wave velocity. The equations 3.4(b), (c) and 3.6 after non-dimensionalising and rotating the coordinate system can be written as follows.

$$\begin{aligned} \frac{\partial^2}{\partial t^2} \nabla^2 \psi + N^2 \left(\cos \alpha \frac{\partial}{\partial x'} - \sin \alpha \frac{\partial}{\partial z'} \right)^2 \psi + f^2 \left(\sin \alpha \frac{\partial}{\partial x'} + \cos \alpha \frac{\partial}{\partial z'} \right)^2 \psi = \\ Fr \left[\frac{\partial}{\partial t} J(\psi, \nabla^2 \psi) - \left(\cos \alpha \frac{\partial}{\partial x'} - \sin \alpha \frac{\partial}{\partial z'} \right) J(\psi, b) + \right. \\ \left. f \left(\sin \alpha \frac{\partial}{\partial x'} + \cos \alpha \frac{\partial}{\partial z'} \right) J(\psi, v) \right] \end{aligned} \quad (3.10a)$$

$$\frac{\partial v}{\partial t} + f \left(\sin \alpha \frac{\partial}{\partial x'} + \cos \alpha \frac{\partial}{\partial z'} \right) \psi = Fr J(\psi, v) \quad (3.10b)$$

$$\frac{\partial b}{\partial t} - N^2 \left(\cos \alpha \frac{\partial}{\partial x'} - \sin \alpha \frac{\partial}{\partial z'} \right) \psi = Fr J(\psi, b) \quad (3.10c)$$

We have the boundary condition on the slope which can be written as,

$$\left. \frac{\partial \psi}{\partial x'} \right|_{z'=0} = 0 \quad (3.11)$$

We can consider Fr as a small parameter (i.e. $Fr \ll 1$), that is to assume that the wave dynamics are weakly nonlinear. The ψ , b and v fields can thus be decomposed into a multiple scale expansion as

$$\psi = \psi_1 + Fr\psi_2 + o(Fr^2) \quad (3.12a)$$

$$b = b_1 + Frb_2 + o(Fr^2) \quad (3.12b)$$

$$v = v_1 + Frv_2 + o(Fr^2) \quad (3.12c)$$

Introducing these expansions in the equations of motion 3.10, the resulting equations can be solved order by order, by matching terms multiplied by the same power of Fr . At each order the solution satisfies the same linear operator with a right hand side determined by lower order nonlinear terms. Identifying terms multiplied by Fr_0 , the first-order fields ψ_1 , v_1 and b_1 are thus found to satisfy the homogeneous linear wave equations. Matching terms multiplied by Fr shows that the second-order fields ψ_2 , v_2 and b_2 are solutions of the same linear operator forced by nonlinear terms solely involving the first-order fields. The detailed calculations associated with this general principle are now presented.

3.2.1 FIRST ORDER SOLUTION

The first order equation for ψ_1 is given by,

$$\frac{\partial^2}{\partial t^2} \nabla^2 \psi_1 + N^2 \left(\cos \alpha \frac{\partial}{\partial x'} - \sin \alpha \frac{\partial}{\partial z'} \right)^2 \psi_1 + f^2 \left(\sin \alpha \frac{\partial}{\partial x'} + \cos \alpha \frac{\partial}{\partial z'} \right)^2 \psi_1 = 0 \quad (3.13)$$

with the boundary condition on the slope given by,

$$\frac{\partial \psi_1}{\partial x'} \Big|_{z'=0} = 0 \quad (3.14)$$

We seek solutions of the kind of a monochromatic plane waves with wavenumbers k and $n_I k$ and frequency ω . The dispersion relation has two roots, implying that the solution ψ is a linear superposition of waves with normal-slope wavenumbers $n_I k$ and $n_R k$. After applying the boundary condition 3.11, we get

$$\psi_1 = a_1 \{ \sin(kx' + n_I kz' - \omega t) - \sin(kx' + n_R kz' - \omega t) \} \quad (3.15)$$

The first-order stream function is therefore the sum of a wave incident onto the slope, which we denote for simplicity as $(k, n_I k, \omega)$, and of its reflected counterpart $(k, n_R k, \omega)$. The wave amplitude a_1 is arbitrary. ψ_1 is also defined up to a constant additional phase, chosen to be 0 in the present case, which does not imply any loss of generality.

Once ψ_1 is known, v_1 and b_1 are inferred from the equations

$$\frac{\partial v_1}{\partial t} + f \left(\sin \alpha \frac{\partial}{\partial x'} + \cos \alpha \frac{\partial}{\partial z'} \right) \psi_1 = 0 \quad (3.16)$$

and

$$\frac{\partial b_1}{\partial t} - N^2 \left(\cos \alpha \frac{\partial}{\partial x'} - \sin \alpha \frac{\partial}{\partial z'} \right) \psi_1 = 0 \quad (3.17)$$

which yields

$$v_1 = \frac{a_1 f k}{\omega} \{ (\sin \alpha + n_I \cos \alpha) \sin(kx' + n_I kz' - \omega t) - (\sin \alpha + n_R \cos \alpha) \sin(kx' + n_R kz' - \omega t) \} \quad (3.18)$$

and

$$b_1 = -\frac{a_1 N^2 k}{\omega} \{ (\cos \alpha - n_I \sin \alpha) \sin(kx' + n_I kz' - \omega t) - (\cos \alpha - n_R \sin \alpha) \sin(kx' + n_R kz' - \omega t) \} \quad (3.19)$$

3.2.2 SECOND ORDER SOLUTION

Matching terms proportional to Fr in equations 3.10 gives the equations for the second-order component. The equation for ψ_2 is

$$\begin{aligned} \frac{\partial^2}{\partial t^2} \nabla^2 \psi_2 + N^2 \left(\cos \alpha \frac{\partial}{\partial x'} - \sin \alpha \frac{\partial}{\partial z'} \right)^2 \psi_2 + f^2 \left(\sin \alpha \frac{\partial}{\partial x'} + \cos \alpha \frac{\partial}{\partial z'} \right)^2 \psi_2 = \\ Fr \left[\frac{\partial}{\partial t} J(\psi_1, \nabla^2 \psi_1) - \left(\cos \alpha \frac{\partial}{\partial x'} - \sin \alpha \frac{\partial}{\partial z'} \right) J(\psi_1, b_1) + \right. \\ \left. f \left(\sin \alpha \frac{\partial}{\partial x'} + \cos \alpha \frac{\partial}{\partial z'} \right) J(\psi_1, v_1) \right] \end{aligned} \quad (3.20)$$

with the boundary condition

$$\frac{\partial \psi_2}{\partial x'} \Big|_{z'=0} = 0 \quad (3.21)$$

The solution of equation 3.20 is given by,

$$\begin{aligned} \psi_2 = 3a_1^2 k^2 \omega \frac{\sin^2 \theta \cos^2 \theta \sin \alpha \cos \alpha}{(\sin^2 \theta - \sin^2 \alpha) D} \{ \sin(2kx' + m_2 kz' - \omega t) - \\ \sin(2kx' + (n_I + n_R)kz' - \omega t) \} \\ - \frac{a_1^2 k^2}{\omega} \frac{\sin \theta \cos \theta}{\sin^2 \theta - \sin^2 \alpha} \sin((n_I - n_R)kz') \end{aligned} \quad (3.22)$$

with

$$\begin{aligned} D = N^2 \sin^2 \theta (4 \sin^4 \theta - 7 \sin^2 \theta \sin^2 \alpha + 4 \sin^2 \alpha - \sin^2) + \\ f^2 \cos^2 \theta (4 \sin^4 \theta - 7 \sin^2 \theta \sin^2 \alpha + 3 \sin^2 \alpha) \end{aligned} \quad (3.23)$$

and

$$\begin{aligned} m_2 = \frac{2\sqrt{4 \sin^2 \theta N^4 (1 - 4 \sin^2 \theta) + 4 \cos^2 \theta f^4 (1 - 4 \cos^2 \theta) + N^2 f^2 (3 - 32 \sin^2 \theta \cos^2 \theta)}}{N^2 (4 \sin^2 \theta - \sin^2 \alpha) + f^2 (4 \cos^2 \theta - \cos^2 \alpha)} \\ - \frac{2 \sin \alpha \cos \alpha (N^2 - f^2)}{N^2 (4 \sin^2 \theta - \sin^2 \alpha) + f^2 (4 \cos^2 \theta - \cos^2 \alpha)} \end{aligned} \quad (3.24)$$

The second-order stream function in equation 3.22 is the sum of an oscillatory component (for $\alpha \neq 0$) and a steady component. The oscillatory component, referred to as the second harmonic wave in the introduction, is made of two terms, associated with the waves $(2k, m_2 k, 2\omega)$ and $(2k, (n_I + n_R)k, 2\omega)$. The former term is the solution of the homogeneous equation associated with equation 3.20 so that the wave $(2k, m_2 k, 2\omega)$ satisfies the

dispersion relation and radiates energy away from the boundary. This term is called a “free wave” by Thorpe (1987). The equation 3.22 is obtained by adding to this homogeneous solution a particular solution of the complete equation, referred to as a “forced” wave by Thorpe (1987), and by prescribing the homogeneous solution parameters through the boundary condition 3.21. The forced wave becomes a free wave when $(2k, (n_I + n_R)k, 2\omega)$ satisfies the dispersion relation, namely when $n_I + n_R = m_2$; in this case, the incident, reflected and second harmonic waves form a resonant triad. A sketch of the interaction between the incident and reflected waves for conditions close to resonance is displayed in figure 3.2.1.

The steady component of equation 3.22 is an Eulerian mean current opposing the Stokes drift associated with the first-order solution (3.15,3.18,3.19), as stated by Thorpe (1987) and Thorpe (1997). Hence the total Lagrangian mean flow, which is the sum of the Eulerian mean flow and of the Stokes drift (Longuet-Higgins, 1969), is zero. Indeed, because of the sloping boundary, there cannot be any horizontal mass transport in the present two-dimensional configuration, implying that the Lagrangian mean flow must vanish.

We now consider the oscillatory component of the second order solution, denoted as ψ_2^h . The denominator of its amplitude goes to 0 for values of (α, θ) satisfying $D = 0$. For $f = 0$, these values span the intervals $[0, 8.21^\circ]$ for α and $[0, 30^\circ]$ for θ , these ranges shrinking to empty intervals as f/N increases and reaches 0.5. As stated in Thorpe (1987), the condition $D = 0$ also corresponds to the case of a resonant triad between the primary incident and reflected waves and the second harmonic free wave. Since $m_2 = n_I + n_R$ in this case, as just discussed, the oscillatory component in equation 3.22 is an indeterminate form $0/0$ as $D \rightarrow 0$. One aim of the present paper is to remove this indeterminacy to clarify the behaviour of the oscillatory component at resonance. For this purpose, we rewrite the oscillatory component of ψ_2 as

$$\psi_2^h = \underbrace{\left[6a_1^2 k^2 \omega \frac{\sin^2 \theta \cos^2 \theta \sin \alpha \cos \alpha \sin(\delta k z')}{(\sin^2 \theta - \sin^2 \alpha) D} \right]}_{\text{amplitude of the second harmonic wave}} \cos(2kx' + (m_2 - \delta)kz' - 2\omega t) \quad (3.25)$$

where $\delta = \frac{1}{2}(m_2 - (n_I + n_R))$. For $\alpha \neq 0$, as $D \rightarrow 0$, it can be shown that,

$$\delta \approx \frac{D}{6 \sin \alpha \cos \alpha (\sin^2 \theta - \sin^2 \alpha) \omega^2} \quad (3.26)$$

so that

$$\lim_{D \rightarrow 0} \frac{\sin(\delta k z')}{D} = \frac{k z'}{6 \sin \alpha \cos \alpha (\sin^2 \theta - \sin^2 \alpha) \omega^2} \quad (3.27)$$

Therefore, as $D \rightarrow 0$, the second harmonics wave becomes as follows.

$$\psi_2^h = \underbrace{\left[\frac{a_1^2 k^2}{\omega} \frac{\sin^2 \theta \cos^2 \theta}{(\sin^2 \theta - \sin^2 \alpha)^2} k z' \right]}_{\text{amplitude at resonance}} \cos(2kx' + (n_I + n_R)kz' - 2\omega t) \quad (3.28)$$

The amplitude of the second harmonic wave is thus a periodic function of the distance from the slope z' whose period $2\pi/\delta k$ goes to infinity as (α, θ) approaches the resonance condition $D = 0$. In this case, the amplitude grows linearly from the slope and is therefore unbounded.

This unbounded amplitude is not physical and is due to the weakly nonlinear character of the theory: the second-order solution is generated by the nonlinear first-order terms so that the second-order wave receives energy from the first-order ones. However the latter is not modified by this energy loss. Hence, at resonance, the second harmonic wave is continuously fed during its propagation by the unaltered primary wave.

3.3 RESONANT INTERACTIONS FOR NONLINEAR REFLECTION OF A WAVE BEAM

The results presented in section 3.2.2 have been obtained for a plane wave of infinite extent, namely the wave is spatially and temporally monochromatic. As discussed in the Introduction, the motivation of the present work was to examine the validity of the theory of Thorpe (1987) for a resonant triad using joint laboratory and numerical experiments using a wave generator device in the experiments. From a theoretical point of view, the incident wave field thus generated is simply modelled as a plane wave with a finite number of wavelengths in the direction normal to wave propagation. In the remainder of the paper, we rely on Thorpe (1987) theory to estimate the amplitude of the second-order wave amplitude where resonant conditions are met for this generation method and compare the theoretical predictions with numerical simulations for an incident wave with various widths.

We recall that, to be valid, the theory requires the amplitude of $Fr\psi_2$ to stay small with respect to the amplitude of ψ_1 . We thus scale the amplitude of $Fr\psi_2^h$ with that of ψ_1 . More precisely, we scale $Fr\|\psi_2^h\|$ by $\|\psi_1\|$ where norm $\|\cdot\|$ is the infinity norm in space and time. This norm is defined by $\|\psi\| = \|\psi\|_{\infty, \Omega \times \mathbb{R}} = \max_{(x,t) \in \Omega \times \mathbb{R}} |\psi|$, where Ω is the interaction domain between the incident and reflected waves represented by the yellow triangle in figure 3.2.1. At resonance, the amplitude of ψ_2^h should reach a maximum value at the largest distance from the slope in the interaction area, which coincides with the top of the yellow triangle. We thus compute the ratio

$$R^{th} = \frac{Fr\|\psi_2^h\|}{\|\psi_1\|}, \quad (3.29)$$

the th superscript standing for theoretical. Our purpose here is (i) to examine the dependence of this ratio upon the number of wavelengths in the incident wave and (ii) to investi-

gate the conditions under which the theory is strictly valid (namely $R^{th} \ll 1$).

Let us compute $\|\psi_1\|$ and $\|\psi_2^h\|$. If one rewrites ψ_1 in the same way as ψ_2^h ,

$$\psi_1 = 2a_1 \sin\left(\frac{n_I - n_R}{2}kz'\right) \cos\left(kx' + \frac{n_I + n_R}{2}kz' - \omega t\right), \quad (3.30)$$

the expressions of $\|\psi_1\|$ and $\|\psi_2^h\|$ are given by

$$\|\psi_1\| = 2a_1 \max_{0 \leq kz' \leq kh} \left\{ \sin\left(\frac{n_I - n_R}{2}kz'\right) \right\} \quad (3.31a)$$

$$\text{and } \|\psi_2^h\| = 6a_1^2 k^2 \omega \frac{\sin \theta \cos \theta \sin \alpha \cos \alpha}{\sin \theta - \sin \alpha} \max_{0 \leq kz' \leq kh} \left\{ \frac{\sin(\delta kz')}{D} \right\}, \quad (3.31b)$$

where h is the height of the interaction triangle normal to the slope. Introducing n_λ , the number of wavelengths contained in the primary wave, and thanks to simple trigonometric calculations, one can show that

$$kh = 2\pi \frac{\sin(\theta - \alpha) \sin(\theta + \alpha)}{\sin(2\theta)} n_\lambda = 2\pi \frac{(\sin \theta - \sin \alpha)}{\sin(2\theta)} n_\lambda = \frac{2\pi}{n_I - n_R} n_\lambda. \quad (3.32)$$

This result implies that $0.5(n_I - n_R)kz' \leq \pi n_\lambda$ for $0 \leq kz' \leq kh$. Since $n_\lambda \geq 1$, it ensures that $\max_{0 \leq kz' \leq kh} \left\{ \sin(0.5(n_I - n_R)kz') \right\} = 1$ and leads to $\|\psi_1\| = 2a_1$. Note that the first equality of equation 3.32 is in agreement with Thorpe (2001).

The expression of $\|\psi_2^h\|$ cannot be simplified in the same way, especially when considering the situation of (α, θ) close to the resonant triad case where $\delta \rightarrow 0$. For simplicity, we introduce

$$M = \max_{0 \leq kz' \leq kh} \left\{ \frac{\sin(\delta kz')}{D} \right\} \quad (3.33)$$

$$M = \begin{cases} kh/(6 \sin \alpha \cos \alpha (\sin \theta - \sin \alpha) \omega^2) & \text{if } D = 0 \\ 1/D & \text{if } D \neq 0 \text{ and } \delta kh > \pi/2 \\ \sin(\delta kh)/D & \text{if } D \neq 0 \text{ and } \delta kh \leq \pi/2. \end{cases} \quad (3.34)$$

(We recall that a second-order oscillatory component is generated when $\alpha \neq 0$, which is assumed here.) A measure of the ratio between the second harmonic wave and the first-order solution is thus given by

$$R^{th} = 3Fra_1 k^2 \omega \frac{\sin \theta \cos \theta \sin \alpha \cos \alpha}{\sin \theta - \sin \alpha} M. \quad (3.35)$$

For the sake of completeness, we provide the expressions of the non-dimensional quanti-

ties a_1 , k and ω with the scaling defined in section 3.2

$$a_1 = 1/2\pi, \quad k = 2\pi \sin(\alpha + \theta), \quad \omega = \sqrt{\sin \theta + (f/N)^2 \cos \theta}, \quad (3.36)$$

while N and f become equal to 1 and f/N , respectively. In the following, the parameter f/N is denoted as γ . With this scaling, the expression of R^{th} becomes:

$$R^{th} = 6\pi Fr \frac{\sqrt{\sin \theta + \gamma^2 \cos \theta} \sin(\theta + \alpha) \sin \theta \cos \theta \sin \alpha \cos \alpha}{\sin(\theta - \alpha)} M. \quad (3.37)$$

R^{th} is proportional to Fr and depends upon the angles α and θ and upon the ratio f/N . Note that, at resonance ($D = 0$), R^{th} is also proportional to the number of wavelengths n_λ (through equation 3.32). This implies that, as $n_\lambda \rightarrow \infty$, this ratio may well become much larger than 1 since Fr and n_λ are independent parameters. Hence the internal wave reflection problem is highly nonlinear at resonance, which figures 3.3.1(a) below attest.

Figure 3.3.1(a) displays R^{th} in a (α, β) diagram for $\gamma = 0$ (no rotation), $Fr = 0.005$ and for four different values of n_λ equal to 1, 2, 4 and 8. These values, except for $n_\lambda = 8$, are those of the numerical simulations reported in section 3.5. The counterpart diagram for $\gamma = 0.2$ is displayed in figure 3.3.1(a). Both figures show that, even if the Froude number is quite low and n_λ is at most equal to 8, R^{th} reaches in all cases values close to unity at resonance. Figure 3.3.1(a) also shows that the location of resonant triads (marked with a dashed curve) differs from the location where R^{th} reaches a maximum value for small values of n_λ , both locations superimposing as n_λ grows. In other words, we recover the predictions of Thorpe (1987) in the limit of infinite plane waves. The latter statement is confirmed in figure 3.5.4, further discussed in section 3.5, where R^{th} is plotted versus α for $n_\lambda = 1, 2$ and 4 (for the value of $\theta = 18.9^\circ$ considered in the numerical simulations) for $n_\lambda \geq 2$, R^{th} displays a maximum which is all the more pronounced n_λ is larger, and is reached for a value of α that approaches the theoretical value at which resonance occurs when n_λ increases. Thus, the second harmonic resonance in the sense of a pronounced local maximum for R^{th} in the (α, θ) plane only arises for high values of n_λ which are not likely to occur in reality.

Finally, figure 3.3.1(b) shows that rotation does not qualitatively modify the resonance process, only making this maximum lower than in the non-rotating case. This behaviour can be explained with equation 3.22. The influence of Coriolis effects in the second-order stream function amplitude at resonance only comes into play through the frequency ω in the denominator of the expression of ψ_2^h . All parameters being kept the same, adding rotation increases ω and therefore lowers the second-order amplitude.

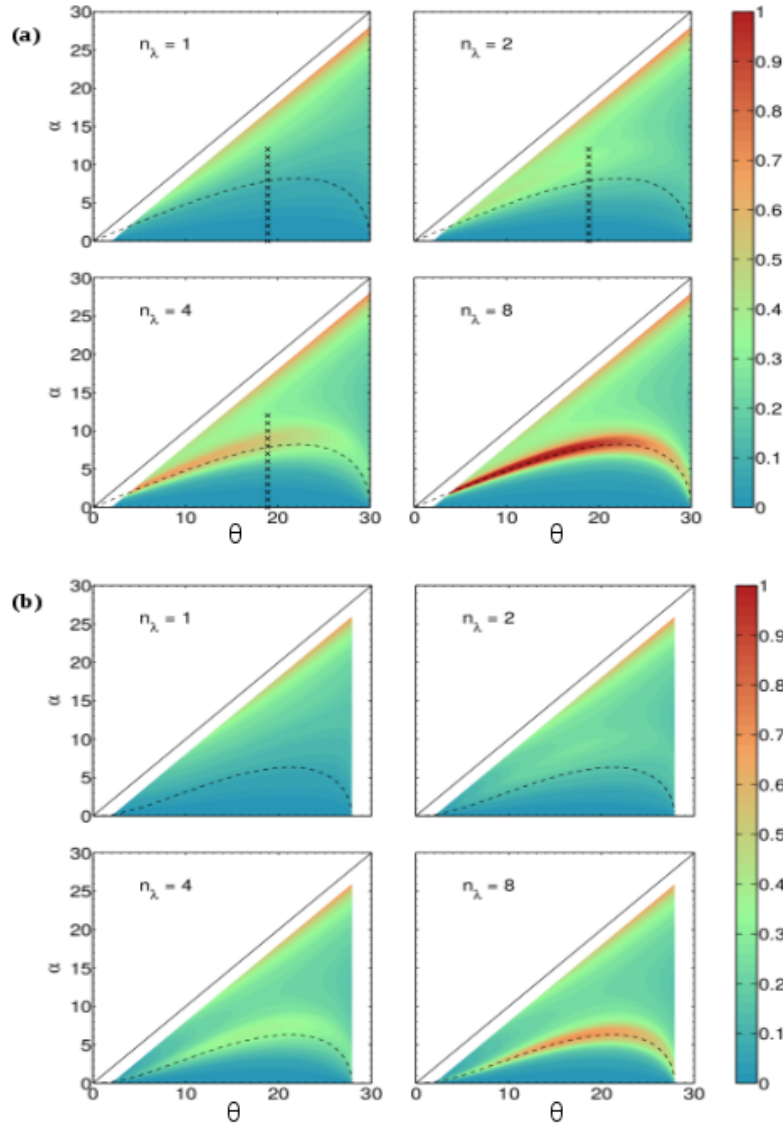


Figure 3.3.1: (a) Ratio of the second-order to the first-order stream function norms R^{th} , defined by (3.37), as a function of the slope angle α and incidence angle θ for a Froude number $Fr = 0.005$, in the non-rotating case ($\gamma = 0$) and for various widths n_λ , with n_λ being the number of wavelengths of the incident wave. The dashed line represents the location where resonance occurs between the incident, reflected and second harmonic waves, as predicted by Thorpe (1987) for an incident wave of infinite extent (corresponding to $n_\lambda \rightarrow \infty$). The crosses refer to numerical simulations reported in section 3.5. The domain is limited to $\theta \leq 30^\circ$ because the second harmonic free wave becomes evanescent above this range. Values of R^{th} are also not plotted when approaching the critical case $\alpha = \theta$ which is beyond the scope of our interest here. (b) Same as in (a), but for a ratio f/N equal to 0.2.

3.4 EULERIAN MEAN FLOW AND STOKES DRIFT

In this section, we quickly demonstrate a statement of [Thorpe \(1987\)](#), namely that there is no mass transport associated with the along slope steady current

$$\psi_2^m = -\frac{a_1^2 k^2}{\omega} \frac{\sin \theta \cos \theta}{\sin^2 \theta - \sin^2 \alpha} \sin((n_I - n_R)kz') \quad (3.38)$$

$$u_2^m = \frac{\partial \psi_2^m}{\partial z'} = -2 \frac{a_1^2 k^3}{\omega} \frac{\sin^2 \theta \cos^2 \theta}{(\sin^2 \theta - \sin^2 \alpha)^2} \cos((n_I - n_R)kz') \quad (3.39)$$

This Eulerian current is indeed found to be compensated by the Stokes drift associated with the first harmonic wave (where the incident and reflected waves superpose).

Let $\mathbf{u}_1 = (u_1, w_1) = (\partial \psi_1 / \partial z', -\partial \psi_1 / \partial x')$ be the velocity field of this first harmonic wave. Assuming that fluid parcel displacements are small compared with the length scale over which \mathbf{u}_1 varies, the Stokes drift is defined by ([Longuet-Higgins, 1969](#))

$$u_2^{sd} = \overline{\left(\int_{t_0}^t u_1(s) ds \right) \frac{\partial u_1}{\partial x'}} + \overline{\left(\int_{t_0}^t w_1(s) ds \right) \frac{\partial u_1}{\partial z'}} \quad (3.40a)$$

and

$$w_2^{sd} = \overline{\left(\int_{t_0}^t u_1(s) ds \right) \frac{\partial w_1}{\partial x'}} + \overline{\left(\int_{t_0}^t w_1(s) ds \right) \frac{\partial w_1}{\partial z'}} \quad (3.40b)$$

where the overbar designates the time average over one wave period. Using the expression of ψ_1 given by [3.15](#) yields

$$u_2^{sd} = -u_2^s \quad \text{and} \quad w_2^{sd} = 0. \quad (3.41)$$

3.5 NUMERICAL SIMULATIONS

In order to estimate the validity of the theoretical predictions exposed in the previous section, two-dimensional numerical simulations have been performed. As just discussed, including rotation does not qualitatively change the results so that the non-rotating case is considered in the present section. All quantities below are dimensional but we keep the same notation as before for the variables and parameters, for simplicity. The term *first harmonic wave* refers to the superposition of the incident and reflected waves.

3.5.1 NUMERICAL CONFIGURATION

The simulations were performed with the numerical model NHOES (Non Hydrostatic Ocean model for Earth Simulator) which solves the free-surface non-hydrostatic Boussinesq equations in a Cartesian coordinate system ([Aiki and Yamagata, 2004](#)). A brief summary of the

numerical model is given in appendix A1. For the present study, equations 5.1 were solved with a viscous term $\nu \nabla^2 \mathbf{u}$ added to the right-hand-side of equation (5.1a) and a diffusive term $\kappa \nabla^2 b$ to that of equation (5.1b); ν and κ are the kinematic viscosity and the diffusivity, respectively. The equation of state is linear and only depends on salinity. The choice of salinity rather than temperature is dictated by laboratory experiments conducted in parallel to the present study in which density variations are created by a vertical profile of salt concentration. The diffusivity is thus set to $1.49 \cdot 10^{-9} m^2 s^{-1}$ while the viscosity is equal to $\nu = 1 \times 10^{-6} m^2 s^{-1}$ (since the Prandtl number of salt dissolved in water is about 700). No sub-grid scale parameterisation is used. The background stratification is linear, with a value of the Brunt-Väisälä frequency equal to $0.46 s^{-1}$ and, as said above, the Coriolis frequency f is set to 0. These values and all values of the physical and geometrical parameters below are those of the laboratory experiments.

The numerical setup is displayed in figure 3.2.1. The domain dimensions are $2.56m$ in the horizontal direction and $0.8m$ in the vertical direction. A forcing generating the incident wave (specified below) is applied at the left boundary and a sponge layer of width $0.3m$ is added at the right boundary in order to prevent wave reflection. The bottom boundary condition is of the free-slip type and an implicit free-surface boundary condition is imposed at the top of the domain.

The incident wave is generated at the left boundary in a forcing layer where all variables are restored towards the analytical solution of a plane progressive wave multiplied by the C^∞ envelop function

$$E_z = \frac{1}{2} \left[1 + \tanh \left\{ \frac{3}{2} \tan \left(-\frac{\pi}{2} + \frac{1}{2} \min[2\pi, \max\{0, \pi(n_\lambda + 1) - k_z |z - z_0|\}] \right) \right\} \right] \quad (3.42)$$

This forcing layer is $0.4m$ wide and the restoring intensity varies from 1 at the left boundary to 0 at the end of the layer. The vertical wavelength λ_z in 3.42 and the period of the incident wave are $\lambda_z = 0.125m$ and $T = 42.16s$, respectively, implying that the wavelength λ is equal to $0.1183m$ and the angle of the incident wave is $\theta = 18.9^\circ$. The value of α for which resonance theoretically occurs in this case, referred to as α_{res} , is equal to 7.848° . The horizontal velocity amplitude is set to $U = 3 \times 10^{-4} m s^{-1}$ so that the Froude number of the incident wave is $Fr = 5 \times 10^{-3}$.

The horizontal and vertical resolutions are equal to $5 \times 10^{-3}m$ and $2.5 \cdot 10^{-3}m$ respectively. We have done simulations for horizontal and vertical resolutions $1.25 \cdot 10^{-3}m$ and $0.625 \cdot 10^{-3}m$. However, the results were found to be the same.

3.5.2 RESULTS OF THE NUMERICAL SIMULATIONS

As indicated by the crosses in figure 3.3.1, numerical simulations have been performed for 3 different wave widths ($n_\lambda = 1, 2$ and 4) and 13 slope angles varying from 0° to 12° , including the value α_{res} for which resonance is predicted. These simulations have been run over 40 wave periods.

The off-slope velocity (normal to the slope) $w' = -\partial\psi/\partial x'$, filtered at either the incident wave frequency, denoted w'_1 , or twice this frequency, denoted w'_2 , is displayed for $n_\lambda = 2$ and $n_\lambda = 4$ in figures 3.5.1 and 3.5.2, respectively. The choice of the w' variable is dictated by the forthcoming comparison with the theoretical predictions presented in the previous section. The harmonic filtering has been performed over the last 8 periods of the simulations.

FIRST HARMONIC WAVE

We first consider the incident wave component w'_1 displayed in the left column of figures 3.5.1 and 3.5.2. Before entering the interaction area, the amplitude of this component should be uniform in space by construction. w'_1 however displays some variability, particularly noticeable for $\alpha = 0$ and $n_\lambda = 4$, due to the interaction with weak-amplitude waves reflecting at the right and top boundaries because of the imperfect damping of the sponge layer. The right column of these figures show that second-order harmonics are radiated from the forcing region of the incident wave due to the modulation of this wave by the envelope function 3.42. Focusing on the interaction region, the figures (left column) show that w'_1 does not depend upon z' . Indeed, ignoring viscous effects in this interaction area, the component w'_1 is the amplitude of ψ_1 given by equation 3.30, multiplied by k and, in the present case of a finite-width wave, by the envelope function 3.42.

Figures 3.5.1 and 3.5.2 (left columns) display a major feature, which is not accounted for in the theory. The theory assumes indeed that the off-slope velocity amplitude of the reflected wave is uniform, equal to that of the incident wave to satisfy the impermeability condition at the boundary while this amplitude is actually much weaker than the incident wave amplitude outside the interaction region, all the more so the slope angle is larger.

The latter behaviour has two origins. The main one arises from the focusing of the reflected wave and is due to molecular effects. The wavelength of the reflected wave $\lambda_R = \lambda \sin(\theta - \alpha) / \sin(\theta + \alpha)$ is indeed smaller than the incident wavelength λ so that the viscous (or diffusive) time scale is smaller for the reflected wave as well. When scaled by the wave period, the viscous time scale decays from 16.8 to 0.9 as α increases from 0° to 12° . Dissipation thus becomes an important effect in the dynamics of the reflected wave as α increases. The second effect is due to energy transfer to higher harmonic fields. The right column of figures 3.5.1 and 3.5.2 shows indeed that, as α increases, the amplitude of the second harmonic wave becomes no longer small compared to the amplitude of the incident wave. There is thus a non-negligible energy flux from the first harmonic wave to the second one which also reduces the amplitude of the reflected wave.

SECOND HARMONIC WAVE

We recall that when an incident plane wave of infinite extent reflects on a flat surface ($\alpha = 0$), no harmonics are produced as the superposition of these two waves is a solution of the invis-

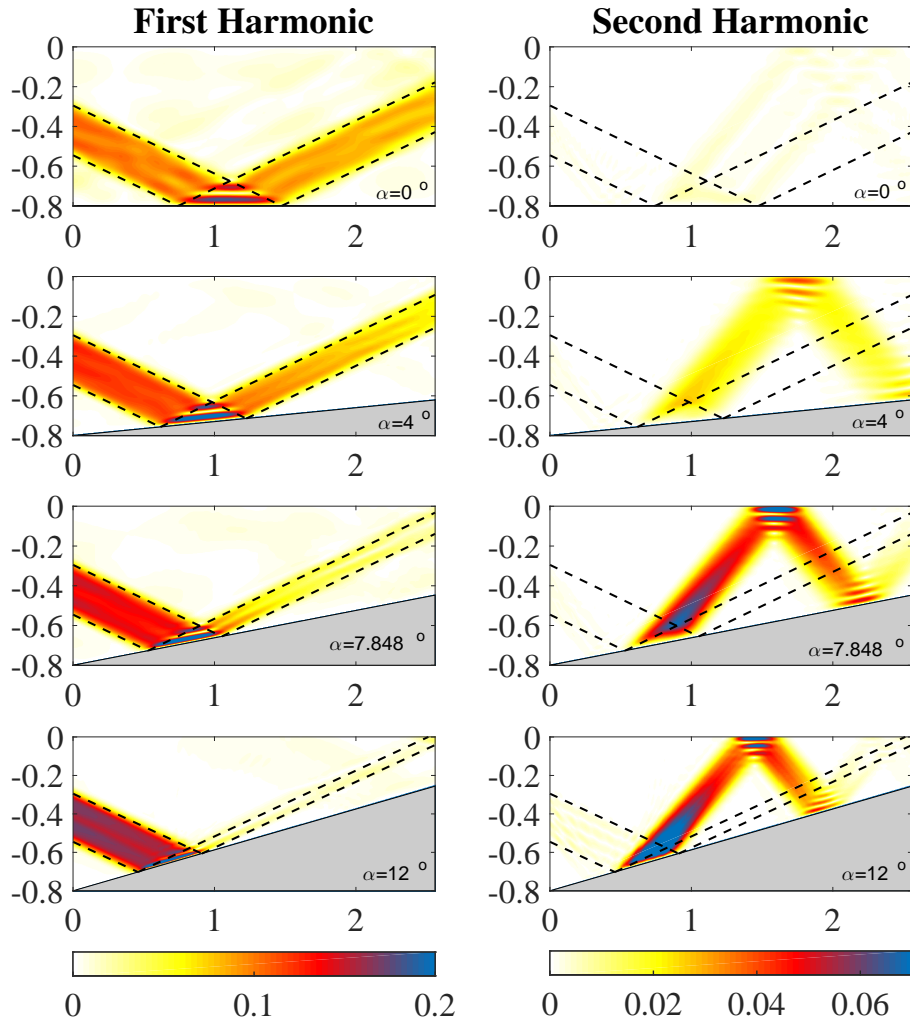


Figure 3.5.1: Amplitude of the off-slope velocity field in $mm\ s^{-1}$ filtered at the first harmonic frequency ω (right column) and at the second harmonic frequency 2ω (left column) for 4 different slope angles α (the angle of incidence θ being constant and set to 18.9°). The incident and reflected waves are delineated with dashed lines. The unit of the horizontal axes is in m . The width of the incident wave is two wavelengths ($n_\lambda = 2$).

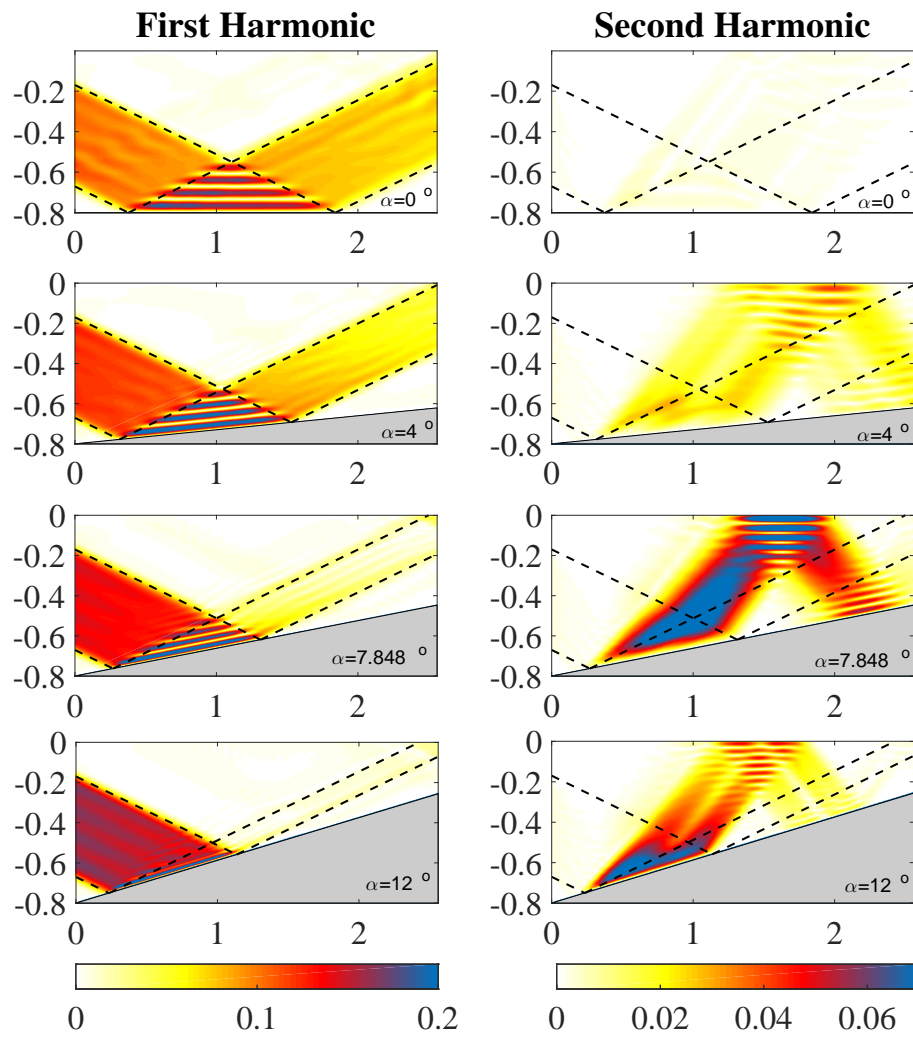


Figure 3.5.2: Amplitude of the off-slope velocity field in $mm\ s^{-1}$ filtered at the first harmonic frequency ω (right column) and at the second harmonic frequency 2ω (left column) for 4 different slope angles α for the incident wave of width four wavelengths ($n_\lambda = 4$).

cid Boussinesq equations (Thorpe, 1968). This is attested by the amplitude of ψ_2^h in equation 3.22, which vanishes for $\alpha = 0$. The situation is different when the plane wave is of finite thickness, as shown more generally by Tabaei et al. (2005) for plane wave beams. Indeed, while each beam is a solution of the inviscid Boussinesq equations, the superposition of the two beams close to the boundary results in their nonlinear interaction and the generation of higher harmonics associated with propagating waves. This is illustrated for instance in the joint numerical and laboratory experiments of Echeverri et al. (2009) and Pairaud et al. (2010). For the present simulations, this accounts for a second harmonic wave propagating from the interaction area in figures 3.5.1 and 3.5.2 for $\alpha = 0$.

When α is non zero, the second-order wave field ψ_2^h is the sum of a forced and a free wave, as discussed in section 3.2.2. The forced wave only exists in the interaction area between the incident and reflected waves and, at resonance, is of largest amplitude at the top of the interaction area. While being also generated inside the interaction area, the free wave can radiate away from this area, its amplitude being then set by that of ψ_2^h at the boundary of the area. In the absence of viscosity, the free wave propagates with this amplitude.

Figures 3.5.1 and 3.5.2 show that, for $\alpha \neq 0$, the second-order free wave is clearly visible outside the interaction area, radiating with the amplitude of the second-order stream function at the boundary of this area. Dissipative effects however damp this amplitude, up to the upper boundary where the free wave reflects. Focusing now on the interaction area, the figures show that the amplitude of the second harmonic off-slope velocity is constant along the slope, as predicted by equation (3.30). This is at least visible for $\alpha = \alpha_{\text{res}}$ and $\alpha = 12^\circ$, and not so clearly for $\alpha = 4^\circ$, consistent with figure 3.3.1 showing that the second-order amplitude is much weaker for $\alpha = 4^\circ$ than for the former cases.

3.5.3 COMPARISON WITH THEORETICAL PREDICTIONS

According to equation 3.22, the amplitude of ψ_2^h should evolve linearly with the normal to the slope z' for $\alpha = \alpha_{\text{res}}$, being otherwise sinusoidal in z' with period $2\pi/\delta k$. Figure 3.5.3 shows the amplitude of the second harmonic off-slope velocity along the normal to the slope direction on a line passing through the top vertex of the interaction region for $n_\lambda = 4$ for two fluid viscosity values, (a) $\nu = 10^{-6} \text{m}^2 \text{s}^{-1}$ and (b) $\nu = 10^{-7} \text{m}^2 \text{s}^{-1}$. The theoretical prediction is shown as a dashed line. We can notice better agreement with the theory as the fluid viscosity is reduced.

The observations from the numerical simulations lead to a striking conclusion when the ratio R^{th} defined by equation 3.37 is compared with its numerical counterpart. Rewriting R^{th} as

$$R^{th} = \frac{Fr}{2} \frac{2k \|\psi_2^h\|}{k \|\psi_1\|} = \frac{1}{2} \frac{Fr \|\partial_{x'} \psi_2^h\|}{\|\partial_{x'} \psi_1\|}, \quad (3.43)$$

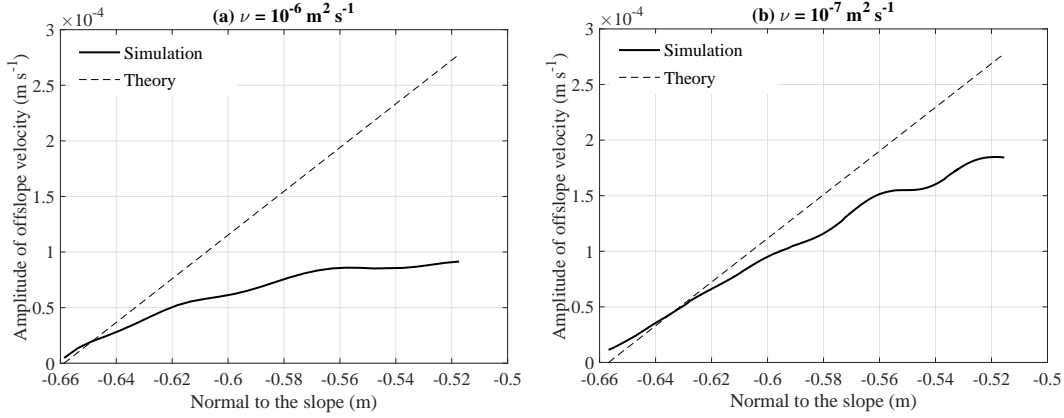


Figure 3.5.3: Amplitude of the second harmonic offslope velocity along the normal to the slope direction on a line passing through the top vertex of the interaction region for for $n_\lambda = 4$ and $\alpha = \alpha_{res} = 7.848^\circ$, for two fluid viscosity values, (a) $\nu = 10^{-6} \text{m}^2 \text{s}^{-1}$ and (b) $\nu = 10^{-7} \text{m}^2 \text{s}^{-1}$. Theoretical prediction given in equation 3.22 is shown as dashed lines.

the numerical counterpart of this ratio can be defined as (in dimensional form)

$$R^{num} = \frac{1}{2} \frac{\|w'_2\|}{\|w'_1\|}. \quad (3.44)$$

In the numerical simulations, the norm of the first and second harmonic off-slope velocities $\|w'_1\|$ and $\|w'_2\|$ are simply defined by the maximum of their respective amplitude over the interaction area.

R^{num} is compared to R^{th} in figure 3.5.4 for $n_\lambda = 1, 2$ and 4. The figure shows that the theory, which involves plane waves, is in very good agreement with the simulations for $n_\lambda = 1$ only, namely for the narrowest finite-width wave we consider, and for α ranging from 0° to about 8° . For higher values of α and n_λ , the two processes mentioned above strongly damp the amplitude of the reflected wave.

More precisely, the largest theoretical amplitude of the first harmonic wave is always reached in the simulations, but in the left part of the interaction area where the reflected wave has not been damped yet. The theoretical maximum is not reached in the numerical simulations for the second harmonic, except when $n_\lambda = 1$. This theoretical maximum is expected at the top of the interaction area but the reflected wave has already weakened there and the second harmonic field is weaker than predicted as well. Only for $n_\lambda = 1$ are the left and top parts of the interaction area close enough and, for α smaller than about 8° , the focusing effect moderate enough for the reflected wave to keep an appreciable amplitude. As a consequence, and quite unexpectedly, numerical simulations only agree with the theoretical predictions for $n_\lambda = 1$, the discrepancy increasing with n_λ .

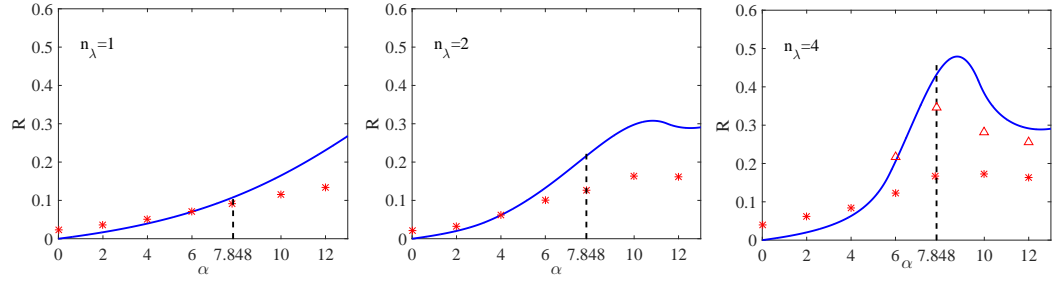


Figure 3.5.4: Comparison of the weakly nonlinear theory presented in section 3.3 with numerical simulations. The Froude number is $Fr = 5 \times 10^{-3}$, the angle of incidence is $\theta = 18.9^\circ$ and an incident wave with 3 different widths is considered: $n_\lambda = 1, 2$ and 4. The points represent R^{num} , defined by equation 3.44, which is the ratio of the second to the first harmonic stream function norms as computed from the numerical simulations. This ratio is compared to the theoretical ratio R^{th} , defined by equation 3.37, and plotted with a solid line. Each star point corresponds to a simulation with fluid viscosity $\nu = 10^{-6} m^2 s^{-1}$, and the triangular points represent simulations fluid viscosity $\nu = 10^{-7} m^2 s^{-1}$. The dashed line indicates the value of α for which resonance is predicted by the theory of Thorpe (1987) (for $\theta = 18.9^\circ$).

3.6 CONCLUSIONS

We studied the nonlinear reflection of a finite-width internal gravity wave incident on a uniform slope, away from critical incidence, in a two-dimensional vertical plane. The angle of incidence is larger than the slope angle, leading to focusing of the reflected wave. Our study has three objectives:

- to revisit the theory of Thorpe (1987) for plane waves of infinite extent, in which the amplitude of the second-order stream function resulting from the interaction of the incident and reflected waves is expressed as an indeterminate form at resonance;
- to apply this theory to a wave of finite width, considered as a simple model of an oceanic internal tide beam;
- to compare the latter theoretical predictions with results of two dimensional numerical simulations of a wave of finite width.

Reformulating Thorpe (1987) theory, we show that the indeterminacy at resonance can actually be waived and that the amplitude of the second-order stream function is a linear function of the distance from the slope. It is therefore unbounded for a plane wave of infinite extent.

An incident wave beam of finite width was considered next. In this case, the generation of the second-order stream function is limited to the area where the incident and reflected waves interact. As a consequence, the second-order amplitude is bounded. However, at resonance, its maximum value scaled by that of the first-order wave can get close to 1 even for small

Froude number values and moderate wavelength numbers. This implies that the reflection problem at resonance is highly nonlinear. We also showed that rotation does not qualitatively change the results obtained in the non rotating case. Numerical simulations of an incident wave of finite width were thus performed in the latter context to estimate the validity of the weakly nonlinear theory.

The numerical simulations surprisingly show that the agreement with the weakly nonlinear theory holds for the narrowest width we considered (one wavelength wide), and for a slope angle smaller than about 8° (the angle of incidence being 18.9°). The reason lies in the amplitude of the reflected wave, which is assumed to be constant in the theory. The amplitude of this wave is actually strongly damped by two effects: molecular effects, because of focusing, and energy transfer to the second-order stream function. Both of these effects are weaker for lower slope angles. Hence the better agreement for slope angles smaller than about 8° .

It follows that, for a finite-width incident wave, (i) the theoretical growth of the second-order stream function is bounded at resonance; (ii) the lower amplitude of the reflected wave should be taken into account in the theory for a closer modelling of the observations.

The analysis presented has been performed in a two-dimensional vertical plane. However the presence of a third dimension modifies the interaction process between the incident and reflected waves, even for normal incidence to the slope. An internal wave beam with finite lateral extent produces a strong horizontally recirculating mean flow as observed by [Bordes et al. \(2012\)](#) in their laboratory experiments, and later theoretically explained by [Kataoka and Akylas \(2015\)](#). Three-dimensional laboratory experiments and numerical simulations of an incident wave of finite width in a plane normal to the slope were conducted in parallel to the present study by [Grisouard et al. \(2013\)](#). In three-dimensional internal wave beam reflection, a Lagrangian mean flow due to nonlinear and dissipative effects can be induced, as opposed to the two-dimensional problem, whose presence should also be introduced in the theory for a complete description of the reflection. Further studies in the reflection of three dimensional internal wave beams are presented in the following chapter.

In summary, the idea is to try to give all of the information to help others to judge the value of your contribution; not just the information that leads to judgement in one particular direction or another.

Richard Feynman, Surely You're Joking, Mr. Feynman!

4

Reflection of three-dimensional internal wave beams

THREE-DIMENSIONAL INTERNAL WAVE BEAMS have been a subject of interest only in the recent times (Bordes et al., 2012, Kataoka and Akylas, 2013, 2015). Much of the research on internal wave beams was restricted to beams of infinite lateral extent. The finite lateral width of the wave beam has started to gain attention only since the development of experimental apparatuses such as the wave generator developed by Gostiaux et al. (2007) (see section 1.4).

Internal tides generated at the ocean topography and over continental shelves propagate as internal wave beams in the ocean (see section 2.4). These beams of internal tides can reflect at the bottom of the ocean, on continental slope or the pycnocline as shown in figure 4.1.1(a). The continental slope descend at more than 4° on average after the shelf-break at the edge of the continental shelf to the beginning of the ocean basins. The reflection of internal tide beams on this continental slope can lead to wave focusing and breaking. The shaping of continental slope has been thought to be influenced by the sediment transport induced by reflecting internal wave beams (Cacchione et al., 2002).

Zhou and Diamessis (2015) has found that two-dimensional internal wave beam reflecting on the pycnocline can induce small particle dispersion at the reflection region. However, when the wave beam is of finite lateral extent (three-dimensional) there can be a strong recirculating mean flow induced by the beam itself as found by Bordes et al. (2012). Indeed, beams of internal tides are of finite lateral extent (compared to their horizontal wavelengths) in the oceans (see figure 4.1.1(b)). The reflection of a three-dimensional internal wave beam and wave induced mean flow was studied by Grisouard (2010) and Grisouard et al. (2013). The extension of their study with more three-dimensional numerical simulations to charac-

terise the induced mean flow is presented in this chapter in the form of draft for an article that is planned to be submitted to Journal of Fluid Mechanics.

4.1 FORCING OF MEAN FLOWS BY THE REFLECTION OF THREE-DIMENSIONAL INTERNAL WAVE BEAMS (ARTICLE)

The results from one of the experiments presented in [Grisouard \(2010\)](#) is used in combination with numerical simulations in order to investigate the strong mean flow forced by a three-dimensional internal wave beam while reflecting on a simple slope.

Forcing of mean flows by the reflection of three-dimensional internal wave beams

Keshav J. Raja¹†, Joel Sommeria¹, Chantal Staquet¹

¹Laboratoire des Écoulements Géophysiques et Industriels, Université Grenoble Alpes, Grenoble, CS 40700, France

(Received xx; revised xx; accepted xx)

The reflection of three-dimensional internal wave beam is analysed. Three-dimensional internal gravity wave beams in a viscous medium have been observed to cause strong horizontal mean flows. This strong mean flow is due to the finite extent of the wave beam and the resulting diffraction. The finite width of the beam in the lateral direction causes the wave to diffract in the horizontal plane. This creates lateral variations of the velocity fields, which in turn leads to a positive source term for the mean vertical vorticity. We investigate this induced mean flow using available experimental data and further three-dimensional numerical simulations. The setup is such that a wave beam of finite extent propagates onto a slope and gets reflected. The recirculating mean flow is independent of the interactions with the slope. The incident and reflected wave interacts close to the slope creating a weaker, spatially periodic mean flow which is dominated by the growing recirculating mean flow. The effects of wave beam width, wave amplitude and the viscosity of the fluid on the forcing of the mean flow are also investigated using numerical simulations. We also performed energy budget of our system in order to quantify the dissipation and transfer of energy from the wave to the mean flow and higher harmonics.

Key words:

1. Introduction

The interest of the oceanic community in internal gravity waves lies primarily in their capacity to vertically mix the ocean, especially in the deep ocean where motions are generally dominated by these waves. Indeed these waves are dissipated at small scales after a complex cascade of nonlinear interactions, and part of the dissipated energy is converted into the potential energy needed for mixing, which brings back cold dense water from the abyss to the surface of the ocean, across constant density surfaces (Munk & Wunsch 1998).

Internal waves also transport momentum, so they can produce a mean horizontal flow by transferring momentum where they are dissipated. This wave streaming effect is thus a major mechanism for driving stratospheric winds by waves emitted in the lower atmosphere (Holton 1982). Wave streaming is also well known in the context of breaking surface waves. It is a major source of currents in near-shore regions (Longuet-Higgins & Stewart 1964). The case of internal waves in the ocean has been much less studied. Grisouard & Bühler (2012) have discussed how the internal waves produced by tidal currents over bottom topography can generate a mean flow by their dissipation far from

† Email address for correspondence: keshav.raja@univ-grenoble-alpes.fr

their generation region. They model the dissipation by an adhoc linear damping of density perturbations, without attempting to describe the actual dissipation processes.

We here consider the different problem of mean flow generation by an internal wave beam impacting a topographic slope. Such wave reflection indeed leads to wave steepening and energy dissipation by breaking, especially strong near the critical slope, obtained when the topographic slope matches the angle of wave propagation. In-situ measurements indeed confirm that such a slope can be an active sink for impinging internal wave energy (Eriksen 1982). The implications of ocean bottom reflection to internal wave spectra and mixing were studied in his eponymous paper by Eriksen (1985). Cacchione & Wunsch (1974) have proposed that the angles in which the energy of semi-diurnal internal tides propagate may determine the average gradient of continental slopes in ocean basins through the sediment transports generated by the bottom shear velocities due to this wave intensification. However the implication in terms of mean flow generation has been much less investigated. This could be a source of ‘sub-meso scale eddies’ whose importance in ocean dynamics is increasingly realised.

The linear internal wave propagation and reflection on a slope in a two-dimensional vertical plane are well known (Phillips 1966). When an internal wave reflects on a slope, its frequency is conserved but its wavelength changes. In the absence of background rotation, the dispersion relation of internal waves states that, $\omega = N \sin \theta$, where ω is the wave frequency, N the buoyancy frequency (assumed to be constant) and θ the angle of propagation of wave energy with the horizontal. Owing to this peculiar dispersion relation, when internal waves propagate toward a sloping bottom with angle α , the reflected wave is either focused (if $\theta > \alpha$, called supercritical reflection) or defocused (if $\theta < \alpha$, called sub-critical reflection). In the supercritical reflection case, the amplitude of the reflected wave increases by a factor, γ where,

$$\gamma = \frac{\sin(\theta + \alpha)}{\sin(\theta - \alpha)} \quad (1.1)$$

A critical condition occurs when $\theta = \alpha$ for which the impinging wave energy gets focused in an infinitely thin reflected wave beam and the amplitude of the reflected wave increases infinitely. Dauxois & Young (1999) have specified how this singularity is smoothed out by nonlinear or transient effects in the limit of small wave amplitude. However in practice the near-critical condition leads to wave breaking and energy dissipation. Numerical studies by Chalamalla *et al.* (2013) indeed show strong turbulence generation during reflection at critical or near critical angles. These computations involved a plane wave beam with infinite lateral extent which does not drive a significant mean flow, as discussed below. Earlier simulations by Slinn & Riley (2001) also performed with a plane wave beam did not lead to mean flow generation, except for thin intrusions from the mixed boundary layers. By contrast, Zikanov & Slinn (2001) have shown that with an oblique incidence of the horizontally projected wave vector, along slope current is generated, in a similar way as along shore currents produced by surface waves with oblique incidence.

Most previous studies with normal incidence focused on the generation of harmonics by the nonlinear interaction between the incident and the reflected wave. These higher harmonics may interact in turn resonantly with primary waves (Thorpe (1987), Thorpe (1997), Leclair *et al.* (2017)). The nonlinear non-resonant wave-wave interactions of internal waves were studied in detail by Teoh *et al.* (1997) with laboratory experiments, and by Javam *et al.* (1999), Javam *et al.* (2000) with numerical simulations. Nonlinear effects in reflecting internal wave beams were studied analytically and numerically by Tabaei *et al.* (2005) using small-amplitude expansions. The existence of these nonlinear effects was later verified by laboratory experiments by Peacock & Tabaei (2005). Labo-

ratory experiments carried out by Gostiaux *et al.* (2006) displayed higher harmonics and also evanescent waves of a frequency higher than buoyancy frequency in the reflection zone. Rodenborn *et al.* (2011) determined the slope angle that generates the maximum amplitude of second harmonic waves during reflection, using laboratory experiments and two-dimensional simulations.

Apart from higher harmonics, wave-wave interactions also generate an Eulerian mean flow which is periodic in the coordinate normal to the slope. The associated Stokes drift and Lagrangian mean flow (which is the sum of Eulerian mean flow and Stokes drift) in internal wave reflection off a free-slip surface were calculated by Zhou & Diamessis (2015), in a two-dimensional domain. This mean flow is however linked to the wave, and it disappears as soon as waves cease. By contrast we are here interested in the mean flow which irreversibly builds up by the dissipation of the impinging wave and persists after the wave ceases.

Most of the above studies deal with a plane internal wave (Thorpe 1987) or two-dimensional internal wave beams in a vertical plane (Tabaei *et al.* 2005). The three-dimensional aspect of internal wave beams, involving the finite extent of the beam in the lateral horizontal direction, has gathered attention only recently. Laboratory experiments and three-dimensional numerical simulations presented by Grisouard *et al.* (2013) show that the mean flow generated in the interaction region when internal wave beam reflects off a slope is markedly different from the one predicted by theory (Thorpe 1987) or by two dimensional simulations. Grisouard *et al.* (2013) reported the presence of a strong, irreversible mean flow of an amplitude exceeding that of the incident wave in the interaction region (Grisouard 2010).

Following these works, the present paper analyses the reflection of a three-dimensional internal wave beam on a slope. The laboratory experiments of Grisouard (2010)) are further analysed in order to study the resonant interactions among the primary (incident and reflected wave beams) and the second harmonic wave beams. Such interactions were predicted by Thorpe (1987) for plane waves. However, for three-dimensional wave beams with finite lateral width, the presence of strong irreversible horizontal mean flow alters the wave field close to the slope. The primary and second harmonic wave beams are found to be refracted in the interaction region due to the strong horizontal mean flow, and reflected wave beam is nearly absent. We here analyse the reflection for different wave amplitudes, lateral widths and fluid viscosities. We also estimate the flux of energy from the wave to the mean flow and to higher harmonics during the reflection through domain integrated energy budget.

The following section briefly summarises the mechanism by which a three-dimensional internal wave beam induces a horizontal mean flow. In section 3, we describe the experimental setup and the numerical model we used. Section 4 presents the experimental and numerical results for a reference case and in section 5, the effects of different wave parameters are analysed using numerical simulations. Finally in section 6, the energy budget is presented with an estimate of the energy fluxes from the primary wave to the mean flow and higher harmonics.

2. Wave induced mean flow

Waves propagating in any medium transport momentum from their source, which drives a mean flow where they are dissipated. This is the general process of wave streaming, well known for sound and surface waves. Considering the Navier-Stokes equations averaged over a wave period, the mean flow acceleration is due to the divergence of the Reynolds stress of the wave velocity field. This so-called radiation stress is a tensor

proportional to the square of the wave amplitude. The divergence of this flux is a vector which corresponds to the net force acting on the mean flow. However this forcing of the mean flow may be opposed by pressure gradients. This is what happens in the case of a wave beam in a vertical plane which is unlimited in the lateral direction. By contrast in a wave beam of finite lateral extent, the divergence of the radiation stress is able to drive a dipolar flow.

The acceleration of the horizontal mean flow \bar{u}, \bar{v} , averaged over a wave period, can be thus expressed as the result of the Reynolds stress $R_{ij} = \widetilde{u_i v_j}$ due to the wave and pressure effects:

$$\frac{\partial \bar{u}}{\partial t} = -\partial_j R_{xj} - \frac{1}{\rho} \partial_x p \quad (2.1)$$

$$\frac{\partial \bar{v}}{\partial t} = -\partial_j R_{jy} - \frac{1}{\rho} \partial_y p \quad (2.2)$$

We here consider just the initiation of the mean flow; so its viscous dissipation is neglected, as well as its feedback on the wave by advection and its own non-linear advection.

These considerations can be made more precise in the case of a wave beam propagating with an angle θ with respect to the horizontal, and a complex amplitude U in velocity, aligned with the beam. Defining the coordinates (X, y, Z) , with X slantwise along the beam, y transverse in the horizontal plane (lateral direction), Z transverse in the vertical plane, we can write the velocity field with a complex amplitude $U(X, y)$ slowly varying in X and y .

$$\widetilde{u_X} = U(X, y) \exp[i(kZ - \omega t)] + c.c. = 2|U(X, y)| \cos(kZ - \omega t + \phi) \quad (2.3)$$

The dominant wave vector \mathbf{k} is perpendicular to the beam, with a corresponding frequency $\omega = N \sin \theta$. The momentum flux tensor (Reynolds stress) has a single non-zero component, aligned with the wave beam, with value $2|U|^2$ after averaging over a wave period. In the absence of energy dissipation, this radiative flux remains uniform along X preventing any spontaneous production of a mean flow. By contrast dissipation leads to a net slanted volume force $-2(d|U|^2/dX)$ whose horizontal projection, is

$$F_x = -2 \frac{d|U|^2}{dX} \cos \theta. \quad (2.4)$$

The rate of decay of the wave beam can be estimated from the rate of energy dissipation in the wave, equal to $(1/2)(\nu + \kappa)k^2 U^2$ per unit of volume. This has to be compared to the energy flux in the beam equal to the group velocity $c_g = (N/k) \cos \theta$ multiplied by the energy density $4|U|^2$ (it includes the kinetic energy and potential energy in equipartition). By equating the divergence of this energy flux $4c_g d|U|^2/dX$ with the local dissipation rate $2(\nu + \kappa)k^2|U|^2/N$, we get

$$\frac{d(|U|^2)}{dX} = -(\nu + \kappa) \frac{k^3 |U|^2}{N \cos \theta} \quad (2.5)$$

which leads to a force with horizontal projection given by

$$F_x = 2(\nu + \kappa) \frac{k^3}{N} |U|^2 \quad (2.6)$$

This force is however partially balanced by an adverse pressure gradient which is needed to drive the return flow occurring outside the wave beam.

A vertical force $F_x \cot \theta$ is similarly produced but it is balanced by a hydrostatic

vertical pressure gradient. A persistent vertical force is indeed prevented by density stratification. More precisely in the absence of diffusion, the Lagrangian vertical transport of fluid elements is prevented by the restoring force due to stratification: an Eulerian vertical mean flow component can exist, if it is balanced by a Stokes drift (the mean Lagrangian velocity associated to the wave), as described by Thorpe (1987). This mean flow is however slaved to the square of the wave amplitude, so it does not grow irreversibly in time once the wave is established, and it disappears when the wave ceases. Furthermore it oscillates as a function of the distance to the wall. A persistent vertical mean flow requires irreversible vertical mixing, associated with diffusivity. This will however remain weak in comparison with the horizontal velocity, so we can consider that the induced mean flow is horizontal and non-divergent at each altitude z . It is then fully determined by its (vertical) vorticity field $\zeta = -\partial_x \bar{u} + \partial_y \bar{v}$.

The growth rate of ζ is given by the curl of the driving force, which eliminates the pressure effect. In the case of a pure wave beam, the vorticity input associated with the force given in equation 2.6 is just $-\partial F_x / \partial y$, leading to

$$\partial \zeta / \partial t = 2(\nu + \kappa) \frac{k^3}{N} |U|^2 \quad (2.7)$$

This fits with equation 2.16 of Fan *et al.* (2018) (the diffusivity κ is equal to zero in this paper and our coordinate y is denoted Z , with a non-dimensional form). This can be also related to a previous analysis by Bordes *et al.* (2012). These authors consider a uniform beam with infinite extent in the vertical coordinate, but finite lateral width. We can then transform $d/dX = \cos\theta \partial/\partial x$, and express the amplitude of the horizontal velocity projection $U' = 2|U|\cos\theta$. The production of vertical vorticity is then obtained by differentiation of 2.4 along y ,

$$\partial \zeta / \partial t = \frac{\partial_{xy}(U'^2)}{2\cos^2\theta} \quad (2.8)$$

This is a similar form as equation (3) of Bordes *et al.* (2012) but larger by a factor of two.

This simple approach however neglects the transverse velocity component which is not a priori justified. Indeed the vorticity production is concentrated at the edge of the wave beam, where lateral gradients of $|U|^2$ are located, but diffraction effects also induce a transverse propagation along y . We can now generalise these results in an integral form, taking first the curl of the general equations 2.2. A good characterisation of the mean flow is the circulation integrated horizontally in the half plane $y > 0$, and vertically within a horizontal slice between $z = z_0$ and z_1 , and along x between x_0 and x_1 , which depends on z for a sloping bottom. This circulation is therefore

$$\Gamma = \int_0^\infty dy \int_{z_0}^{z_1} dz \int_{x_0}^{x_1} \zeta dx \quad (2.9)$$

From 2.2, the growth rate of Γ writes

$$\frac{d\Gamma}{dt} = \int_0^\infty dy \int_{z_0}^{z_1} dz \int_{x_0}^{x_1} (-\partial_y \partial_j R_{xj} + \partial_x \partial_j R_{yj}) \quad (2.10)$$

Integrating the first term first with respect to y , we get the integral $\int_{z_0}^{z_1} dz \int_{x_0}^{x_1} \partial_j R_{xj}|_{y=0} dx$ in the vertical plane at $y = 0$. The integral of $\partial_x R_{xx} + \partial_x R_{xz}$ can be expressed from the boundary flux by the divergence theorem, leading to the contour integral $\int \widetilde{u} \widetilde{\mathbf{u}}_{\mathbf{n}} \cdot \widetilde{\mathbf{n}} dl$. Writing also $\partial_j R_{yj} = \widetilde{\mathbf{u}} \cdot \widetilde{\nabla} \widetilde{v}$, we finally get

$$\frac{d\Gamma}{dt} = \int \overline{\widetilde{u\mathbf{u}_n \cdot \mathbf{n}} dl} + \int_{z_0}^{z_1} dz \int_{x_0}^{x_1} \partial_y \overline{\widetilde{u\widetilde{v}}}|_{y=0} dx + \int_0^\infty dy \int_{z_0}^{z_1} dz [\overline{\widetilde{\mathbf{u} \cdot \nabla \widetilde{v}}}]_{x_0}^{x_1} dx \quad (2.11)$$

In the case of a free wave beam, we can consider a slice with infinite extent in x , so that the last term vanishes. The first term reduces to the difference of the flux $\overline{\widetilde{u\widetilde{v}}}$ through the two planes z_0 and z_1 . This leads to expression 2.8 in an integral form. However we have the additional term $\partial_y \overline{\widetilde{u\widetilde{v}}}$ which may not be equal to zero in the center of a narrow beam (even if $\overline{\widetilde{u\widetilde{v}}} = 0$ by symmetry).

Another characterisation of the mean flow is provided by the vorticity moment

$$\mathcal{P}_x = - \int_{z_0}^{z_1} dz \int \int y \zeta dx dy \quad (2.12)$$

integrated over the whole range of y in a slice between z_0 and z_1 . This is obtained by an integration by part of the usual momentum $\int \int l \overline{u_x} dy$ and differs from it by boundary terms ($\mathcal{P}_x = \int \int \overline{u} dx dy + [\int y \overline{u}]_0^{x_b} dx - [\int (y \overline{v} dx)]_{-\infty}^{+\infty}$). The growth of \mathcal{P}_x can be calculated in a similar way as Γ , using integration by parts in y . This leads to

$$d\mathcal{P}_x/dt = \int_{-\infty}^\infty dy \int \overline{\widetilde{u\mathbf{u}_n \cdot \mathbf{n}} dl} + \int_{-\infty}^\infty dy \int_{z_0}^{z_1} dz [\overline{\widetilde{\mathbf{u} \cdot \nabla \widetilde{v}}}]_{x_0}^{x_1} dx \quad (2.13)$$

In the case of a free wave beam, the last term again vanishes, and the first term reduces to the difference of the flux $\overline{\widetilde{u\widetilde{v}}}$ through the two planes z_0 and z_1 . The term in $\partial_y \overline{\widetilde{u\widetilde{v}}}$ has been suppressed by the integration in the whole y domain.

Let us considering the model of Bordes *et al.* (2012) of a wave beam generated at the vertical wall $x = 0$ uniformly in z , and damping by viscosity at large x . The momentum flux difference through the two limiting horizontal planes is equal to zero, since the beam does not depend on z , and the only contribution comes from the flux through the vertical boundary $x = 0$. The integration of 2.8 from $x = 0$ to ∞ then yields $d\mathcal{P}_x/dt = \int \int \overline{\widetilde{u\widetilde{v}} dy dz}$. This is in agreement with an integration of the local expression 2.7. Therefore it does not agree with the expression of Bordes *et al.* (2012) differing by a factor of two, which points out an inconsistency in this analysis.

Coming now to the results of Fan *et al.* (2018), we need first to relate the viscous effect to the x derivative of the momentum flux. Writing the equation 2.12 of Fan *et al.* (2018) with our notations, we get for a steady wave with no advection by an established mean flow,

$$c_g \frac{\partial U}{\partial X} = -\frac{1}{2}(\nu + \kappa)k^2 U + i \frac{\cos^2 \theta}{2 \sin \theta} \frac{N}{k^2} \frac{\partial^2 U}{\partial y^2} \quad (2.14)$$

We can deduce from this an equation for the energy $|U|^2 = U^* U$ which generalises 2.5 by introducing lateral diffraction effects,

$$c_g \frac{\partial |U|^2}{\partial X} = -(\nu + \kappa)k^2 |U|^2 + i \frac{\cos^2 \theta}{2 \sin \theta} \frac{N}{k^2} [U^* \frac{\partial^2 U}{\partial y^2} - U \frac{\partial^2 U^*}{\partial y^2}] \quad (2.15)$$

so that equation 2.8 is now generalised into

$$\partial \zeta / \partial t = \frac{\partial_{xy}(U_x'^2)}{2 \cos^2 \theta} + i \frac{\cos^2 \theta}{2 \sin \theta} \frac{N}{k^2} [U^* \frac{\partial^2 U}{\partial y^2} - U \frac{\partial^2 U^*}{\partial y^2}] \quad (2.16)$$

The second term in the right hand side however vanishes by integration in the plane $y >$, since $\int_0^\infty U^* \partial_{yy}^2 U = [-U^* \partial_y U + U \partial_y U^*]_{y=0} + \int_0^\infty U \partial_{yy}^2 U^* dy$, and by symmetry $\partial_y U = 0$ at $y = 0$. Similarly we can check that the general relation 2.13 is indeed satisfied.

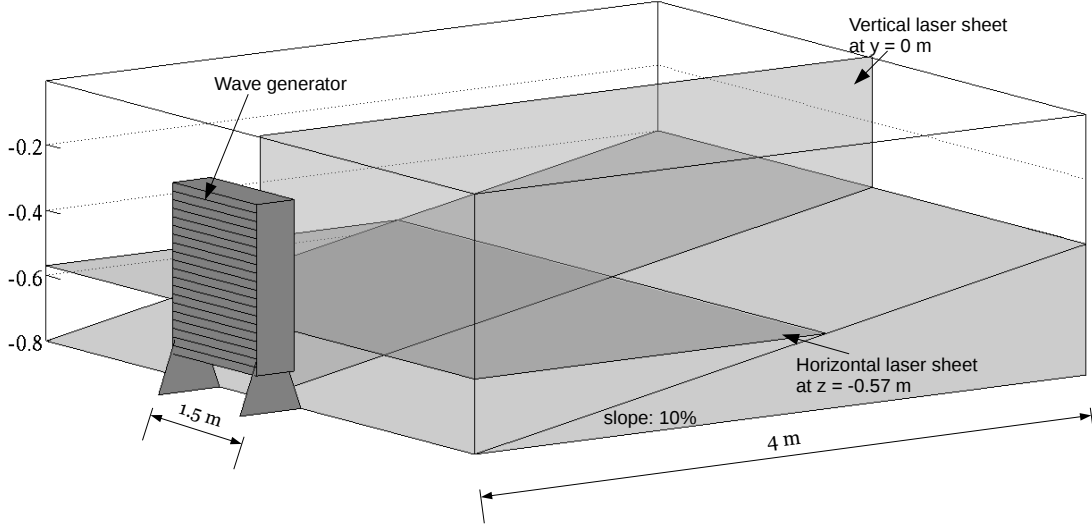


FIGURE 1. Schematic of the experimental setup.

This will be therefore a good guideline to analyse our results of wave reflection beyond any multiscale approximation. In this context the last boundary term in 2.13 must be examined. It vanishes with no-slip boundary conditions on the slope, but this question must be examined with care with the free-slip boundary condition used in the numerical simulations.

3. Experimental and numerical approach

3.1. Experimental setup

Laboratory experiments were carried out on the Coriolis platform at LEGI in Grenoble. It consists of a rotating basin of 13 m in diameter. The large dimensions of the platform allows us to minimise any influence of the lateral walls of the tank while being able to reach large Reynolds numbers. A vertically stratified layer can be created by changing the salinity of the water while filling, using computer controlled volumetric pumps regulating the flow from each of the tanks.

Internal waves are generated using a wave generator designed by Gostiaux *et al.* (2007) (see also Mercier *et al.* (2010)). The tank is filled with uniformly stratified water with a Brunt-Väisälä frequency $N = 0.42 \text{ rad s}^{-1}$, and with a depth of 0.8 m. The wave generator is 1.5 m wide in the y -direction and produces internal wave beams of finite dimensions with wave numbers in x and z directions, according to the forcing frequency and stratification. The wave generator produces a beam of 4 wavelengths with horizontal and vertical wave numbers being, $k_x = 0.17 \text{ cm}^{-1}$ and $k_z = 0.49 \text{ cm}^{-1}$ respectively. The amplitude of the zonal (x -direction) velocity of the generated wave is $U = 2.5 \times 10^{-3} \text{ m s}^{-1}$.

A sloping plate of inclination 10% (slope angle, $\alpha = 5.71^\circ$) is placed in front of the wave generator so that the internal wave beam is incident normally on the slope. The sloping plate is 4 m long and 4.5 m wide. The whole setup of wave generator and the slope (Figure 1) is placed in the centre of the tank.

Measurements are done using Particle Image Velocimetry. The fluid is seeded with neutrally buoyant fine particles (of around $300 \mu\text{m}$ diameter) that trace the flow. Images are captured in a plane illuminated by a laser (laser sheet) using high speed cameras with a fixed frequency in this plane. Successive images are then cross-correlated to obtain

the field of two components of velocity using a Matlab toolbox developed in LEGI called UVMAT. Two separate configurations were used in order to have a horizontal and vertical planes. The vertical plane is through the centre of the wave beam. The choice of the horizontal plane is such that it cuts through the incident and the reflected wave beams in the interaction region close to the slope.

The experiment presented here has a forcing frequency, $\omega = 0.14 \text{ rad s}^{-1}$. So the incident wave propagates at an angle of $\theta = 19.5^\circ$ with the horizontal. The experiment was run for 22 wave periods.

3.2. Numerical method

We are using the model called NHOES (Non-Hydrostatic Ocean model for Earth Simulator) developed by H. Aiki (Aiki & Yamagata 2004). This model solves non-hydrostatic incompressible Boussinesq equations discretised with Arakawa's C-grid. The model introduces a viscous term in the momentum equation with a kinematic viscosity, ν , and a diffusive term in the advection equation with a diffusivity, κ . The governing equations 3.1 are solved using a finite volume method in Cartesian coordinates with uniform grid spacings. A leap-frog scheme is used for time integrations. We used a linear equation of state depending on salinity alone in order to simulate the laboratory experiment.

For the velocity vector \mathbf{u} , pressure p and density ρ with a reference density ρ_0 , the governing equations can be written as follows.

$$\frac{\partial \mathbf{u}}{\partial t} + (\nabla \times \mathbf{u}) \times \mathbf{u} + \frac{1}{2} \nabla \mathbf{u}^2 = -\nabla p - \frac{\rho g}{\rho_0} \mathbf{e}_z + \nu \nabla^2 \mathbf{u} \quad (3.1a)$$

$$\frac{\partial \rho}{\partial t} + \nabla \cdot (\mathbf{u} \rho) = \kappa \nabla^2 \rho \quad (3.1b)$$

$$\nabla \cdot \mathbf{u} = 0 \quad (3.1c)$$

where ν and κ are the kinematic viscosity and diffusivity of the fluid respectively, and g is the acceleration due to gravity.

The numerical domain is of dimensions 2.56 m in x-direction, 7.68 m in y-direction and covers the whole water depth in the experiment (0.8 m) in z-direction with resolutions of $\Delta x = \Delta y = 0.01 \text{ m}$ and $\Delta z = 0.005 \text{ m}$. We have a linear background stratification with a buoyancy frequency, $N = 0.42 \text{ rad s}^{-1}$. The sloping platform with a slope angle of $\alpha = 5.71^\circ$ ($\tan \alpha = 10\%$) is implemented by a partial step scheme. The boundary condition at the slope is of free-slip. The domain is open at the left and right zonal boundaries (x-direction), with a wave forcing at the left and a sponge layer of thickness 0.2 m at the right boundary. The top of the domain is a free surface which is calculated using a semi-implicit scheme.

The density ρ can be written as the sum of a reference density ρ_0 , the background density profile $\hat{\rho}$ and the density perturbation ρ' . Similarly, the pressure p can also be decomposed into the background pressure field \hat{p} and the pressure perturbation p' .

$$\rho = \rho_0 + \hat{\rho}(z) + \rho'(x, y, z, t) \quad (3.2a)$$

$$p = \hat{p}(z) + p'(x, y, z, t) \quad (3.2b)$$

At $t = 0$, the background density $\hat{\rho}(z)$ and pressure $\hat{p}(z)$ are initialised as,

$$\hat{\rho}(z) = \int_z^0 \frac{\rho_0}{g} N^2 dz \quad (3.3a)$$

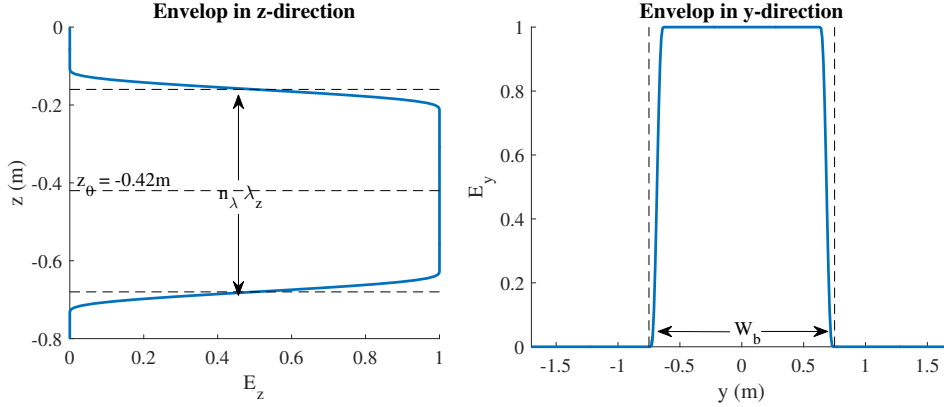


FIGURE 2. The envelopes in y - and z - directions given by equations 3.4b and 3.4c respectively.

$$\hat{p}(z) = \int_z^0 g \left(\frac{\rho_0 + \hat{p}}{\rho_0} \right) dz \quad (3.3b)$$

The forcing at the left boundary generates a plane wave solution in a vertical plane for the zonal velocity, u and density, ρ , which is limited by a smooth envelope in y and z directions, to mimic the finite sized wave generator in the laboratory experiment. The wave forcing on the zonal velocity, u with an amplitude, U , wave frequency, ω , and vertical wave number, k_z , is given as follows.

$$u(0, y, z) = U E_y E_z (1 - e^{-5t \frac{\omega}{2\pi}}) \cos(k_z z - \omega t) \quad (3.4a)$$

$$E_z = \frac{1}{2} \left[1 + \tanh \left\{ \frac{3}{2} \tan \left(-\frac{\pi}{2} + \frac{1}{2} \min[2\pi, \max\{0, \pi(n_\lambda + 1) - k_z |z - z_0|\}] \right) \right\} \right] \quad (3.4b)$$

$$E_y = \frac{1}{2} \left[1 + \tanh \left\{ \frac{3}{2} \tan \left(-\frac{\pi}{2} + \frac{1}{2} \min[2\pi, \max\{0, k_z (W_{\frac{1}{2}b} - |y|)] \right) \right\} \right] \quad (3.4c)$$

The envelop function E_z is centered at z_0 and permits n_λ number of wavelengths in the wave beam. The width of the wave beam in lateral direction is given by $W_b = 2W_{\frac{1}{2}b}$. We have used $n_\lambda = 4$ and $k_z = 48 \text{ m}^{-1}$ for all the simulations, the same as the laboratory experiment. The wave is found to reach a steady regime in less than 6 wave periods, however, the mean flow grows for about 30 wave periods before starting to saturate in the reference case. We ran the simulation for 40 wave periods in all cases.

4. Experimental and numerical results : A reference case

The velocity fields from the experiment and simulation were filtered using a sliding bandpass filter centered at the forcing wave frequency and with a window of three wave periods to obtain the primary wave velocity fields. A similar filter centered at twice the wave frequency was used to get the fields for the second harmonic wave. The Eulerian mean flow fields were obtained using a sliding time average over three wave periods. Figure 3 shows the results from the experiment and simulation. The left and right columns show the results from the laboratory experiment and the numerical simulation respectively.

The first row (figures 3 (a), (b)) shows the zonal velocity field of the primary wave in a vertical plane $y = 0 \text{ m}$, in the centre of the wave beam. We can notice that the reflected wave is nearly absent in both experiment and simulation. The energy of the incident wave is almost completely used up at the slope, through dissipation and transfers to the

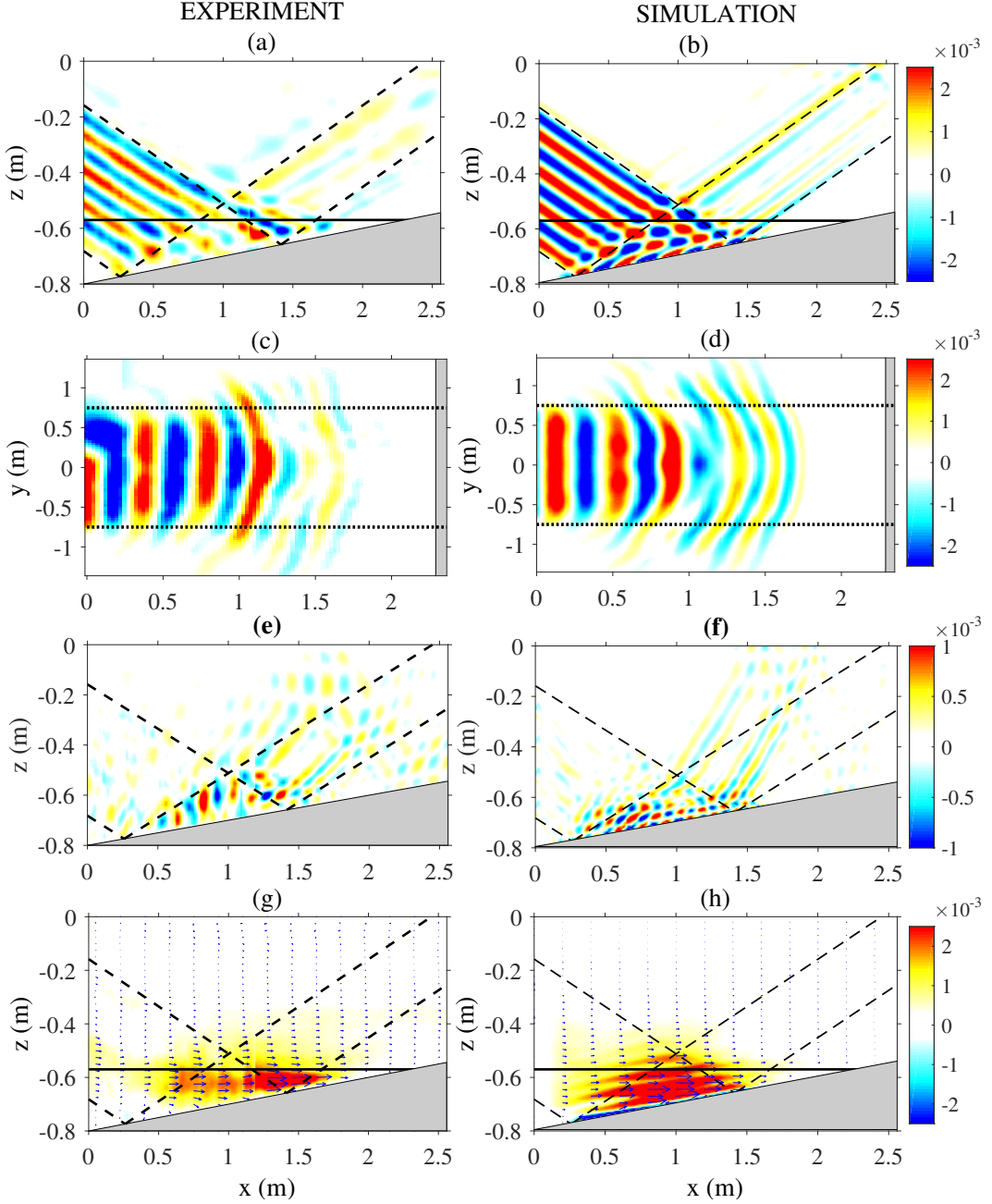


FIGURE 3. Experimental and numerical velocity fields (in $m s^{-1}$) are shown for comparison. The left column shows results from the experiment and the right column shows those from the numerical simulation. Figures (a) and (b) show the wave velocity obtained by filtering out the velocity fields at the forcing frequency over the wave periods 17-20 in the central vertical plane $y = 0m$ (dashed lines represent the wave beams). Figures (c) and (d) show the zonal velocity field of the primary harmonic in a horizontal plane at $z = -0.57m$ (shown with a solid line in figures (a) and (b)). The dotted lines in figures (c) and (d) represent the initial lateral width of the wave beam W_b . The zonal velocity filtered at twice the forcing frequency corresponding to the second harmonic wave is shown in figures (e) and (f). Figures (g) and (h) show the Eulerian mean zonal velocity (in colour) and the Eulerian mean velocity vectors obtained using a time average over the wave periods 17-20 in the central vertical plane $y = 0m$.

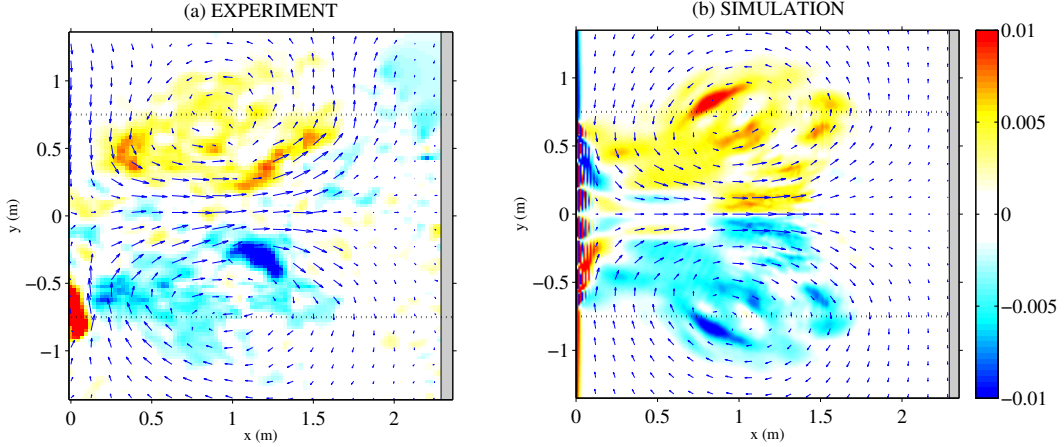


FIGURE 4. Recirculating mean flow, $m s^{-1}$ (arrows) and vertical vorticity, s^{-1} (background colour), in the (a) experiment, (b) simulation. The dashed lines indicate the initial lateral width of the wave beam W_b .

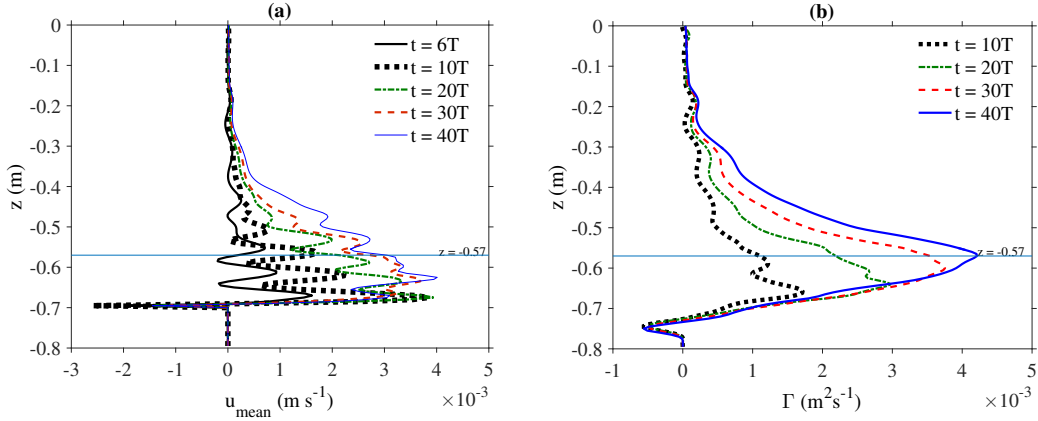


FIGURE 5. From the simulation, (a) the mean horizontal velocity \bar{u} in the interaction region ($x = 1m, y = 0m$) with respect to the height for different time, and (b) the mean circulation approximated as $\Gamma = \int_0^{L_x} \bar{u} dx$ in the plane $y = 0m$, plotted with respect to the height for different time.

mean flow and higher harmonics, with very little left of the incident wave energy to be reflected from the slope.

The second row (figures 3 c, d) shows the top view of the zonal velocity of the primary wave beam in a horizontal plane $z = -0.57 m$. We can see that the wave beam, due to its finite lateral width, diffracts in the horizontal plane as it propagates away from the forcing region. We can notice the spreading of the wave out of its initial lateral width and the bending of the wave crests in the horizontal plane. This bending is exacerbated with the refraction due to the growing mean flow as time progresses.

The zonal velocity of the second harmonic is shown in the third row (figures 3 (e), (f)). The second harmonic wave is seen to be largely confined to the interaction region in both experiment and simulation. This is also a key difference from the two-dimensional reflection where the second harmonic wave was relatively stronger and was propagating away from the slope. The confinement of the second harmonic wave in the present case can be due to the refraction caused by the mean flow close to the slope.

The Eulerian mean flow is shown in the fourth row (figures 3 (g), (h)). The Eulerian

mean flow we find in the experiment and in the simulation is completely different from that of the two-dimensional Eulerian mean flow calculated by Thorpe (1987). We do not find a mean flow that is periodic along the normal to the slope coordinate, but a strong jet-like mean flow in the centre of the beam and close to the slope. Moreover, the amplitude of the mean flow reaches a value comparable to that of the incident wave amplitude.

We can also see that the zonal mean flow for the simulation in figure 3 (h) shows some striations along the slope in the interaction region. These are signatures of the spatially periodic mean flow due to the interaction of the incident and reflected wave beams present in the interaction region, as predicted by Thorpe (1987). Thus, we can observe a superposition of two distinct mean flow structures, namely a spatially periodic mean flow and a strong jet-like mean flow. The former has a constant amplitude (as predicted in Thorpe (1987)) and is reversible (disappears when the forcing is removed). However, the latter grows in time and persists after the forcing. We can see this in figure 5 (a) where the mean flow in the interaction region $((x, y) = (1, 0)m)$ is plotted over the vertical coordinate for different time during the simulation. We can see the spatially periodic mean flow initially before it gets dominated by the growing jet-like mean flow. We can notice in figure 5 (a) that after 40 wave periods, signatures of the periodicity of the initial spatially periodic mean flow remains in the form of striations in the interaction region.

The mean flow forms a strong jet inside the wave beam and has a return flow component outside the beam. This recirculating mean flow is similar to the results of Bordes *et al.* (2012) and Kataoka & Akylas (2015) and is a form of a steady streaming generated by Reynolds stresses in the presence of viscosity. The jet-like mean flow in the centre of the beam and the return flow outside the beam create a dipole mean vorticity field in the horizontal plane. The recirculating mean flow and the dipole mean vertical vorticity field for laboratory experiment and numerical simulation are shown in figure 4. The mean zonal velocity integrated along the zonal coordinate plotted with respect to the vertical coordinate is shown for different time during the simulation in figure 5 (b). The zonal integral of the mean flow at a particular height can be considered as an approximation for the circulation along the edges of one half of the dipole vortex. We can note that the circulation is maximum close to the height corresponding to the horizontal plane $z = -0.57m$ in which we showed the vertical vorticity field in figure 4.

The recirculating mean flow is driven by the divergence of Reynolds stresses of the wave field. The wave beam with a finite width in the lateral direction diffracts in the horizontal plane as it propagates away from the forcing region. This diffraction causes horizontal spatial variations in the Reynolds stress terms, the divergence of which, accelerates the mean flow. Figures 6 (a), (b) show the horizontal velocities of the primary harmonic along the lateral direction in the interaction region (at $x = 1m$) for the experiment and the simulation. The forcing of the wave is along the zonal axis. The wave produced at the forcing region has only zonal and vertical velocity components. The lateral velocity v is forced through Reynolds stresses because of the lateral variations in the zonal velocity u , due to the diffraction of the wave beam.

Wave diffraction is related to an aspect ratio As of the wave beam which is the ratio of the horizontal wavelength λ_x to the lateral width of the wave beam at the forcing region W_b . Diffraction is enhanced if the wave length is comparable to that of the width of the wave beam. Enhanced diffraction causes strong spatial variations of the wave field closer to the wave generator and one can observe the mean flow not far from the wave generator. If As is lower, the wave beam propagates away from the forcing region before the spatial variations become strong enough to force a mean flow. In the case shown

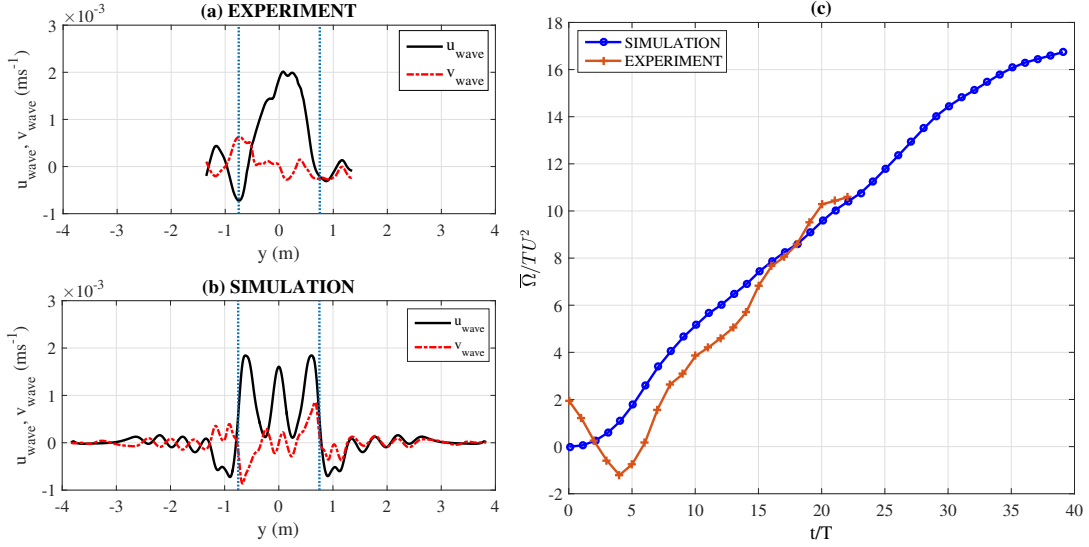


FIGURE 6. The zonal velocities of the primary harmonic, \tilde{u} and \tilde{v} along the lateral (y -) in the interaction region at $x = 1m$ and time = $20T$ for (a) experiment, and (b) simulation. (c) Normalised mean vertical vorticity integrated in the half plane $y > 0$ for the experiment and the simulation.

above, As is 0.25, while for Bordes *et al.* (2012), it ranged from 0.44 to 0.95. In figure 3 (c), (d), we can note that the lateral variations of the wave field start to be significant closer to the slope (from around $x = 1m$), and clearly in figure 3 (g), (h), we find that the mean flow is stronger in the interaction region. Since the forcing of the mean flow is due to the spatial variations in the wave field, this forcing is constant after the wave field has reached a steady regime. Thus, the mean flow continues to grow until it saturates because of viscosity. Figure 6 (c) shows the growth of the normalised mean vertical vorticity integrated in the half plane $y > 0$ for the experiment and the simulation. The initial decrease in the normalised mean vertical vorticity for the experiment in figure 6 (c) is due to pre-existing mean motions in the setup from previous experiments.

5. Effects of wave beam width, wave amplitude and fluid viscosity

As we have mentioned, the Eulerian mean flow induced during the reflection of internal wave beam of finite lateral width includes the spatially periodic mean flow in the interaction region and the recirculating mean flow induced by the beam. The reference case presented in section 4 shows the combined resulting mean flow. The equations presented by Kataoka & Akylas (2015) show that the forcing of the mean flow is governed by the primary wave amplitude, spatial variations of the primary wave amplitude and fluid viscosity. In order to analyse the influence of these parameters, we performed numerical simulations with the same configuration of that of the reference case, but varying the wave beam width, wave amplitude and kinematic viscosity of the fluid. The list of all the numerical simulations we did and their associated non-dimensional parameters is given in table 1.

5.1. Effect of the lateral width of the wave beam

We mentioned in section 4 that the location of the maximum of the Eulerian mean flow depends on the width of the wave beam. We have performed numerical simulations for a narrow beam and a broad beam with their lateral beam widths, half and double

No.	Name	α (deg)	$W_b(m)$	$U(m\ s^{-1})$	$\nu(m^2\ s^{-1})$	As	Fr	Re
1	U0.5	5.71	1.50	0.5×10^{-3}	1.0×10^{-6}	0.247	0.0027	185
2	U0.5- ν 0.1	5.71	1.50	0.5×10^{-3}	0.1×10^{-6}	0.247	0.0027	1850
3	U1- ν 0.1	5.71	1.50	1.0×10^{-3}	0.1×10^{-6}	0.247	0.0064	3700
4	U1- ν 0.5	5.71	1.50	1.0×10^{-3}	0.5×10^{-6}	0.247	0.0064	740
5	U1	5.71	1.50	1.0×10^{-3}	1.0×10^{-6}	0.247	0.0064	370
6	U1- ν 2.0	5.71	1.50	1.0×10^{-3}	2.0×10^{-6}	0.247	0.0064	185
7	U1.5	5.71	1.50	1.5×10^{-3}	1.0×10^{-6}	0.247	0.0097	555
8	U2.5-HalfWb	5.71	0.75	2.5×10^{-3}	1.0×10^{-6}	0.494	0.0161	925
9	Reference	5.71	1.50	2.5×10^{-3}	1.0×10^{-6}	0.247	0.0161	925
10	U2.5-TwiceWb	5.71	3.00	2.5×10^{-3}	1.0×10^{-6}	0.124	0.0161	925

TABLE 1. Table of simulations and their parameters. Listed are the wave frequency ω , the slope angle α , the lateral wave beam width at origin W_b , the wave amplitude at origin U , and the viscosity of the fluid ν . The non-dimensional parameters listed are defined as follows: the horizontal aspect ratio of the wave $As = \frac{\lambda_x}{W_b}$, the Froude number, $Fr = \frac{U}{N\lambda_x}$ and the Reynolds number $Re = \frac{U\lambda_x}{\nu}$.

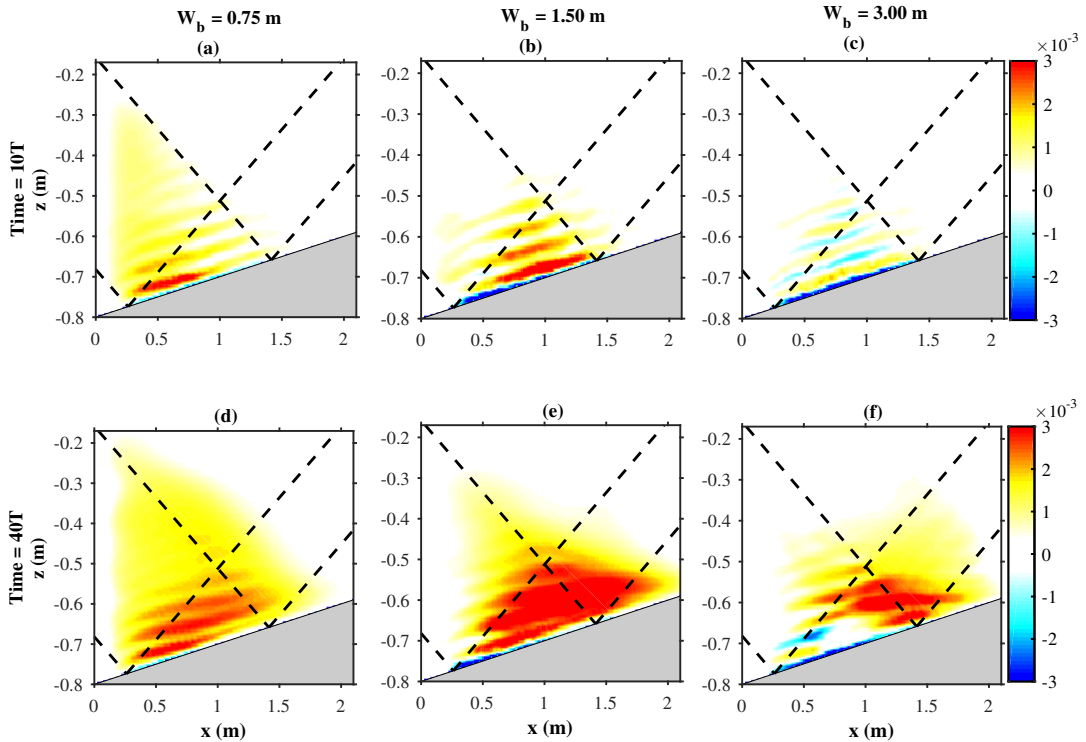


FIGURE 7. The zonal mean velocity \bar{u} for different wave beam widths $W_b = 0.75m$ (left column), $1.50m$ (central column) and $3.00m$ (right column) in the central vertical plane $y = 0m$ at time $10T$ and $40T$.

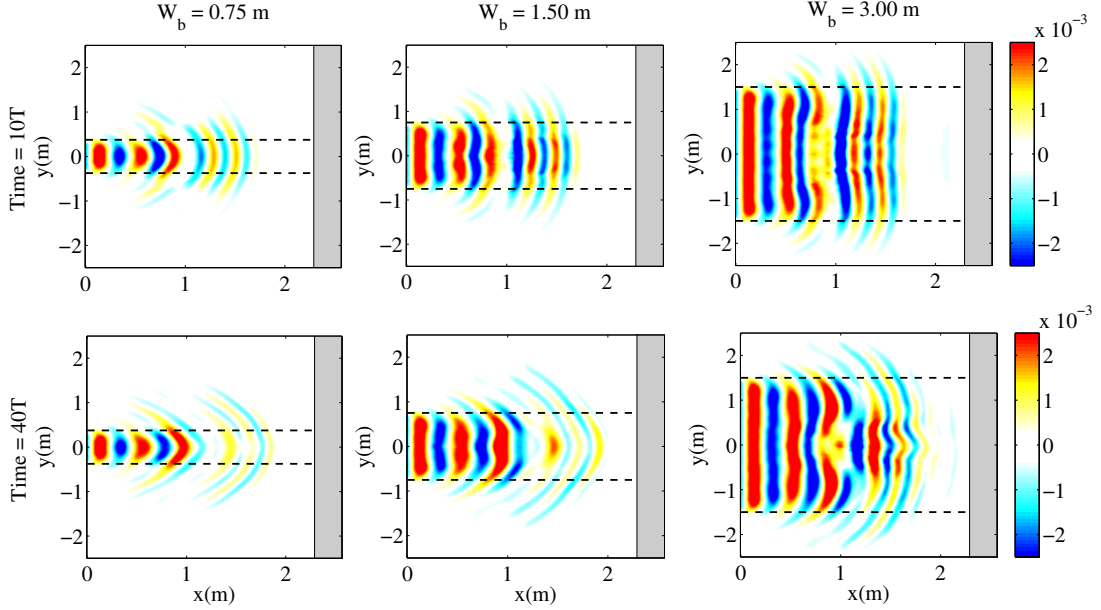


FIGURE 8. The zonal velocity for the primary harmonic for different wave beam widths $W_b = 0.75\text{m}$ (left column), 1.50m (central column) and 3.00m (right column) in the horizontal plane $z = -0.57\text{m}$ at time $10T$ and $40T$.

that of the reference case. The A_s for the narrow beam case (U2.5-HalfWb) is 0.494 close to the value in the experiments of Bordes *et al.* (2012).

In Figure 7, we show the evolution of zonal mean flow for wave beams with three different lateral widths. The narrow beam case (U2.5-HalfWb) is given in the left column, the reference case in the centre and the broad beam case (U2.5-TwiceWb) in the right column. We show the mean flow field in the central vertical plane ($y = 0\text{m}$) at two different instances during the simulations, just after the reflection has been completed and after 40 wave periods. The group velocities and other wave parameters are all same for the three cases.

We can notice that in the narrow beam case in figure 7 (a), there is a mean flow as soon as the reflection is completed, at time $10T$. We can notice that the mean flow is located closer to the wave generator in the region of incident wave beam. The reflected wave that has started to propagate away from the slope has started to interact with the incident wave to form the spatially periodic mean flow in the interaction region. In the reference case shown in figure 7 (b), the recirculating mean flow just started to appear in the interaction region but with notable striations in the normal to the slope direction, resulting from the addition of the periodic mean flow present there. Whereas in the broad beam case in figure 7 (c), the recirculating mean is not yet present, however the periodic mean flow is completely formed, resembling a two-dimensional reflection case.

By the end of our simulations at 40 wave period, the recirculating mean flow has almost fully formed in the broad beam case (figure 7 (f)), compensating the negative parts of the spatially periodic mean flow in the interaction region. For the narrow beam and reference cases, the recirculating mean flow has continued to grow and viscous dissipation has started to balance the acceleration of the mean flow (figure 7 (d) and (e)).

As the mean flow grows, it also refracts the primary wave field, enhancing the bending of the phase lines in zonal direction. The wave diffracts in the horizontal plane and this diffraction creates a laterally bent wave field. This initial bending is later enhanced due to

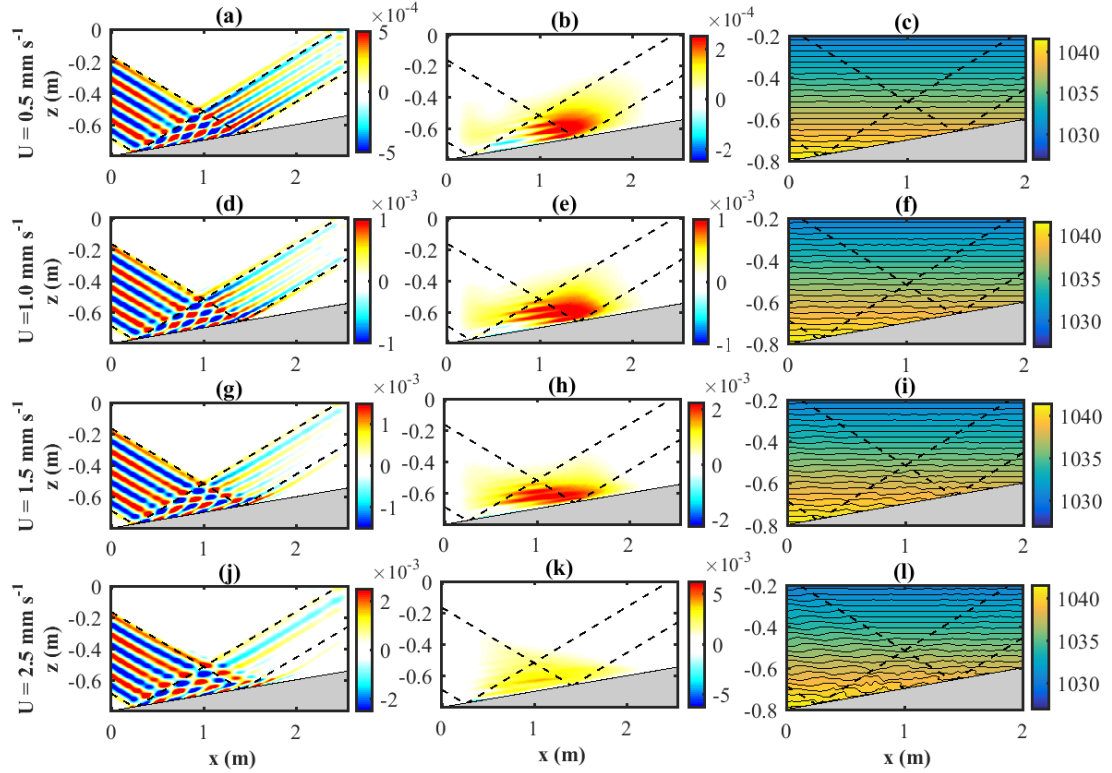


FIGURE 9. The zonal velocity of the primary harmonic (left column), zonal mean velocity (central column) and density field with isopycnals in the central vertical plane $y = 0m$ for different incident wave amplitudes (a), (b) and (c) $U = 0.5 \text{ mm s}^{-1}$, (d), (e) and (f) $U = 1.0 \text{ mm s}^{-1}$, (g), (h) and (i) $U = 1.5 \text{ mm s}^{-1}$, (j), (k) and (l) $U = 2.5 \text{ mm s}^{-1}$.

the refraction caused by the recirculating mean flow. In figure 8, we show the fundamental wave field in the horizontal plane at two points in time, after 10 wave periods and after 40 wave periods. We can see that at 10 wave periods, the wave field for the narrow beam and control cases already show prominent bending of their phase lines. The wider beam experience less diffraction and hence are not bent in the beginning, except at the boundaries of the beam. At the end of 40 wave periods, we can see that the wave field is severely refracted in all cases because of the recirculating mean flow.

5.2. Effect of incident wave amplitude

The mean flow induced by the internal wave beam is forced through the nonlinear term in the mean momentum equation, which is proportional to the square of the wave amplitude. Thus, we expect the amplitude of the mean flow generated by the internal wave beam to be proportional to the square of the wave amplitude.

As we mentioned in the introduction, the amplitude of the reflected wave will be amplified by a factor γ . Moreover, in the interaction region near the slope, the superposition of the incident and the reflected wave further increases the amplitude. This can lead to the overturning of isopycnals near the slope and wave breaking. The amplitude of the wave in our reference case is high enough to have wave breaking close to the slope. In order to study the effect of wave amplitude on the generation of mean flow without any additional effects due to wave breaking, we look at the reflection of waves of lower wave amplitudes. Figure 9 shows the zonal velocity fields of the primary harmonic in the left column, the

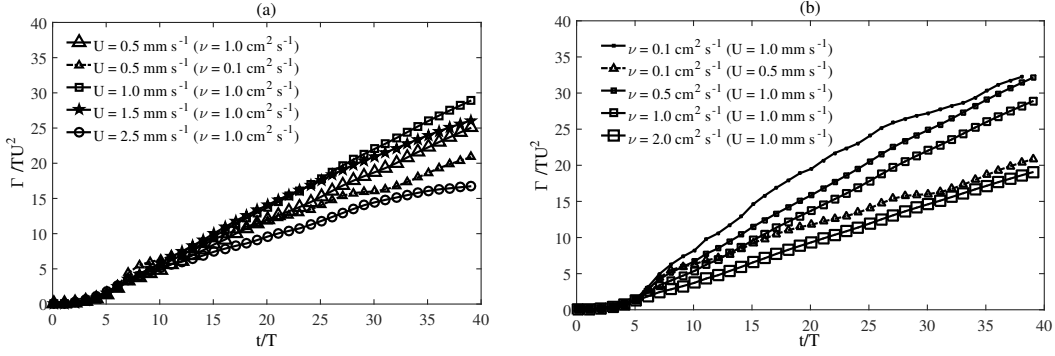


FIGURE 10. Normalised mean vertical vorticity $\bar{\zeta}$ integrated in the horizontal half-plane $y > 0m$ at $z = -0.57m$ for (a) different wave amplitudes for $\nu = 1.0 \times 10^{-6} m^2 s^{-1}$ and (b) different fluid viscosity values for $U = 1 mm s^{-1}$.

zonal mean velocity in the central column and the density field with isopycnals in the right column in the vertical plane, $y = 0$, for different wave amplitudes.

We can notice that for lower amplitude cases, the reflected wave is more prominent. The wave field close to the slope suffers less refraction too in lower amplitude cases. This implies that the near absence of reflected wave in the reference case (shown here in the bottom row of figure 9) is due to the dissipation of incident wave due to wave breaking on the slope. The strong mean flow close to the slope refracts the wave field and steepens it until it breaks.

We can notice that as wave amplitude increases, the vertical displacements of the isopycnals in the interaction region increases and for $U = 2.5 \times 10^{-3} m s^{-1}$ (the amplitude of the reference case presented in section 4) the isopycnals overturn close to the slope. When the isopycnals overturn, the wave breaks and the wave field is disturbed. The source term for the recirculating mean flow comes from the gradients of wave velocity field especially in the interaction region because the resulting amplitude is higher there. When the wave field is disturbed because of breaking, this source term is diminished.

When the wave breaks, the momentum of the wave is transferred to the mean flow. This is a yet another source of a mean flow; the one caused by the breaking of the wave on the slopes. However, we find that the mean flow caused by the breaking is not strong enough to compensate for the lost recirculating mean flow due to breaking. Thus, we see that for the high amplitude reference case, the mean flow is smaller than what we would expect following the trend of the amplitude of the mean flow being proportional to the square of the wave amplitude.

As mentioned earlier, the mean flow due to the interaction of incident and reflected waves is spatially periodic and does not grow in time. We expect only the recirculating mean flow to grow in time. The recirculating mean flow in the horizontal plane due to the finite lateral width of the beam can be quantified by the mean vertical vorticity $\bar{\zeta}$ integrated in the half domain $y > 0$. Figure 10(a) shows the mean vertical vorticity $\bar{\zeta}$ normalised with the square of the wave amplitude U^2 and the time period T of the wave. We observe that for lower amplitudes, the growth of the normalised mean vertical vorticity collapses into a linear profile, which proves that the evolution of the mean vertical vorticity is proportional to the square of the wave amplitude. For the higher amplitude case, we notice a departure from the linear profile, as time progresses. Indeed, in this case, the wave breaks at the slope and the reflected wave is almost absent, thus diminishing the contribution towards the growth of the mean vorticity.

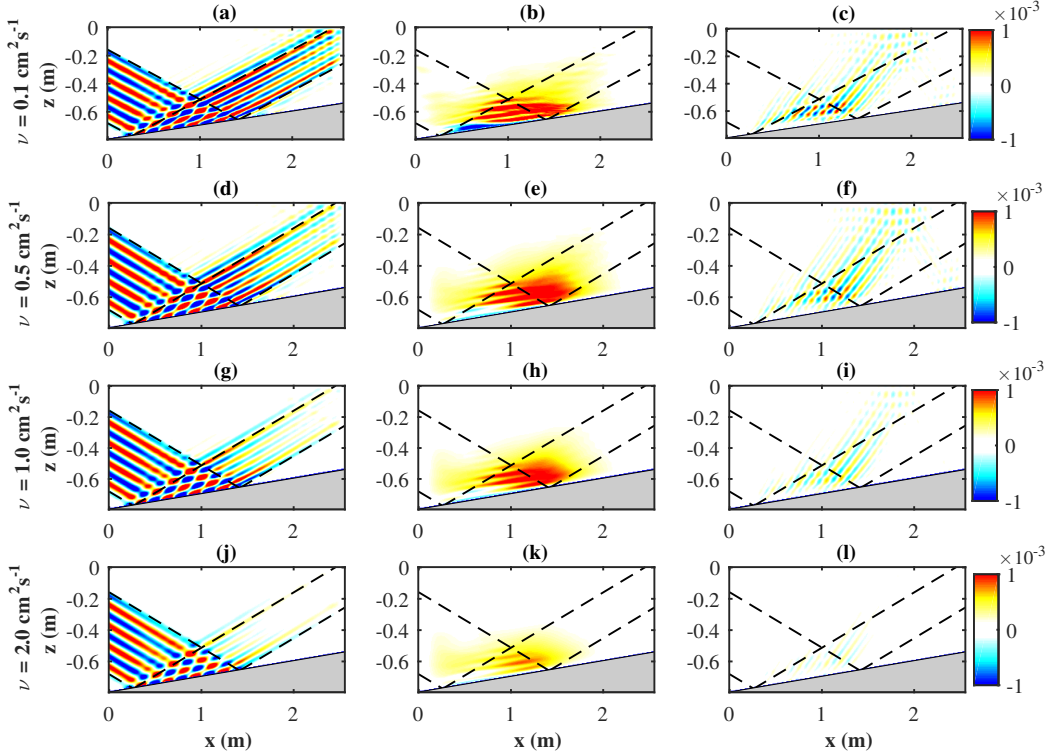


FIGURE 11. The zonal velocity of the primary harmonic (left column), zonal mean velocity (central column) and the zonal velocity of the second harmonic (right column) for fluid viscosity values $\nu = 0.1 \text{ cm}^2 \text{ s}^{-1}$ (a,b,c), $\nu = 0.5 \text{ cm}^2 \text{ s}^{-1}$ (d,e,f), $\nu = 1.0 \text{ cm}^2 \text{ s}^{-1}$ (g,h,i) and $\nu = 2.0 \text{ cm}^2 \text{ s}^{-1}$ (j,k,l) for the wave amplitude $U = 1 \text{ mm s}^{-1}$.

5.3. Effect of fluid viscosity

The viscosity of the fluid is essential to induce irreversible mean flow by waves. However, the viscosity also leads to the attenuation of the wave field that induce the mean flow. Moreover, the induced mean flow also gets affected by the viscosity. In figure 10 (b) we show the growth of the normalised mean vertical vorticity integrated in the half plane $y > 0$ at height $z = -0.57 \text{ m}$, for different values of viscosity. We can note that the growth of the mean vertical vorticity decreases with increasing viscosity for a given wave amplitude. When we decrease the wave amplitude to $U = 0.5 \text{ mm s}^{-1}$ for the fluid viscosity value $\nu = 0.1 \text{ cm}^2 \text{ s}^{-1}$, we can see in figure 10 (a) that the growth of the mean vertical vorticity increases with viscosity.

The equations derived by Kataoka & Akylas (2015) depict the role of viscosity in generating the mean flow. Equation for the evolution of mean flow of Kataoka & Akylas (2015) suggests that for a quasi-steady internal wave beam of finite extent, there will be no mean flow in the absence of viscosity. This can be thought of as a consequence of the non-acceleration theorem. However, the effect of viscosity on the mean flow is not easy to infer from the coupled system of equations of Kataoka & Akylas (2015), because of the wave-mean flow coupling given by the wave equation given in Kataoka & Akylas (2015). The wave field that generates the mean flow is also affected by the viscosity.

In our case, for a fixed wave amplitude ($U = 1 \text{ mm s}^{-1}$), when the value of the kinematic viscosity increases, the attenuation of the amplitude of the wave increases and the growth

of the mean flow decreases. Figure 11 shows the zonal wave velocity (left column), zonal mean flow velocity (central column) and the zonal velocity of the second harmonic (right column) for different fluid viscosities with fixed wave amplitude. We can see that the mean flow and the second harmonics are diminished as fluid viscosity increases for the given wave amplitude.

6. Energy budget

The results from our laboratory experiment and numerical simulations reveal that a strong recirculating mean flow is induced by the finite-width internal wave beam as it reflects on the slope. We argued that the recirculating mean flow is due to the finite-width of the beam and is independent of the spatially periodic mean flow induced on the slope due to the interaction of incoming and reflected waves. In our results, we also see that the energy of the reflected wave is highly diminished. There is hardly any reflected wave visible in our reference case in figures 3 (a), (b). We noted that the internal wave beam in the reference case breaks and dissipated its energy on the slope while also inducing a strong mean flow (see section 5.2 and figures 9 (k) and (l)). Most of the energy of the incoming internal wave beam is either dissipated or transferred to the mean flow and higher harmonics in the reference case. We are evaluating the energy balance of the reference case in our simulation in this section. We are also estimating the power transferred from the wave to the mean flow and the higher harmonics.

6.1. Energy balance of the reference case

The domain \mathcal{V} chosen for calculating the energy budget includes all of our numerical domain except for regions close to the boundaries to avoid the forcing region and sponge layers. Within the numerical domain, the domain \mathcal{V} is [7,230] cm in x-direction, [-358,358] cm in y-direction and from the slope to 150cm in z-direction. Let \mathcal{A} be the surface of the our domain \mathcal{V} with a unit normal \mathbf{n} .

The total energy balance equation in the domain can be written as,

$$\frac{d}{dt} \oint_{\mathcal{V}} e d\mathcal{V} = - \oint_{\mathcal{A}} \mathbf{u}(e + p') \cdot \mathbf{n} dA + \oint_{\mathcal{V}} \left(\nu \mathbf{u} \cdot \nabla^2 \mathbf{u} + \frac{\kappa}{N^2} b \nabla^2 b \right) d\mathcal{V} \quad (6.1)$$

where

$$e = \frac{1}{2} \mathbf{u}^2 + \frac{b^2}{2N^2} \quad , \quad b = -\frac{\rho' g}{\rho_0} \quad (6.2)$$

and ρ' and p' are density and pressure anomalies.

The first term on the right hand side of equation 6.1 is the net flux of energy into the domain and the last term is the dissipation of energy in the domain. So we may rewrite equation 6.1 as,

$$\frac{\partial E}{\partial t} = (\text{Energy influx} - \text{Energy efflux}) + \text{Dissipation} \quad (6.3)$$

Figure 12 (a) shows the terms of equation 6.3 for the reference case. We can notice that the energy in the control volume becomes steady by around 15 wave period and then there is not much changes happening as far as the integral energy balance is concerned. Almost all of the energy that comes into the domain is dissipated within the domain, making the energy going out of the domain very small.

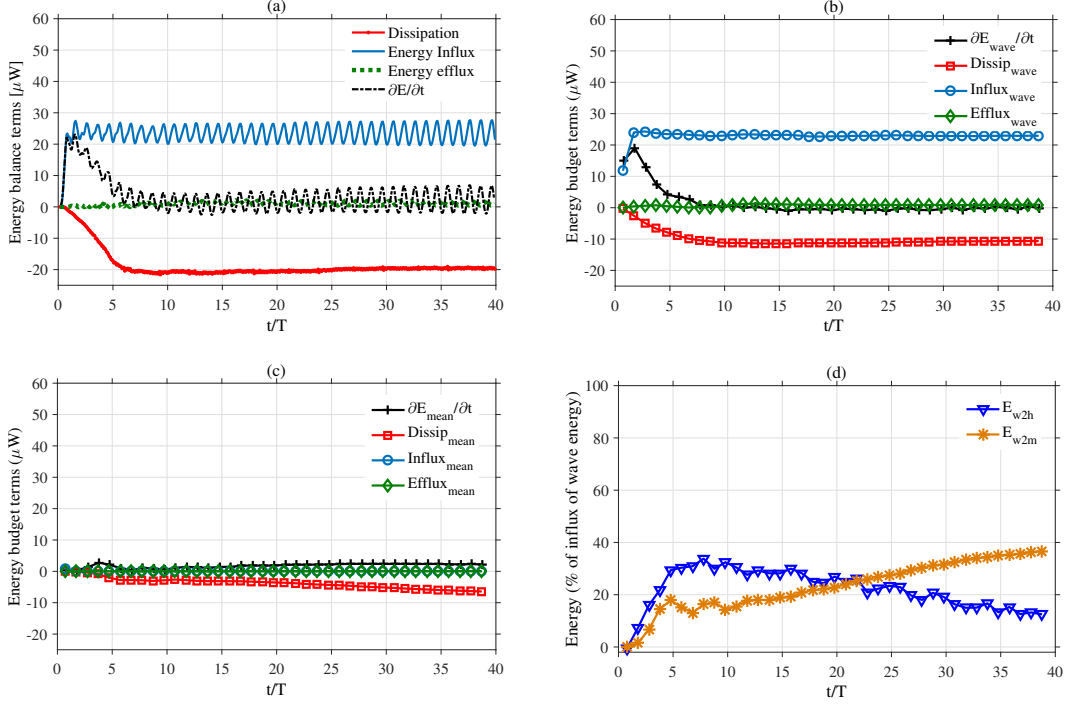


FIGURE 12. (a) Energy balance for the reference case of reflection, (b) energy balance terms for the primary harmonic field, (c) energy balance terms for the mean fields, and (d) rate of energy transfer from the primary harmonic to the mean flow and higher harmonics as percentage of the influx of primary harmonic wave energy.

6.2. Energy balance of wave and mean fields

The energy balance equation can be written for the fundamental wave and mean fields separately. For $\psi = (u, v, w, \rho, p')$, we can write

$$\psi = \tilde{\psi} + \bar{\psi} + O(\epsilon^2) \dots \quad (6.4)$$

where $\tilde{\psi}$ is the fundamental wave field and $\bar{\psi}$ is the mean flow field.

Using the decomposition 6.4 in the energy balance equation 6.1, we can write,

$$\frac{d}{dt} \oint_{\mathcal{V}} \tilde{e} d\mathcal{V} = - \oint_{\mathcal{A}} \tilde{\mathbf{u}}(\tilde{e} + \tilde{p}') \cdot \mathbf{n} dA + \oint_{\mathcal{V}} (\nu \tilde{\mathbf{u}} \cdot \nabla^2 \tilde{\mathbf{u}} + \frac{\kappa}{N^2} \tilde{b} \nabla^2 \tilde{b}) d\mathcal{V} + F(\tilde{\psi} \tilde{\psi}) \quad (6.5a)$$

$$\frac{d}{dt} \oint_{\mathcal{V}} \bar{e} d\mathcal{V} = - \oint_{\mathcal{A}} \bar{\mathbf{u}}(\bar{e} + \bar{p}') \cdot \mathbf{n} dA + \oint_{\mathcal{V}} (\nu \bar{\mathbf{u}} \cdot \nabla^2 \bar{\mathbf{u}} + \frac{\kappa}{N^2} \bar{b} \nabla^2 \bar{b}) d\mathcal{V} + G(\tilde{\psi} \tilde{\psi}) \quad (6.5b)$$

where

$$\tilde{e} = \frac{1}{2} \overline{\tilde{\mathbf{u}} \tilde{\mathbf{u}}} + \frac{\tilde{b} \tilde{b}}{2N^2}, \quad \bar{e} = \frac{1}{2} \overline{\bar{\mathbf{u}} \bar{\mathbf{u}}} + \frac{\bar{b} \bar{b}}{2N^2} \quad (6.6)$$

and F and G are functions containing work by Reynolds stresses. The function G represents the source of mean flow energy. We will assume that the mean flow is induced by only the fundamental wave through the action of Reynolds stresses. The higher harmonics can also induce some mean flow, but the transfer of energy from higher harmonics to the mean flow is negligible compared to that from fundamental wave because of the difference in their amplitudes. So the source of the mean flow energy is the wave energy in the domain. The function F represents the sink of energy from the wave field. This includes the energy transferred from the wave to the mean flow as well as to the

Run	E_i	E_o	E_{w2m}	E_{w2h}	D
U0.5	0.88	0.04 (4.5%)	0.02 (2%)	0.26 (29%)	0.58 (65%)
U0.5- ν 0.1	0.89	0.32 (36%)	0.04 (5%)	0.24 (27%)	0.29 (32%)
U1- ν 0.1	3.75	1.07 (28%)	0.22 (6%)	1.95 (52%)	0.52 (14%)
U1- ν 0.5	3.66	0.46 (12%)	0.25 (7%)	1.43 (38%)	1.57 (43%)
U1	3.57	0.18 (5%)	0.29 (8%)	0.96 (27%)	2.12 (59%)
U1- ν 2.0	3.44	0.08 (2%)	0.22 (6%)	0.76 (22%)	2.45 (70%)
U1.5	8.29	0.47 (6%)	1.43 (17%)	1.82 (22%)	4.47 (54%)
U2.5-HalfWb	10.13	0.54 (5.3%)	2.69 (27%)	1.48 (15%)	5.27 (52%)
Reference	22.93	0.69 (3%)	8.63 (38%)	2.64 (12%)	10.65 (47%)
U2.5-TwiceWb	49.06	2.85 (6%)	14.12 (29%)	8.27 (17%)	23.19 (47%)

TABLE 2. Energy balance terms (μW) for the wave and mean fields at the end of 40 wave periods. E_i , E_o , E_{w2m} , E_{w2h} and D are the wave energy influx, the wave energy efflux, the flux of energy from wave to the mean flow, the flux of energy from wave to higher harmonics and the dissipation of wave energy in the domain, respectively. The percentage values in parentheses are with respect to the wave energy influx, E_i .

higher harmonics. We can estimate the source of the energy for the mean flow from the mean flow energy balance equation and the sink of wave energy from the wave energy balance equation.

We may rewrite the equations 6.5 as

$$\frac{\partial E_{wave}}{\partial t} = (\text{Influx}_{wave} - \text{Efflux}_{wave}) + \text{Dissip}_{wave} + (\text{Sink}) \quad (6.7)$$

$$\frac{\partial E_{mean}}{\partial t} = (\text{Influx}_{mean} - \text{Efflux}_{mean}) + \text{Dissip}_{mean} + (\text{Source}) \quad (6.8)$$

The energy balance terms for the wave and mean fields integrated in the energy budget domain, are shown in figures 12 (b) and (c), respectively. We can identify the sink of energy of the wave field and the source of energy for the mean field. The difference between the sink of wave energy and the source of mean flow energy can be estimated to be the energy transferred to higher harmonics. The transfer of energy from the wave to the mean flow and to the higher harmonics are shown in figure 12 (d) as a percentage of the total wave influx of energy into our domain. We find that after 40 wave periods, about 38% of wave energy entering the domain is transferred to the mean flow, and about 12% of it is transferred to the higher harmonics, with most of the remaining is dissipated within the domain.

6.3. Discussion

The influx of energy of the primary harmonic wave E_i , the efflux of energy of the primary harmonic wave E_o , the power transferred from the primary harmonic wave to the mean flow E_{w2m} , the power transferred from the primary harmonic wave to higher harmonics E_{w2h} and the dissipation rate of the primary harmonic wave energy D, are shown in table 2 for all the simulations at the end of the simulation (40 wave periods). The values in the brackets are the values as percentage of the primary wave energy influx.

We can notice that the energy flux into the mean flow (E_{w2m}) increases with the

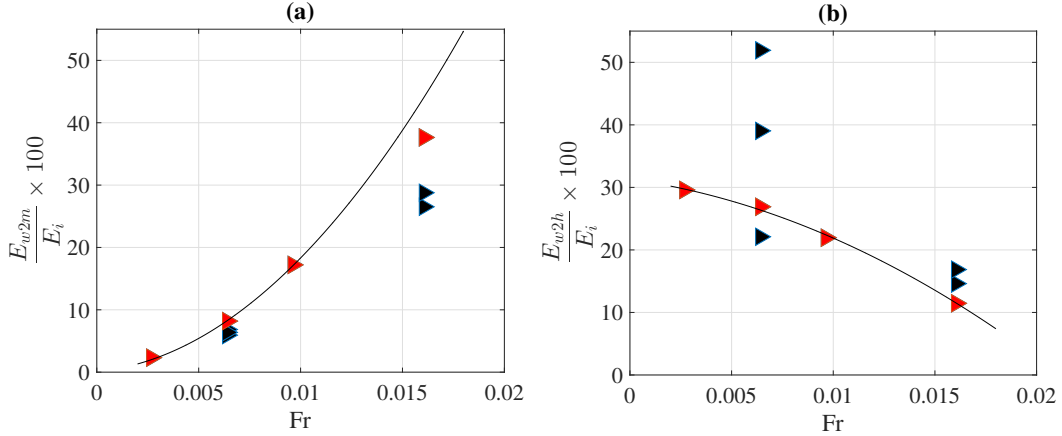


FIGURE 13. Normalised energy flux to (a) the mean flow and (b) the higher harmonics, plotted as a function of the Froude number. The cases with the same kinematic viscosity ($\nu = 1.0 \times 10^{-6} \text{m}^2 \text{s}^{-1}$) and wave beam width ($W_b = 1.5\text{m}$) are shown in red colour.

incident wave amplitude. As we have mentioned before, the amplitude of the mean flow is proportional to the square of the wave amplitude since mean flow is forced by the divergence of Reynolds stress. The energy of the mean flow is, therefore, proportional to the fourth power of the wave amplitude. Thus, the energy flux into the mean flow as percentage of the influx of wave energy increases as the square of the wave amplitude. We can notice this trend in the table 2 in the cases U0.5, U1, U1.5 and Reference. The energy flux into the mean flow (E_{w2m}) normalised with the influx of wave energy (E_i) is shown with respect to the Froude number in figure 13(a).

We also can see that the efflux of primary harmonic wave energy E_o (associated with the reflected wave) remains almost the same (varies between 3% and 6%) with the increase in the incident wave amplitude. In the reference case, we have seen that the wave breaks at the slope and there is hardly any reflected wave. In cases of lower incident wave amplitude, the reflected wave is mostly dissipated as it propagates away from the slope. The reflected wave suffers more dissipation because the wave is focused after reflection. The difference for lower amplitude cases, however, is that in the absence of wave breaking, the interaction between incident and reflected wave gives rise to prominent second harmonics. We can notice in the table 2 that the power transferred to the higher harmonics as percentage of the influx of wave energy decreases with the increasing amplitude with a sudden drop for the largest amplitude in the Reference case (when the wave breaks). The energy flux into the higher harmonics (E_{w2h}) normalised with the influx of wave energy (E_i) is shown with respect to the Froude number in figure 13(b).

For the simulations with different values of kinematic viscosity, namely, U1- ν 0.1, U1- ν 0.5, U1 and U1- ν 2.0, we can see that the the outgoing flux of primary harmonic wave energy decreases with increasing viscosity. Indeed, the reflected wave is dissipated more when the viscosity increases. We can also note that the dissipation rate of the wave energy in the domain increases with the increase in the viscosity. However, the surprising thing is that the energy flux to the mean flow remains almost the same (varies between 6% and 8%) with the change in viscosity. This implies that the power transferred to the mean flow depends only on the Froude number and is independent of the kinematic viscosity. The power transferred to the higher harmonics can be seen to be decreasing with increasing viscosity. This can be because of the dissipation of the primary wave in the interaction region leading to reduced transfer to the higher harmonics.

7. Conclusions

We have studied the reflection of a three-dimensional internal wave beam on a slope using laboratory experiment and numerical simulations. The reflection of an internal wave beam with a finite lateral width is fundamentally different from that of an infinite plane wave or two-dimensional wave beam because of the presence of a strong jet-like Eulerian mean flow induced by the wave beam. The wave induced mean flow diminishes the generation of second harmonic wave close to the slope thereby making it difficult for resonant interactions as predicted by Thorpe (1987).

The Eulerian mean flow observed in the laboratory experiment and numerical simulation has two distinct mean flow structures namely, a spatially periodic mean flow produced by the nonlinear interaction of incident and reflected waves near the slope and a jet-like mean flow induced by the wave-wave interaction of the finite-width wave beam. The spatially periodic mean flow is confined to the interaction region close to the slope and its amplitude is constant in time. However, the jet-like mean flow grows in time with a return flow component outside the wave beam, forming a pair of vortices in the horizontal plane. The growing jet-like mean flow dominates the spatially periodic mean flow as time passes with the periodicity of the latter forming distinct striations in the mean flow in the interaction region. The generation of a similar jet-like mean flow through wave-wave interactions was observed for a propagating internal wave beam with finite lateral width by Bordes *et al.* (2012). Kataoka & Akylas (2015) derived a coupled system of equations explaining the evolution of the mean flow induced by a finite-width internal wave beam.

The jet-like mean flow is forced by the divergence of Reynolds stress of the wave field. So the forcing of the mean flow is proportional to the square of the wave amplitude. The forcing of the mean flow also depends on the spatial variations of the wave field. This is also evident from the coupled system of equations of Kataoka & Akylas (2015). They find that the lateral spatial variations of the wave field is essential for the growth of the jet-like mean flow. The wave beam with finite lateral width diffracts in the horizontal plane resulting in the bending and spreading of the wave crests creating lateral variations in the wave beam. Apart from the spatial variations, viscosity is also essential for forcing the mean flow. However, viscosity also diffuses the wave field decreasing the forcing of the mean flow. In order to test these, we have performed numerical simulations varying the lateral width of the wave beam, amplitude of the wave and the kinematic viscosity of the fluid.

When the lateral width of the wave beam is decreased, we observed that the jet-like mean flow appeared sooner, closer to the wave generator and was observed to grow faster. The diffraction of the wave beam in the horizontal plane depends on the aspect ratio $As = \lambda_x/W_b$. When the width is decreased (As increases), the diffraction is more efficient, increasing the forcing of the mean flow. Thus, the mean flow grows faster and reaches saturation sooner than for reference case. When the width of the beam was increased, the growth of the mean flow was slower.

Increasing the incident wave amplitude increases the amplitude of the induced mean flow quadratically. For the highest wave amplitude we studied, the wave breaks at the slope and the generation of mean flow is less efficient. This is because the wave breaking perturbs the wave field diminishing the streaming of jet-like mean flow.

The generation of irreversible mean flow requires fluid viscosity. However, we find that increasing the fluid viscosity decreases the growth rate of the mean flow for a given wave amplitude. Indeed, fluid viscosity acts on the wave field as well and attenuation of the wave amplitude results in the decrease of the induced mean flow amplitude. However,

when we decrease the wave amplitude, we notice that mean flow amplitude decreases with decreasing fluid viscosity.

The energy flux into the mean flow and the second harmonic wave was estimated from the energy balance equation for the primary wave field (the sink term in the energy balance equation). The energy balance equation for the mean field gave an estimate of the energy flux into the mean flow from the primary wave. The difference between the sink of energy flux of the primary wave and the source of the mean flow was assumed to be the energy flux into the second harmonic wave field. The following results were observed from this analysis –

- The energy flux into the mean flow E_{w2m} normalised with the wave energy influx E_i increases quadratically with the increase in Froude number. The energy flux into the mean flow is proportional to the square of the mean flow amplitude and the influx of wave energy is proportional to the square of the wave amplitude. Therefore, the energy flux into the mean flow is proportional to the fourth power of the wave amplitude. As mentioned above, in the highest amplitude case that we studied (reference case), we find a departure from this trend because of wave breaking.

- The normalised energy flux into the second harmonic wave (E_{w2h}/E_i) decreases with increase in the Froude number. This is in contrast with the predictions of weakly-nonlinear theory. Indeed, all the wave amplitudes we studied are in the strongly nonlinear regime.

- For different wave beam widths, the normalised energy flux into mean flow was found to be higher for the reference case than both narrow (U2.5-HalfWb) and broad (U2.5-TwiceWb) beam cases. This points towards a possible optimum aspect ratio for maximum transfer of energy to the mean flow.

- The fluid viscosity does not seem to have any effect on the energy flux into the mean flow. Indeed, the dissipation of the wave field decreases with the decrease of fluid viscosity. However, this decrease in wave attenuation is reflected on a stronger reflected wave and enhanced second harmonic wave; the enhancement of energy flux into second harmonic wave being the result of a stronger reflected wave.

We have only analysed three of the parameters involved in the reflection of three-dimensional internal wave beam, namely the wave amplitude, width of the beam and fluid viscosity. The influence of parameters such as the slope angle, wave frequency or stratification and no-slip boundary condition at the slope need to be studied in future. The equations derived by Kataoka & Akylas (2015) should be re-written to shed more light into the influence of some of these parameters in inducing a recirculating mean flow by a finite-width internal wave beam. Attempts are underway by some of the authors to find a simpler steady-state solution of the mean flow induced by a three-dimensional internal wave beam of finite lateral width.

Another important effect that can influence the mean flow generated by the internal wave beam is background rotation. Three-dimensional numerical simulations similar to those presented in this paper are used to investigate the reflection of finite-width inertia-gravity wave beams under different Rossby number. The authors are in preparation of an article on that topic.

The laboratory experiment presented here was performed by Louis Gostiaux and Nicolas Grisouard in the Coriolis platform at LEGI, Grenoble with the help of Samuel Viboud during Nicolas's PhD preparation with Chantal Staquet. The three-dimensional numerical simulations were started by Matthieu Leclair. We thank them all for their insights and contributions to this project. We also thank Hidenori Aiki for all his help in running the NHOES code he developed.

REFERENCES

- AIKI, H. & YAMAGATA, T. 2004 A numerical study on the successive formation of meddy like lenses. *J. Geophys. Res.* **109**, (C6).
- BORDES, G., VENAILLE, A., JOUBAUD, S., ODIER, P. & DAUXOIS, T. 2012 Experimental observation of a strong mean flow induced by internal gravity waves. *Physics of Fluids* **24**, 086602.
- CACCHIONE, D. & WUNSCH, C. 1974 Experimental study of internal waves over a slope. *J. Fluid Mech.* **66**, 223–239.
- CHALAMALLA, V. K., GAYEN, B., SCOTTI, A. & SARKAR, S. 2013 Turbulence during the reflection of internal gravity waves at critical and near-critical slopes. *J. Fluid Mech.* **729**, 47–68.
- DAUXOIS, T. & YOUNG, W. R. 1999 Near-critical reflection of internal waves. *J. Fluid Mech.* **390**, 271–295.
- ERIKSEN, C. C. 1982 Observation of internal waves reflection off sloping bottom. *J. Geophysical Research* **87**, 525–538.
- ERIKSEN, C. C. 1985 Implications of ocean bottom reflection for internal wave spectra and mixing. *J. Physical Oceanography* **15**, 1145–1156.
- FAN, BOYU, KATAOKA, T & AKYLAS, TR 2018 On the interaction of an internal wavepacket with its induced mean flow and the role of streaming. *Journal of Fluid Mechanics* **838**.
- GOSTIAUX, L., DAUXOIS, T., DIDELLE, H., SOMMERIA, J. & VIBOUD, S. 2006 Quantitative laboratory observations of internal wave reflections on ascending slopes. *Physics of Fluids* **18**, 056602.
- GOSTIAUX, L., DIDELLE, H., MERCIER, S. & DAUXOIS, T. 2007 A novel internal waves generator. *Experiments in Fluids* **42**, 123–130.
- GRISOARD, N 2010 Réflexions et réfractions non linéaires dondes internes de gravité. PhD thesis, PhD thesis (in French), University of Grenoble, France.
- GRISOARD, NICOLAS & BÜHLER, OLIVER 2012 Forcing of oceanic mean flows by dissipating internal tides. *Journal of Fluid Mechanics* **708**, 250–278.
- GRISOARD, N., LECLAIR, M., GOSTIAUX, L. & STAQUET, C. 2013 Large scale energy transfer from an internal gravity wave reflecting on a simple slope. *IUTAM Symposium Procedia* **8**, 119–128.
- HOLTON, JAMES R 1982 The role of gravity wave induced drag and diffusion in the momentum budget of the mesosphere. *Journal of the Atmospheric Sciences* **39** (4), 791–799.
- JAVAM, A., IMBERGER, J. & ARMPFIELD, S. W. 1999 Numerical study of internal wave reflection from sloping boundaries. *J. Fluid Mech.* **396**, 183–201.
- JAVAM, A., IMBERGER, J. & ARMPFIELD, S. W. 2000 Numerical study of internal wave interactions in a stratified fluid. *J. Fluid Mech.* **415**, 65–87.
- KATAOKA, T. & AKYLAS, T. 2015 On three-dimensional internal gravity wave beams and induced large-scale mean flows. *J. Fluid Mech.* **769**, 621–634.
- LECLAIR, M., RAJA, K. J. & STAQUET, C. 2017 Nonlinear reflection of a two-dimensional finite-width internal gravity wave onto a slope. *J. Fluid Mech.* p. in preparation.
- LONGUET-HIGGINS, MICHAEL S & STEWART, RW 1964 Radiation stresses in water waves; a physical discussion, with applications. In *Deep Sea Research and Oceanographic Abstracts*, vol. 11, pp. 529–562. Elsevier.
- MERCIER, M. J., MARTINAND, D., MATHUR, M., GOSTIAUX, L., PEACOCK, T. & DAUXOIS, T. 2010 New wave generation. *J. Fluid Mech.* **657**, 308–334.
- MUNK, WALTER & WUNSCH, CARL 1998 Abyssal recipes ii: Energetics of tidal and wind mixing. *Deep Sea Research Part I: Oceanographic Research Papers* **45** (12), 1977–2010.
- PEACOCK, T. & TABAEI, A. 2005 Visualization of nonlinear effects in reflecting internal wave beams. *Physics of Fluids* **17**, 061702.
- PHILLIPS, O. M. 1966 Dynamics of the upper ocean. Cambridge University Press.
- RODENBORN, B., KIEFER, D., ZHANG, H. P. & SWINNEY, H. L. 2011 Harmonic generation by reflecting internal waves. *Physics of Fluids* **23**, 026601.
- SLINN, DONALD N & RILEY, JJ 2001 Internal wave reflection from sloping boundaries. *Submitted to J. Fluid Mech.*

- TABAEI, A., AKYLAS, T. R. & LAMB, K. G. 2005 Nonlinear effects in reflecting and colliding internal wave beams. *J. Fluid Mech.* **526**, 217–243.
- TEOH, S. G., IVEY, G. N. & IMBERGER, J. 1997 Laboratory study of the interaction between two internal wave rays. *J. Fluid Mech.* **336**, 91–122.
- THORPE, S. A. 1987 On the reflection of a train of finite-amplitude internal waves from a uniform slope. *J. Fluid Mech.* **178**, 279–302.
- THORPE, S. A. 1997 On the interactions of internal waves reflecting from slopes. *J. Fluid Mech.* **27**, 2072.
- ZHOU, Q. & DIAMESSIS, P. 2015 Lagrangian flows within reflecting internal waves at a horizontal free-slip surface. *Physics of Fluids* **27**, 126601.
- ZIKANOV, OLEG & SLINN, DONALD N 2001 Along-slope current generation by obliquely incident internal waves. *Journal of Fluid Mechanics* **445**, 235–261.

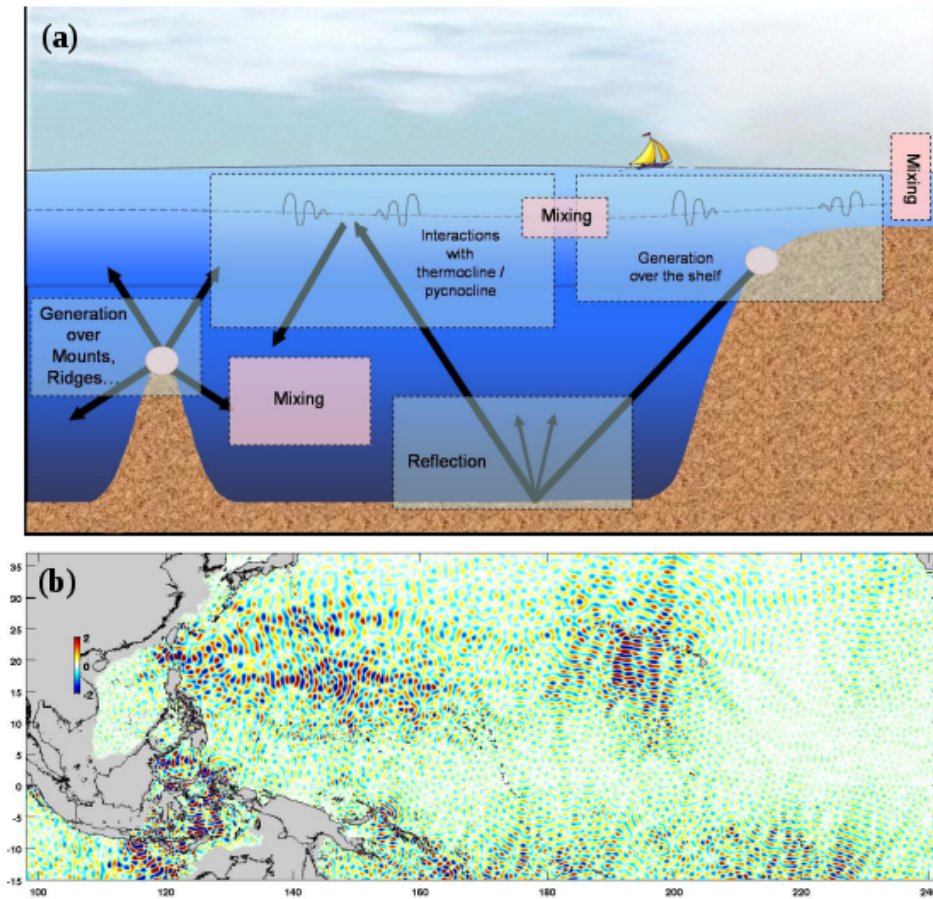


Figure 4.1.1: (a) Schematic representation of the internal tide generation, propagation, reflection and dissipation. Internal tidal beam can be seen reflecting on the continental slope and the pycnocline. Image from Francis Auclair. (b) Global M2 1st mode internal tide map (in-phase, cm). Notice that internal tide beams have finite lateral extent and therefore are three-dimensional wave beams. Image from Egbert and Erofeeva (2014).

I was born not knowing and have had only a little time to change that here and there.

Richard Feynman, Letter to Armando Garcia J,
December 11, 1985

5

Three-dimensional inertia-gravity wave beams

THE EFFECTS OF ROTATION on streaming of a mean flow by three-dimensional internal wave beams with finite lateral width are investigated in this chapter. With the Coriolis force providing a restoring force in addition to gravity, internal waves propagate as inertia-gravity waves with a dispersion relation is given in equation 2.25.

Internal waves with frequencies close to the Coriolis frequency (near-inertial) are a ubiquitous phenomenon in the ocean, and the inertial peak usually dominates the oceanic internal-wave spectrum. As we mentioned in chapter 1, near-inertial waves in oceans are mostly generated by atmospheric disturbances through wind stress on the upper layers of the ocean. Alford (2003a) has constructed a global map of the input of near-inertial energy shown in figure 1.2.1(b). However, laboratory or numerical studies of inertia-gravity waves are not numerous to the best of our knowledge. The effects of rotation on internal wave dynamics were investigated almost exclusively in the context of plane inertia-gravity waves.

The dynamics of linear internal waves in the ocean taking into account the vertical and horizontal component of Earth's rotation (not assuming *f-plane approximation* mentioned in section 2.2) was analysed by Gerkema and Shrira (2005b). They found that the horizontal inhomogeneities in the Coriolis parameter enable a transition from super-inertial to sub-inertial waves and thus effectively facilitates an irreversible transformation of large-scale into small-scale motions providing a mechanism for mixing in the deep ocean. The propagation of linear near-inertial waves in the specific case of *β -plane approximation* was considered in Gerkema and Shrira (2005a).

Reflection of plane internal waves obliquely incident on a slope in a stratified rotating fluid was examined by Thorpe (1997) using asymptotic analysis to study the nonlinear interac-

tions in the reflection region. However, he also noted the presence of an along-slope lateral drift when the field of the incident internal waves is anisotropic in lateral direction. This anisotropy can be due to the presence of background rotation, background mean currents, or local topography constraining the directionality of the wave field or where local sources of waves exist. Later Thorpe (2000) summarised the effects of rotation on the reflection of internal waves on a slope and concluded that for reflecting plane waves, the Lagrangian along-slope drift is enhanced in the presence of rotation and a drift is generated even when the incidence is normal to the slope. The Eulerian upslope current was also found to be enhanced by a factor $O(2)$.

Weakly nonlinear reflection of internal waves from uniform slopes in a stratified rotating fluid was studied under Traditional and Non-traditional approximations by Gerkema (2006). They examined the effects of Non-traditional approximations on the resonant forcing of second harmonics and found that Non-traditional effects favour resonant forcing at near-tidal frequencies. Gerkema (2006) also discussed the results from two-dimensional numerical simulations of reflection of internal wave beams.

Hitherto, studies of inertia-gravity waves were limited to considering propagation and reflection of plane internal waves or internal wave beams in a two-dimensional vertical plane. There is no literature available discussing a three-dimensional inertia-gravity wave beam to the best of our knowledge.

5.1 NUMERICAL MODEL AND FORCING

We are using the model called NHOES (Non-Hydrostatic Ocean model for Earth Simulator) developed by H. Aiki (Aiki and Yamagata, 2004). This model solves non-hydrostatic incompressible Boussinesq equations discretised with Arakawa's C-grid. The model introduces a viscous term in the momentum equation with a kinematic viscosity, ν , and a diffusive term in the advection equation with a diffusivity, κ . The governing equations 5.1 are solved using a finite volume method in Cartesian coordinates with uniform grid spacing. A leap-frog scheme is used for time integrations. We used a linear equation of state depending on salinity alone in order to simulate the laboratory experiment.

For the velocity vector \mathbf{u} , pressure p and density ρ with a reference density ρ_0 , the governing equations can be written as follows.

$$\frac{\partial \mathbf{u}}{\partial t} + (\nabla \times \mathbf{u}) \times \mathbf{u} + \frac{1}{2} \nabla \mathbf{u}^2 = -\nabla p - f \hat{\mathbf{e}}_z \times \mathbf{u} - \frac{\rho g}{\rho_0} \mathbf{e}_z + \nu \nabla^2 \mathbf{u} + F_x \hat{\mathbf{e}}_x \quad (5.1a)$$

$$\frac{\partial \rho}{\partial t} + \nabla \cdot (\mathbf{u} \rho) = \kappa \nabla^2 \rho \quad (5.1b)$$

$$\nabla \cdot \mathbf{u} = 0 \quad (5.1c)$$

where ν and κ are the kinematic viscosity and diffusivity of the fluid respectively, f is the

No.	ω (rad s^{-1})	f (s^{-1})	N (s^{-1})	θ (deg)	C_g (m s^{-1})	f/ω
1	0.1991	0.15	0.42	19.5	0.0048	0.7534
2	0.2349	0.20	0.42	19.5	0.0036	0.8514
3	0.2742	0.25	0.42	19.5	0.0026	0.9117
4	0.3157	0.30	0.42	19.5	0.0017	0.9503

Table 5.1.1: Table of simulations performed with their relevant parameters. The simulations are done for 4 different values of Coriolis parameter f keeping the angle of propagation of the wave beam with the horizontal axis θ kept as a constant by changing the wave frequency ω appropriately. The Brunt-Väisälä frequency N is also fixed for all simulations. The group velocity C_g and a non-dimensional parameter f/ω are also listed for the simulations.

Coriolis parameter and g is the acceleration due to gravity and F_x is the wave forcing.

The following forcing function is added to the right hand side of the x-momentum equation at the left boundary of the domain.

$$F_x(0, y, z) = U E_y E_z \left((1 - e^{-\frac{5t}{T}}) \omega \sin(k_z z - \omega t) + \left(\frac{5t}{T} \right) e^{-\frac{5t}{T}} \cos(k_z z - \omega t) \right) \quad (5.2a)$$

$$E_z = \frac{1}{2} \left[1 + \tanh \left\{ \frac{3}{2} \tan \left(-\frac{\pi}{2} + \frac{1}{2} \min[2\pi, \max\{0, \pi(n_\lambda + 1) - k_z |z - z_0|\}] \right) \right\} \right] \quad (5.2b)$$

$$E_y = \frac{1}{2} \left[1 + \tanh \left\{ \frac{3}{2} \tan \left(-\frac{\pi}{2} + \frac{1}{2} \min[2\pi, \max\{0, k_z (W_{\frac{1}{2}b} - |y|)\}] \right) \right\} \right] \quad (5.2c)$$

where F_x is the wave forcing in the zonal direction with a velocity amplitude U , wave frequency ω , wave period T , and vertical wave number k_z . The forcing at the left boundary generates a plane wave in a vertical plane for the zonal velocity, u and density, ρ , which is limited by a smooth envelope in y and z directions to produce a wave beam of finite dimensions. The envelop function E_z is centred at z_0 and permits n_λ number of wavelengths in the wave beam. The width of the wave beam in lateral direction is given by $W_b = 2W_{\frac{1}{2}b}$. We have used $n_\lambda = 4$ and $k_z = 48 \text{ m}^{-1}$ for all the simulations.

The numerical domain is of dimensions $2.56m$ in x-direction, $7.68m$ in y-direction and $0.8m$ in z-direction with resolutions of $\Delta x = \Delta y = 0.01m$ and $\Delta z = 0.005m$. We have a linear background stratification with a buoyancy frequency, $N = 0.42s^{-1}$. The background rotation is varied in the simulations. The sloping platform with a slope angle of $\alpha = 5.71^\circ$

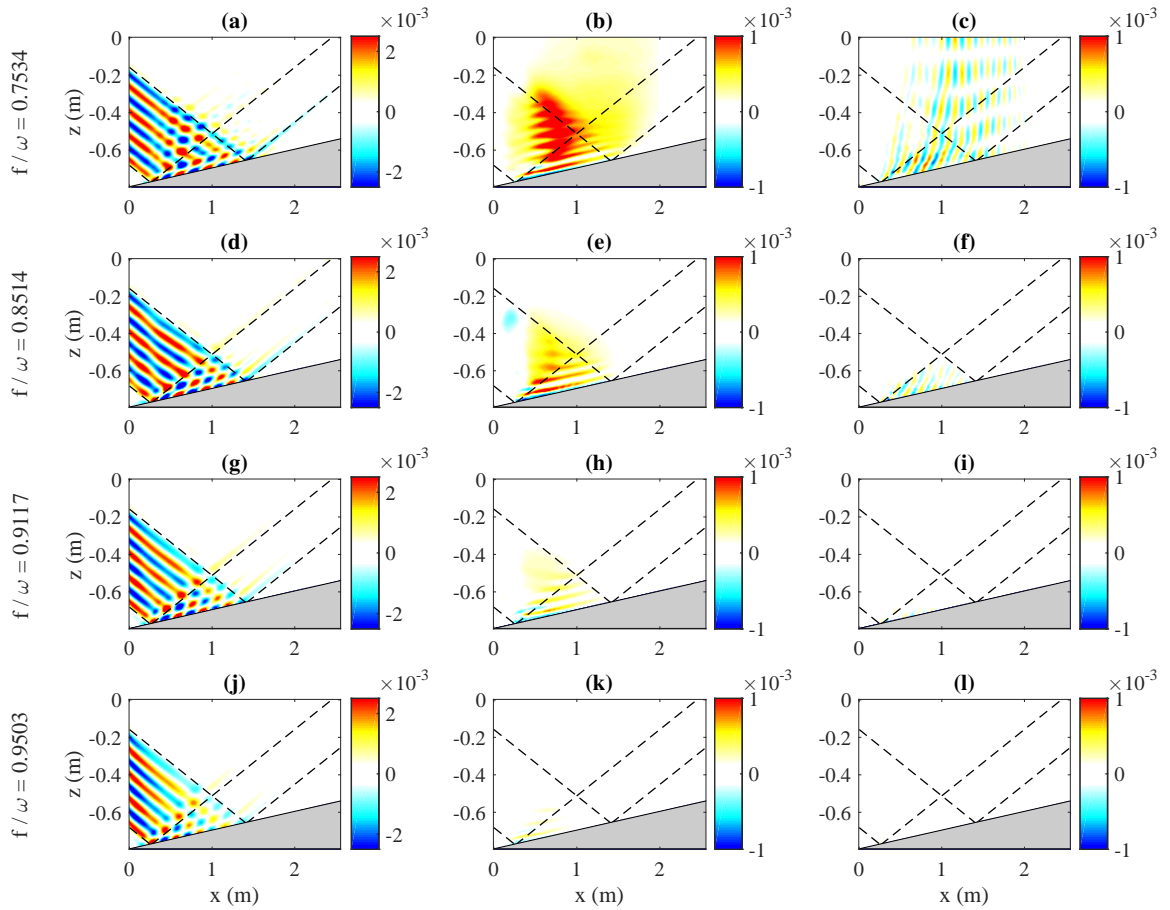


Figure 5.1.1: The zonal velocity u fields for the (left column) primary harmonic wave (filtered around the forcing frequency ω), (central column) Eulerian mean (averaged over 3 wave periods) and (right column) second harmonic wave (filtered around twice the forcing frequency), for the numerical experiments listed in table 5.1.1 at 90T.

($\tan \alpha = 10\%$) is implemented by a partial step scheme. The boundary condition at the slope is of free-slip. The domain is open at the left and right zonal boundaries (x-direction), with a wave forcing at the left and a sponge layer of thickness 0.2 m at the right boundary. The top of the domain is a free surface which is calculated using a semi-implicit scheme.

The numerical simulations performed are listed in table 5.1.1. Simulations are done for four different values of background rotation rates. We chose to maintain the angle of propagation of the incident wave beam as $\theta = 19.5^\circ$ by changing the value of the wave frequency ω appropriately. The value of θ was chosen to be the same as that for the cases without background rotation presented in the previous chapter. This is to keep the geometry of the reflection that same, so that we can distinguish the effect of background rotation on the forcing of the mean flow and reflection.

A natural non-dimensional parameter that can be identified is the ratio of the timescales of the primary harmonic wave ω and the background rotation f . The value of f/ω is close to 1 implying the waves are near-inertial. We are presenting results for four values of f/ω .

The group velocity of the wave beams depend on the Coriolis parameter f and decreases with increasing f (for constant θ) as shown in table 5.1.1. Therefore, the energy of the incident wave beam takes longer time to reach the slope for cases with higher rotation rates. We have run all the simulations for 90 wave periods in order to ensure that the wave beam had time to propagate and complete the reflection in all cases. For the highest rotation rate $f/\omega = 0.9503$, the simulation was run for 150 wave periods, but no significant changes were observed after 90 wave periods.

5.2 INDUCED MEAN FLOW AND EFFECT OF CORIOLIS FORCE

The velocity fields were filtered using a sliding band-pass filter centred at the forcing wave frequency and with a window of three wave periods to obtain the primary wave velocity fields. A similar filter centred at twice the wave frequency was used to get the fields for the second harmonic wave. The Eulerian mean flow fields were obtained using a sliding time average over three wave periods. Figure 5.1.1 shows the results from the simulations for different values of f/ω . The left column shows the zonal velocity field of the primary harmonic wave, the centre column shows the zonal Eulerian mean velocity and the right column shows the zonal velocity field of the second harmonic wave.

We can readily notice in the figures in the central column of 5.1.1 that the Eulerian mean velocity decreases drastically with increasing rotation rate (increasing f/ω) and the amplitude of the mean velocity is weaker than the non-rotating cases in chapter 4. We can also notice in figure 5.1.1(b) that the mean velocity develops vertically outside the wave beam. This is due to the induced mean velocity being in geostrophic balance. In the highest rotation rate we analysed, there was no Eulerian mean velocity induced by the wave beams as can be seen in figure 5.1.1(k).

In the left column of figure 5.1.1, we can see the primary harmonic wave. We can notice that

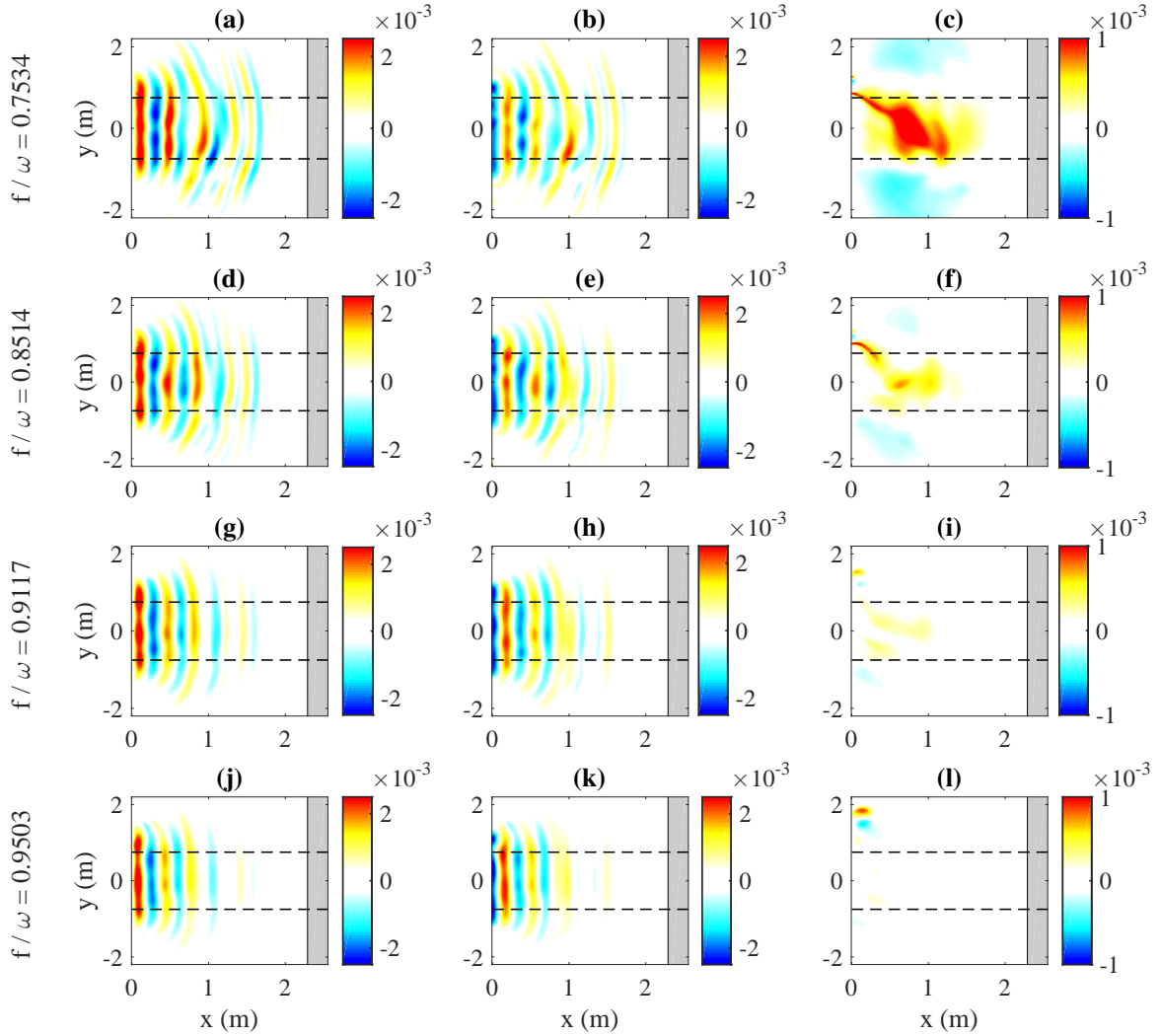


Figure 5.2.1: The zonal velocity fields of the primary harmonic (left column), the longitudinal velocity fields of the primary harmonic (central column) and the zonal Eulerian mean velocity fields (right column) for the numerical experiments listed in table 5.1.1 at 90T.

the reflected wave is nearly absent in all cases, suggesting that almost all of the incident wave energy is either dissipated or transferred to the mean flow or higher harmonics. We can also observe that the incident wave beams are attenuated as they propagate towards the slope. The attenuation increases in severity with the increase in the rotation rate, so much so that for the highest rotation rate, the incident wave hardly reaches the slope in figure 5.1.1(j). Therefore, the interaction of the incident and reflected wave beams close to the slope is suppressed in the case of higher f/ω . This is why we do not see the spatially periodic Eulerian mean flow in these cases (figures 5.1.1(h) and (k)).

In the right column of figure 5.1.1, we can see the second harmonic waves generated by the interaction of incident and reflected wave beams. As we mentioned above, the interaction of incident and reflected wave beams occur only for lower rotation rates. Thus we can clearly see that the second harmonic waves are generated only for cases with lower f/ω (figures 5.1.1(c) and (f)). For the lowest value of f/ω , in figure 5.1.1(c), we can also notice that the second harmonic wave beam is refracted by the vertically developing zonal mean flow as it propagates away from the slope.

The velocity fields presented in figure 5.1.1 suggest that the wave momentum is not transferred to the mean flow or higher harmonics for cases with higher background rotations. The zonal and lateral velocity (u and v , respectively) fields of the primary harmonic and the Eulerian mean velocity fields in the horizontal plane $z = -0.57m$ are shown in figure 5.2.1. The lateral velocity v of the primary harmonic is forced by the Coriolis force ($f u$). Therefore, the amplitude of the lateral velocity can be seen to be increasing with increasing f/ω (central column in figure 5.2.1). We can also see the mean flow decreasing with increasing f/ω .

We are forcing the system in the zonal direction at the left boundary wall. In the presence of background rotation, the zonal velocity of the inertia-gravity waves forces wave motions in the lateral direction. Thus, with background rotation, the zonal wave momentum is deflected by the Coriolis force in the lateral direction, causing lesser transfer to the zonal mean motions than in the case without rotation. As f/ω increases, the Coriolis force increases and most of the zonal wave momentum is deflected in lateral direction, causing stronger lateral velocity and no zonal mean flow in figure 5.2.1(k) and (l), respectively.

The deflection of zonal wave momentum to force wave motions in the lateral direction leaves a very weak forcing for the mean vertical vorticity in the horizontal plane, unlike in the cases without rotation. We can see the mean vertical vorticity (in colour) and mean velocity vectors in the horizontal plane $z = -0.57 m$ in figure 5.2.2 for the simulations with $f/\omega = 0.7534$ and 0.8514 . For simulations, with higher f/ω , the mean vertical vorticity field is too weak to be displayed in the same scale. We can observe an asymmetric vortex dipole for $f/\omega = 0.7534$ in figure 5.2.2(a), but for $f/\omega = 0.8514$ in figure 5.2.2(b), there is hardly a coherent vortex structure within the beam. We can also note some strong vorticity in the edge of the beam close to the forcing wall. This can be associated with Kelvin waves that propagate along the forcing wall close to the wave envelop.

The vortex dipole shown in figure 5.2.2 grows in time and continue to turn in the horizontal

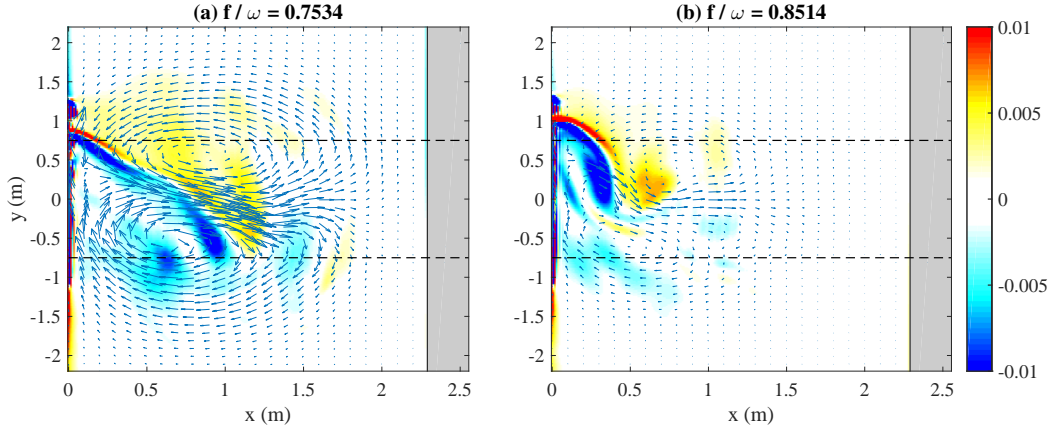


Figure 5.2.2: Mean curl of the horizontal velocity fields (in colour in s^{-1}) and the velocity vectors (arrows) for the numerical experiments with $f/\omega = 0.7534$ and $f/\omega = 0.8514$ at 90T.

plane. Since there is no fixed horizontal axis of symmetry, the evolution of the vortex field can be quantified using the first moment of the vertical vorticity (which is also equal to the mean momentum integrated in the horizontal plane) defined as follows.

$$P_x = \int_S y \overline{\Omega_z} dx dy \left(= \int_S \overline{u} dx dy \right) \quad (5.3)$$

$$P_y = - \int_S x \overline{\Omega_z} dx dy \left(= \int_S \overline{v} dx dy \right) \quad (5.4)$$

where $\overline{\Omega_z}$ is the mean vertical vorticity in the horizontal plane. The integration is done in an area avoiding the regions close to the boundaries. S is the area of integration defined as $(x, y) = (0.27 : 2.30, -2.20 : 2.20)$ m. The evolution of the components of the moment of the mean vertical vorticity are shown in figure 5.2.3 (a) and (b). The evolution of the moment for the case $f/\omega = 0$ (the reference case in chapter 4) is also shown in black dotted line. The amplitude of the moment is shown in figure 5.2.3 (c) and the angle made by the moment with the x-axis is shown in figure 5.2.3 (d) for 90 wave periods.

We can readily notice that the mean vorticity is much weaker in the presence of background rotation. However, as with the non-rotating case, the x-component of the moment in the horizontal plane P_x grows with time for rotating cases too, implying the growth of the horizontal mean flow. The growth is lower as f/ω increases. The vorticity field is very weak for higher values of f/ω , so we show only for $f/\omega = 0.7534$ and $f/\omega = 0.8514$. We can notice in figures 5.2.3 (b) and (d) that the dipole vortex slowly oscillates with respect to the x-axis. For $f/\omega = 0.8514$, the dipole is making a larger angle with respect to the x-axis. This

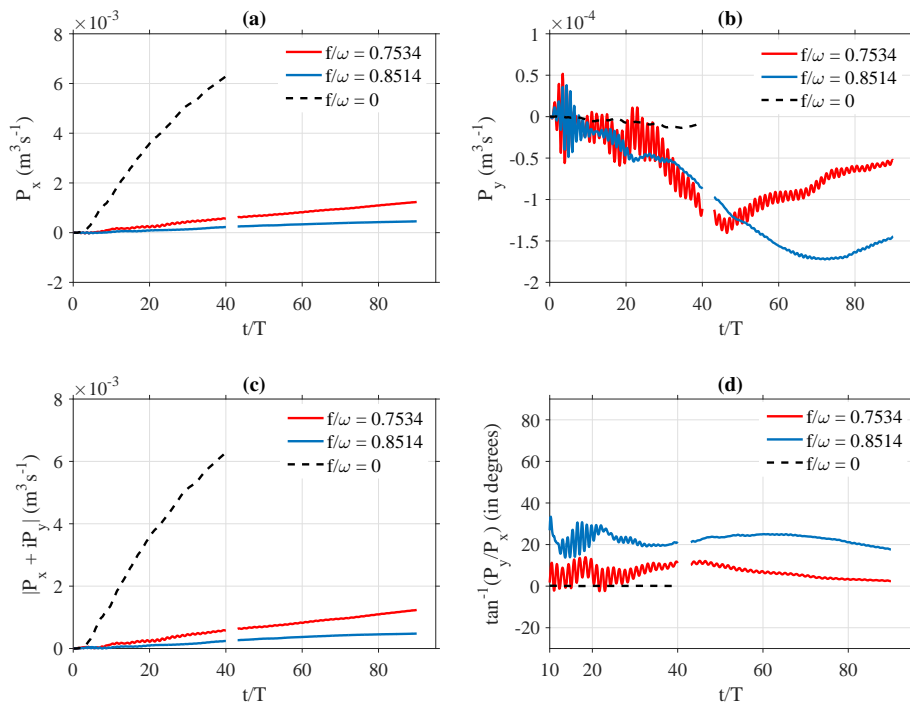


Figure 5.2.3: The components of the moment of the vertical vorticity (a) P_x and (b) P_y in the horizontal plane $z = -0.57m$ for $f/\omega = 0.7534$ (red) and $f/\omega = 0.8514$ (blue). The amplitude of the moment of vertical vorticity is shown in (c) and the angle of the moment with respect to the x-axis is shown in (d). The **black dotted line** corresponds to $f/\omega = 0$ (reference case in chapter 4), plotted here to show the effect of background rotation.

No.	E_i	E_o	E_{w2m}	E_{w2h}	D
1	10.44	0.52 (5.0%)	0.72 (6.9%)	0.84 (8.0%)	8.35 (79.9%)
2	7.98	0.22 (2.7%)	0.36 (4.5%)	0.43 (5.4%)	6.96 (87.3%)
3	6.45	0.08 (1.0%)	0.13 (2.0%)	0.00 (0.0%)	6.24 (96.7%)
4	4.87	0.04 (0.8%)	0.00 (0.0%)	0.00 (0.0%)	4.83 (99.2%)

Table 5.2.1: Energy balance terms (μW) for the wave and mean fields at the end of 90 wave periods. E_i , E_o , E_{w2m} , E_{w2h} and D are the wave energy influx, the wave energy efflux, the flux of energy from wave to the mean flow, the flux of energy from wave to higher harmonics and the dissipation of wave energy in the domain, respectively. The percentage values in parentheses are with respect to the wave energy influx, E_i .

might be due to the domination of the vorticity arising from the edge of the wave beam

5.3 ENERGY BUDGET

We have also performed energy budget of the system in the same way as described in chapter 4 in order to estimate the transfer of energy from the wave to the mean flow. The energy balance equations for the primary harmonic and mean fields can be written as follows.

$$\frac{\partial E_{wave}}{\partial t} = (\text{Influx}_{wave} - \text{Efflux}_{wave}) + \text{Dissip}_{wave} + (\text{Sink}) \quad (5.5)$$

$$\frac{\partial E_{mean}}{\partial t} = (\text{Influx}_{mean} - \text{Efflux}_{mean}) + \text{Dissip}_{mean} + (\text{Source}) \quad (5.6)$$

We can identify the sink of energy of the wave field and the source of energy for the mean field. The difference between the sink of wave energy and the source of mean flow energy can be estimated to be the energy transferred to higher harmonics. In the table 5.2.1, the influx of primary harmonic wave energy ($\text{Influx}_{wave} = E_i$), the efflux of primary harmonic wave energy associated with the reflected wave ($\text{Efflux}_{wave} = E_o$), the flux of energy from the primary harmonic to the mean flow ($\text{Source} = E_{w2m}$), the flux of energy from the primary harmonic to the higher harmonics ($\text{Sink} - \text{Source} = E_{w2h}$) and the dissipation rate of the primary harmonic wave energy ($\text{Dissip}_{wave} = D$) are shown.

We can notice that almost all of the incoming wave energy is dissipated in the domain. The outgoing energy flux associated with the reflected wave beam is very small (6% of the incoming wave energy flux) even for the lowest value of f/ω and decreases further with increasing f/ω . The rate of energy transfer from the wave to the mean flow and higher harmonics also decrease with increasing value of f/ω .

5.4 CONCLUSIONS

We have studied the reflection of three-dimensional internal wave beam under background rotation using numerical simulations. We performed 4 simulations of varying Coriolis frequencies. The angle of propagation of the wave beam was kept constant (same as the cases in chapter 4) in all those simulations by varying the wave frequency accordingly, so that the geometry of the reflection is the same. The amplitude of the zonal velocity of the wave, wavelengths, width of the beam and fluid viscosity are same as the reference case in chapter 4. With the change in wave frequencies and Coriolis frequencies, the group velocities will also change. In order to give the wave energy time to reach the slope in all our simulations, we performed the simulation for 90 wave periods.

We can see that the mean flow is highly diminished in the presence of rotation (even for the lowest f/ω case, the mean flow is 2.5 times lower than the reference case in chapter 4) and continue to decrease as f/ω is increased. As f/ω approaches the value of 1, there is no mean flow induced by the wave (in the case of $f/\omega = 0.9503$ in our simulations).

In the presence of background rotation, the zonal momentum is deflected by the Coriolis force to lateral direction in order to force wave motions in that direction. The forcing of lateral wave motions decreases the forcing of the induced mean flow. The mean velocity that is present for lower f/ω values is also deflected by the Coriolis force, thereby distorting the dipole vortex structure in the horizontal plane.

The growth of the mean flow can be quantified using horizontal moment of the vertical vorticity in a horizontal plane $z = -0.57m$. We noticed that the growth of the mean flow decreases with increasing f/ω . The dipole vortex formed by the mean flow slowly oscillates with respect to the x -axis.

We also performed the energy budget (in the same way as mentioned in chapter 4) in order to estimate the energy flux into the mean flow and higher harmonics. We find that in all our cases, almost all of the wave energy (more than 80%) is dissipated in the domain and the dissipation increases with f/ω . The energy flux into the mean flow and second harmonics is very small (less than 10%) in the case of lowest f/ω and it decreases further with increasing f/ω . For the highest value of Coriolis frequency we studied ($f/\omega = 0.9503$), the energy flux into the mean flow and second harmonics is less than 0.1%.

The propagation and reflection of three-dimensional inertia-gravity wave beams with finite lateral extent have never been studied before, to the best of our knowledge. The effect of Coriolis force on the generation of mean flow by internal wave beams is yet to be explained analytically. There are ongoing attempts by some to derive a steady state solution for the propagation of inertia-gravity wave beams with finite lateral extent in collaboration with the author.

It doesn't matter how beautiful your theory is, it doesn't matter how smart you are. If it doesn't agree with experiment, it's wrong.

Richard Feynman, on scientific method (talk)

6

Laboratory modelling of Antarctic Circumpolar Current

ANTARCTIC CIRCUMPOLAR CURRENT (ACC) is a major eastward flowing ocean current in the Southern Ocean around the continent of Antarctica. ACC is the only ocean current that completes a circumpolar loop unobstructed by any land masses. ACC was discovered by the English astronomer, Edmund Halley*, while he was surveying the Southern ocean on board HMS *Paramore* during 1699-1700. Ever since that, ACC has been notorious among many sailors for its strength and the rough seas it creates.

* of Halley's comet fame

The Antarctic Circumpolar Current is often called the “great ocean conveyor”, as it connects the Atlantic, Indian and Pacific oceans and facilitates the transport of mass and energy among these ocean basins (figure 6.0.1). It is one of the largest ocean current with a mean transport of about 100-150 Sverdrups*. In the Drakes passage (the narrowest part of the Southern ocean at southern tip of South America), the ACC was measured using moored instruments in the upper 2.5 Km and it was estimated to be carrying around 118-143 Sverdrups of ocean water (Whitworth III, 1983) However with the recent measurements, it has been found that these estimates might be short by about 30% (Donohue et al., 2016).

* 1 Sverdrup = $10^6 m^3 s^{-1}$

The northern boundary of the ACC is defined by the Sub-antarctic Front which is found between 48°S and 58°S in the Pacific and Indian oceans and between 42°S and 48° in the Atlantic. The southern boundary is defined by an upwelling region called the Antarctic Divergence (Nowlin and Klinck, 1986). However, Orsi et al. (1995) proposes the southern edge of the Upper Circumpolar Deep Water to be the southern edge of the ACC. These put

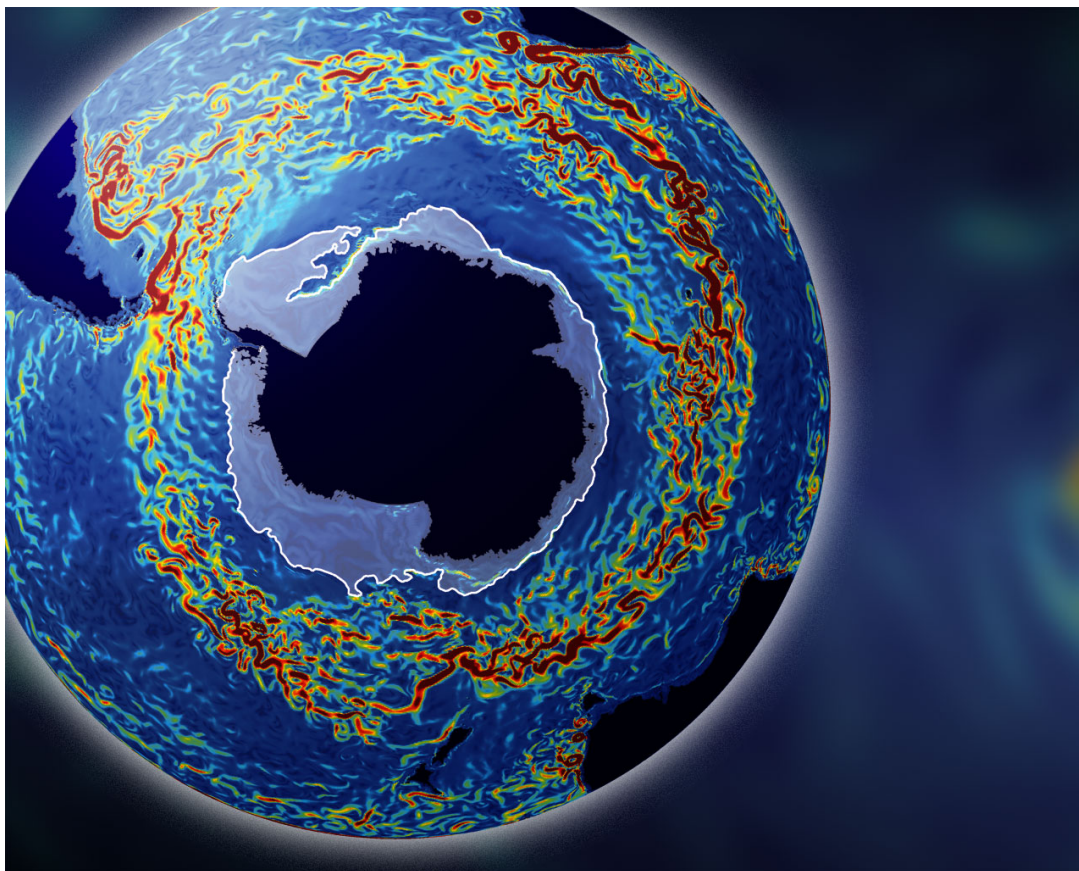


Figure 6.0.1: The map shows the speed of the clockwise Antarctic Circumpolar current on May 12, 2006, increasing from slow-moving blue water to dark red indicating speeds above one mile per hour. (Image courtesy: M. Mazloff, MIT; Source: San Diego Supercomputer Center, UC San Diego)

the southern boundary of the ACC to be roughly between 60°S and 70°S .

The forcing of ACC comes from strong, persistent westerly winds with an average wind speed of 15 to 24 knots in the southern ocean. It can be found that the surface wind stress is enough to drive ACC (the velocity of the current being the result of a balance between the surface wind stress and bottom friction). However, the mechanisms by which the input momentum exits the system is still an active topic of research. The balance among the input surface wind stress, form stress across bottom topography, interfacial form stress and the net meridional transport in each layer contributes to the average transport in the ACC. The mean velocity of ACC is about 10 cm s^{-1} , rising to about 2-3 times this value near fronts.

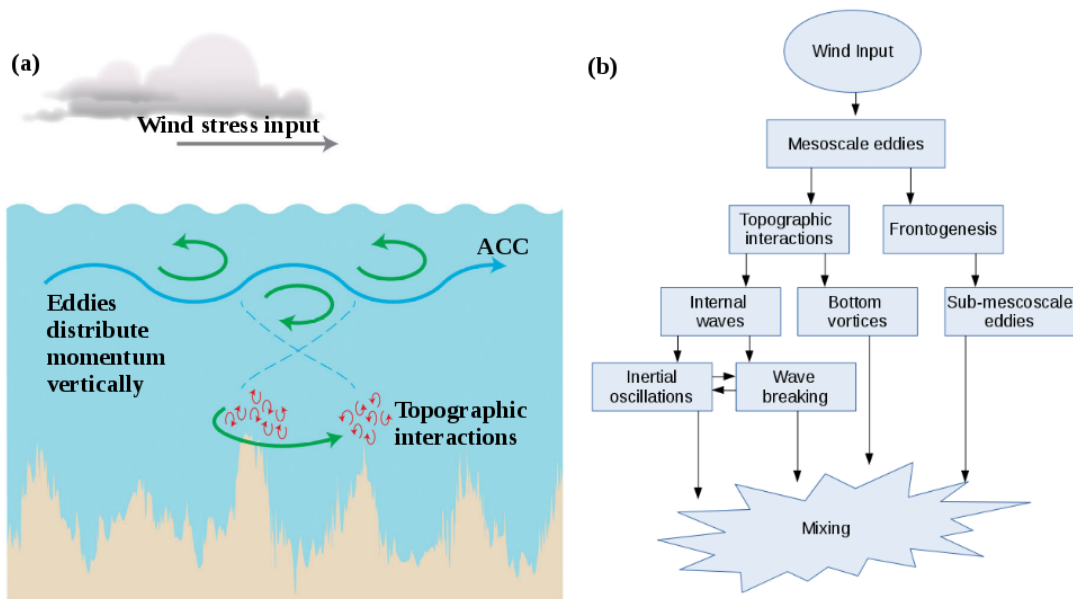


Figure 6.1.1: (a) Strong westerly winds (grey) over the Southern Ocean force the Antarctic Circumpolar Current (blue). The current would keep accelerating over time except that it becomes unstable, giving rise to strong eddies that are visible to satellites as bumps or dips in sea surface height. Although the mean current at depth is weak, eddies (green) can be strong, leading to internal wave generation by flow over rough topography. The internal waves then generate turbulence (red) that provides a source of energy for the mixing of abyssal waters, which, in turn, hastens the global overturning circulation (Image from MacCready (2014)). (b) Energy cascade in the southern ocean.

6.1 DISSIPATION OF ENERGY IN THE SOUTHERN OCEAN

The Antarctic Circumpolar Current is considered as one of the main sources of mixing in oceans, as mentioned in the chapter 1. Recent observations by Garabato et al. (2004a) in the southern ocean have shown that the interaction of ACC with the ocean bottom topography can generate internal waves which transport momentum vertically contributing to bottom friction. These waves break in the ocean interior leading to turbulent mixing playing an important role in the upward transport of water closing the meridional overturning circulation (Polzin et al., 1995).

The generation and dissipation of internal waves by geostrophic motions impinging on ocean topography was studied theoretically by Nikurashin and Ferrari (2010). They used weakly nonlinear theory and idealised two-dimensional simulations to study the generation of waves by the mean flow and the feedback of the dissipating waves on the zonally averaged mean flow. They found that the waves generated at steep topographies drive vigorous inertial oscillations. The strong vertical shear associated with these inertial oscillations drive

enhanced wave breaking and high mixing rates above rough topographies. The theoretical estimates agree well with the observations of [Garabato et al. \(2004a\)](#).

[Nikurashin and Ferrari \(2011\)](#) estimated the global distribution of generation of internal waves by ocean currents and eddies using linear lee-wave theory. They found that the total energy flux into lee waves in the global ocean was around 0.2 TW which is about 20% of the total wind power input into the ocean system (see section 1.2). They also found that the geographical distribution of the energy flux into lee waves is largest in the Southern Ocean which accounts for half of the total energy flux into lee waves. [Scott et al. \(2011\)](#) also used linear lee-wave theory to come to an estimate of about 0.4 TW of energy conversion into lee waves with higher concentration in the Southern ocean. [Nikurashin and Ferrari \(2013\)](#) have produced a three-dimensional distribution of internal wave-driven diapycnal mixing by combining the global energy flux to lee waves with a turbulent mixing parameterisation. Using this, they estimated that the mixing caused by lee waves can sustain 20-30 Sverdrups of water-mass transformation, and almost one third of this transformation can be attributed to lee waves generated by the ACC in the Southern ocean.

The various ways in which the energy of the geostrophic flow is dissipated in the Southern ocean was studied by [Nikurashin et al. \(2013\)](#) using a high resolution model resolving mesoscale and sub-mesoscale eddies and as well as internal waves generated by the topography. In Southern ocean, where lateral boundaries are absent, geostrophic eddies must transfer their energy to smaller scale unbalanced motions by generating sub-mesoscale eddies in the upper oceans or interacting with the bottom topography ([Waterman et al., 2013](#)). [Nikurashin et al. \(2013\)](#) showed that most of the conversion of geostrophic eddies to smaller scales happen in the abyssal ocean, catalysed by rough, small-scale topography. The bulk of the energy is dissipated in the region close to the topography but about one fifth of it is radiated away into ocean interiors as lee waves which might break and sustain turbulent mixing. The remaining conversion of geostrophic eddies should come from generation of fronts and sub-mesoscale eddies in the upper ocean.

However, more recent observations from the Diapycnal and Isopycnal Mixing Experiment in the Southern ocean (DIMES) ([St. Laurent et al., 2012](#)) finds that the linear theory and idealised two-dimensional numerical models overestimate the observed turbulent energy dissipation in the Southern ocean. [Nikurashin et al. \(2014\)](#) performed two-dimensional and three-dimensional numerical simulations using realistic topography and found that the internal wave generation at three-dimensional topography is reduced compared to the case of two-dimensional topography. The difference between the two likely arises due to the fact that in the three-dimensional topography case, the fluid has the option to flow horizontally around the topography.

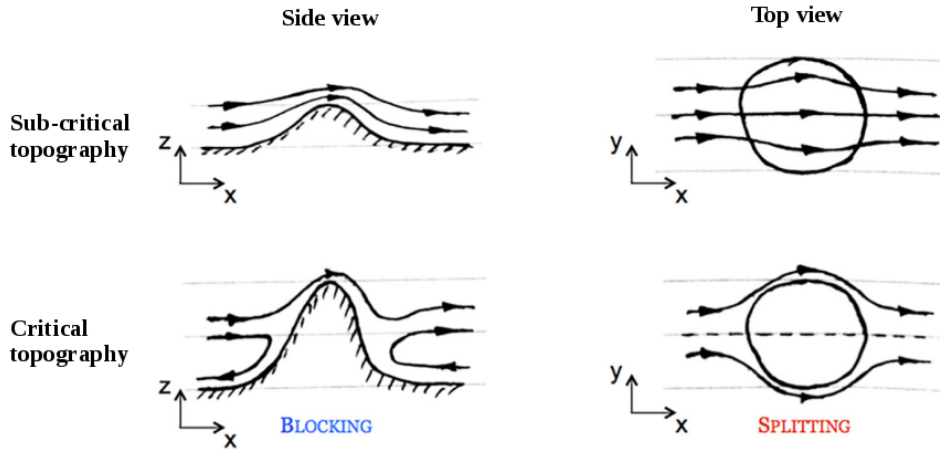


Figure 6.2.1: A sketch of the mean flow–topography interaction: (top) sub-critical topography limit and (bottom) critical topography limit; (left) vertical plane view and (right) horizontal plane view. The bottom two panels illustrate the blocking and splitting effects arising in the critical topography limit. (Image courtesy: Nikurashin et al. (2014))

6.2 STRATIFIED FLOW OVER THREE-DIMENSIONAL TOPOGRAPHY

Stably stratified flow over an obstacle have been studied for a long time as it represents a fundamental problem in geophysical fluid dynamics. The generation of lee waves by a uniform mean flow over a topography is a well-studied problem (Scorer (1949), Miles and Huppert (1968), Bell (1975a), Lighthill (1978), Baines (1998), Dalziel et al. (2011)). The linear theory (refers to linearised boundary condition) for a steady stratified flow over a three-dimensional topography was given by Drazin (1961). It is valid for topographic height smaller than the vertical internal wave scale (sub-critical topography). If the topography is expressed as $z = h(x, y)$ and the steady mean flow velocity as U_0 , the boundary condition $w = w_0(x, y)$ can be applied at $z = 0$ rather than applying $\mathbf{u} \cdot \nabla(z - h) = 0$ on the surface of the topography. Then the linearised boundary conditions can be written as

$$w_0 = U_0 \frac{\partial h}{\partial x} \quad (6.1)$$

The linearised boundary condition implicitly assumes that the mean flow has sufficient kinetic energy to rise up and over the topography. If we note that the work required to raise a fluid parcel in a uniformly stratified fluid by a height h is $\frac{1}{2}gh^2 \frac{d\hat{\rho}}{dz}$ and the energy available to the flow with a mean velocity U_0 is its kinetic energy given by $\frac{1}{2}\rho_0 U^2$, then the condition for the flow to completely rise over the topography is given by

$$\frac{1}{2}\rho_0 U_0^2 \geq \frac{1}{2}gh^2 \frac{d\hat{\rho}}{dz} \implies Fr_h = \frac{U_0}{Nh} \geq 1 \quad (6.2)$$

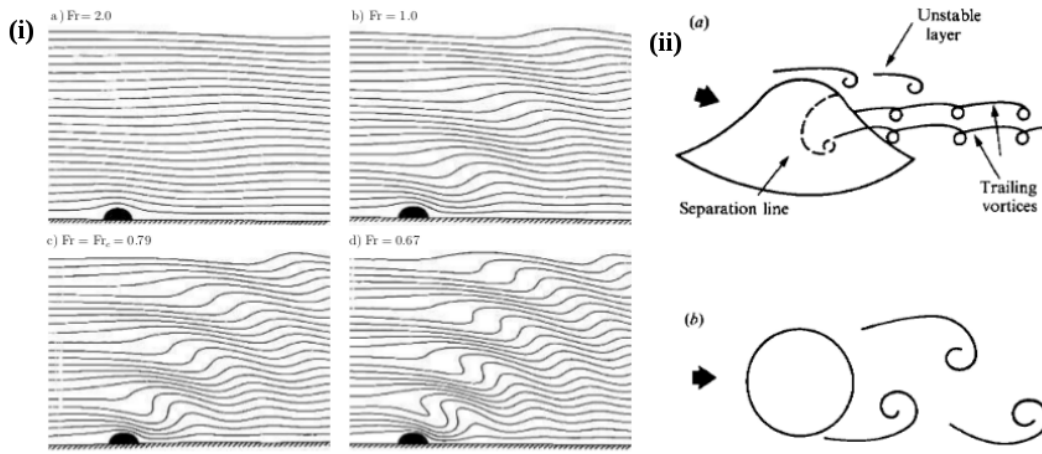


Figure 6.2.2: (i) From the theoretical calculations of Miles and Huppert (1968) for two-dimensional topography (for high Froude numbers, 3D topography behaves like 2D one), contours showing the displacement of isopycnal surfaces resulting from uniformly stratified flow upstream of speed U_0 moving over a semi-circular hill of radius R . Vertically propagating internal waves are launched more efficiently as the Froude number decreases. (ii) Sketches from Richards et al. (1992) of the separated flow behind a three-dimensional hill for (a) a non-rotating flow (perspective view) and (b) a rapidly rotating flow (plan view). The vortices are shed when there is background rotation, while it remains as trailing vortices in the absence of rotation.

where Fr_h is a Froude number. In two-dimensional simulations, if the flow has a Froude number $Fr_h < 1$, then the flow will be partially blocked by the topography and a stagnant layer form upstream (6.2.1).

For an isolated three-dimensional obstacle in an otherwise flat plane, Drazin (1961) has proposed that the flow can be considered to be split into two regions. The flow below a critical height h_c of the topography is essentially two-dimensional and moves horizontally around the obstacle (splitting). Then a vortical wake is produced, with the possibility of periodic vortex shedding as we will mention below. The flow above the critical height h_c can go over the topography and generate lee waves. It can be showed that for an axisymmetric mountain of radius R , the critical height h_c is given by

$$h_c = R(1 - \alpha_T Fr_R) \quad (6.3)$$

where α_T is a constant of order one and depends on the shape of the obstacle (we shall assume α_T to be 1.0 in the rest of our chapter) and Fr_R is a Froude number based on the radius of the sphere ($Fr_R = U_0/NR$).

This is similar to the concept of a ‘dividing streamline height’ (the height from which a parcel of the fluid must originate far upstream if it is to pass over the topography rather than

go around it) first proposed by Sheppard (1956) using the same energy based argument. Through many experimental and numerical studies that followed, Sheppard's formula was found to be working well at least for obstacles of low span-wise aspect ratio.

Drazin's theory was generalised and verified using experiments by Brighton (1978) for vertically varying stratified mean flow over a three-dimensional obstacle. The experiments of Brighton (1978) were using a recirculating tank for strongly stratified flows (low Froude numbers) and were visualised using dyes. They observed most of the flow went around the obstacle except for the tops of the obstacle, and noted a cow-horn shaped horizontally oriented eddy downstream of the topography. They also observed shedding of vortices for large Reynolds number and low Froude number cases.

Experimental study to describe the flow structure for stratified flow over a three-dimensional (bell-shaped) hill was done by Hunt and Snyder (1980) for a range of Froude numbers. They also verified Drazin's theory for low Froude numbers and observed lee-wave patterns and separated flow regions for higher Froude numbers.

Hopfinger et al. (1991) studied the generation of internal waves and the turbulent wake of a sphere towed through a stratified fluid using fluorescent dye technique. They found that when Froude number increases (with Reynolds number the same), there is a transition from the lee wave regime to internal waves generated by the coherent turbulent structures in the wake of the sphere. They noted that the transition occurs for a Froude number $Fr_R = 4$. Further experiments using stratified towing tanks were performed by Vosper et al. (1999) with a range of three-dimensional obstacles such as different sizes of hemispheres and cones. They measured the drag for all obstacles and found that as Froude number (based on the obstacle height) decreases, the drag coefficient increases. They also observed that vortices were shed for lower Froude numbers and it is a major contributor to the total drag.

The generation of low Froude number lee waves by a hemisphere in a uniform flow of linearly stratified fluid was studied by Dalziel et al. (2011) using a recirculating channel. They recovered the simple linear theory predictions of Drazin (1961) for low Froude number flows and observed the division of the flow region into a wave-generating cap of height RF_R and a blocking base of height $R(1 - F_R)$. They also noted that the structure of the lee waves is extremely sensitive to departures from horizontal flow.

The energy input into internal waves generated by a towed sphere at low Froude numbers was investigated experimentally by Brandt and Rottier (2015). They also noted (like Hopfinger et al. (1991)) that for $Fr > 1$, the turbulent wake of the sphere can be the dominant source in exciting internal waves. They also found a resonance in the coupling of the input wake energy to the internal wave field at a Froude number of about 0.5.

Experiments on flow of stratified rotating fluid past isolated obstacles were done by Boyer et al. (1987) for a range of Rossby, Ekman and Burger numbers. When the stratification was stronger, they observed vortex shedding for even for lower Reynolds number, owing to the flow being forced to go around the obstacle rather than above it. They also noted that if vortex shedding occurs, the vortex streets exhibit an asymmetry with stronger cyclonic eddies and weaker anticyclonic eddies if the background rotation is cyclonic (this was observed also

for homogeneous rotating flow around an obstacle by d'Hieres et al. (1989)). Boyer et al. (1987) also observed that for vertically upward rotation, the lee waves on the right, facing downstream, have a larger amplitude than their counterparts at the same location on the left.

The atmospheric vortex streets in the wake of large islands and the vortex shedding in some cases were observed by many. Etling (1989) proposed that the observed vortex shedding in the wake of the islands can be due to viscous boundary layer separation like in Karman vortex streets. Etling (1990) compared the observations with laboratory experiments and concluded that the vortex shedding in the wake of three-dimensional obstacles is influenced by both stratification and rotation. They found a critical Froude number of around 0.4 below which the vortex shedding was observed. Variations in Froude number gave different types of wakes such as line, wavy or vortex wake.

Richards et al. (1992) performed laboratory experiments of stratified rotating flow over a three-dimensional hill using towing tanks placed in a rotating platform, to study the boundary layer separation for different Rossby numbers (from $Ro = 1 - 6$). The separation was found to be strongly influenced by rotation. The topology of the flow was found to be different to that of non-rotating case in the way that they found only one dominant trailing vortex and a much narrower turbulent wake.

Three-dimensional numerical simulations were done by Schär and Durran (1997) to study the stratified non-rotating flow around an axisymmetric mountain. They showed that oscillating Karman vortex street appear when they introduce asymmetries with respect to the axis of the incident flow. They proposed that the transition into the vortex shedding regime is associated with an absolute instability of the symmetrical wake, which feeds upon the shear present at the edges of the wake

Theoretical modelling of the drag on a sphere moving horizontally in a stratified non-rotating fluid was done by Greenslade (2000) using linear gravity wave theory for large Froude numbers. For small Froude numbers, a new theory based on separating the contributions of wave generation and the wake was proposed. Starting from Greenslade's model, Voisin (2007) developed a detailed asymptotic analysis of the generation of lee waves by stratified mean flow past a sphere for large and small Froude numbers. The analysis also predicted the wave drag more accurately with the dependence of wave drag with Froude number, which was validated by comparison with existing experimental observations.

6.3 EXPERIMENTAL METHOD

The cylindrical tank of the 'Coriolis' platform, 13 m in diameter, is filled with water linearly stratified in density by salinity, up to a total height $H = 91.5\text{cm}$. A uniform circular current is produced by a small sudden change of the tank rotation speed (spin-up). This circular current persists by inertia for the duration of the experiment, typically 15 minutes, over which the flow conditions can be considered quasi-steady. A spherical cap is fixed on the flat hori-

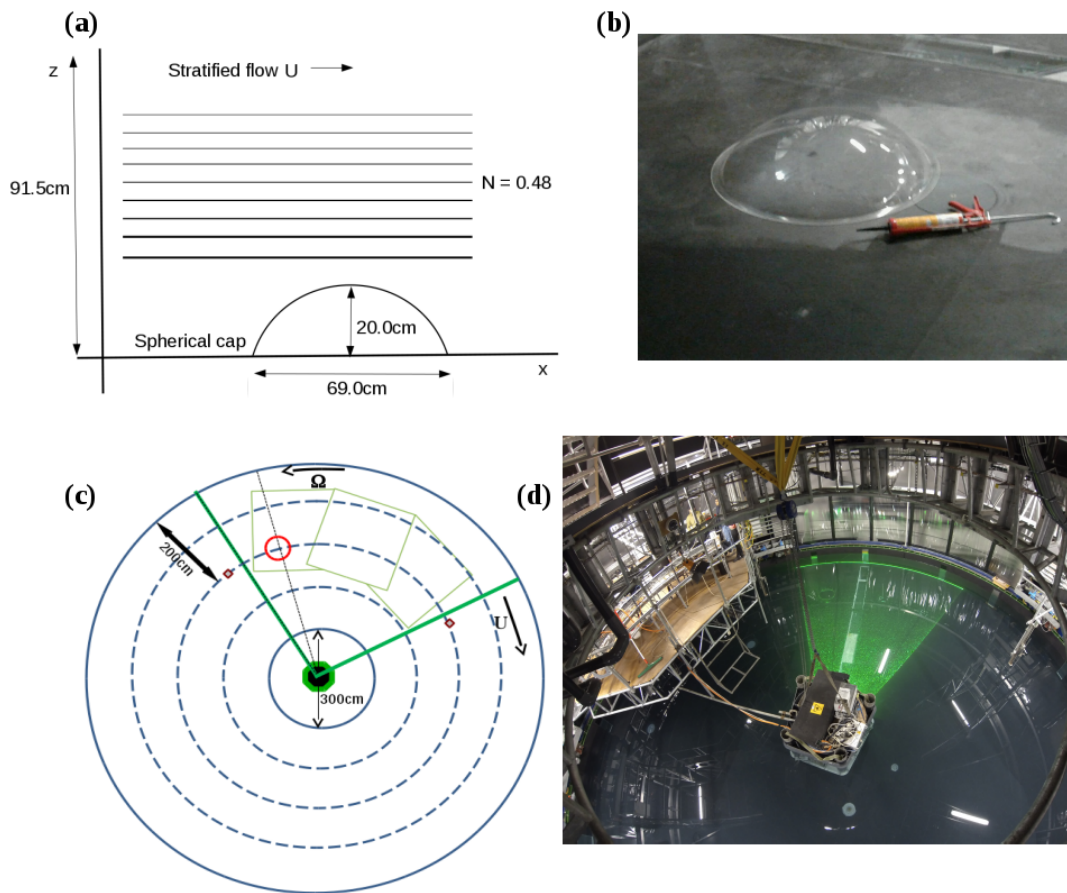


Figure 6.3.1: Experimental setup for the flow over an isolated spherical cap. (a) Schematic of the spherical cap and the mean flow. (b) Photo of the spherical cap before placement on the Coriolis platform. (c) Schematic of the experimental setup (the red circle represent the spherical cap, green circle at the centre represents the laser setup and green lines represent the edge of the laser sheet, light green rectangles represent the field of view of the three high-speed cameras and small red squares represent the position density probes). (d) Photo of the experimental setup after filling the tank with stratified water.

Parameters	Definition	Value	Unit
R_T	Radius of the tank	6.50	m
R_c	Radial position of the cap centre	4.50	m
H	Total water height	0.915	m
L	Horizontal scale of the flow	6.50	m
h	Height of the cap	0.20	m
d	Length of the cap at base	0.69	m
N	Buoyancy frequency	0.48	s^{-1}
f	Coriolis frequency	0.19	s^{-1}
h/d	Aspect ratio	0.29	
N/f	Frequency ratio	2.5	

Table 6.3.1: Parameters of the spherical cap and experimental setup.

No. of caps	Background rotation	Name	U_0 (cm/s)	Fr	Ro	Re
Single cap	Without rotation	A1	3	0.31	∞	6000
		B1	6	0.62	∞	12000
		C1	9	0.93	∞	18000
		D1	12	1.24	∞	24000
	With rotation	A2	3	0.31	0.24	6000
		B2	6	0.62	0.48	12000
		C2	9	0.93	0.72	18000
		D2	12	1.24	0.96	24000
Multiple caps	Without rotation	A3	3	0.31	∞	6000
		B3	6	0.62	∞	12000
		C3	9	0.93	∞	18000
		D3	12	1.24	∞	24000
	With rotation	A4	3	0.31	0.24	6000
		B4	6	0.62	0.48	12000
		C4	9	0.93	0.72	18000
		D4	12	1.24	0.96	24000

Table 6.3.2: Table of the experiments performed.

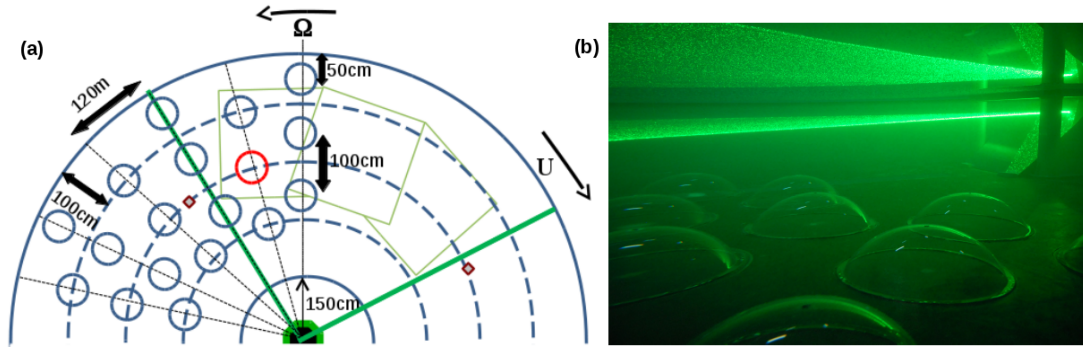


Figure 6.3.2: (a) Schematic of the experimental setup for flow over multiple spherical caps. The red circle represents a reference to define our coordinate system. It corresponds with the spherical cap used in the single mountain experiment. Blue circles represent the additional 17 spherical caps. Green circle at the centre represents the laser setup and green lines represent the edge of the laser sheet, light green rectangles represent the field of view of the three high-speed cameras. Small red squares represent the position density probes. (b) Photo of the spherical caps beneath the laser sheet in the stratified fluid.

zontal bottom of the tank, centered at a distance 2 m from the tank edge (at radius $r_0 = 4.5\text{m}$ from the tank centre) such that the lateral confinement of the wake is marginal. The cap has a height $h = 20\text{cm}$ and a diameter $d = 69\text{cm}$ at its basis, see figure 6.3.1(a). It is cut from a sphere of radius $R = 40\text{cm}$. The buoyancy frequency is set to $N = 0.48\text{s}^{-1}$ in all the experiments (corresponding to $\delta\rho/\rho = 2.15\%$ over the water height H). The multiple cap experiments are done in a similar way with a pavement of 18 identical caps as sketched in the lower part of figure 6.3.2(a). All fixed parameters of the experiment are listed in table 6.3.1.

The ‘non-rotating’ case ($f = 0$) is obtained by suddenly starting the tank rotation at angular speed $\Delta\Omega$ (anticlockwise), while the water remains at rest by inertia, yielding a clockwise fluid velocity in the reference frame of observation. The fluid velocity $U_0 = r_0\Delta\Omega$ produced above the cap is set to 3, 6, 9 or 12cm s^{-1} , such that the Froude number $Fr = U_0/(Nh)$ takes the values 0.31 to 1.25 (see table 6.3.2).

The ‘rotating’ case is similarly obtained by first preparing the stratified water layer with a tank rotation at a constant angular velocity $\Omega = 0.095\text{rad/s}$ (0.9 turns/minute). This yields a Coriolis parameter $f = 2\Omega = 0.19\text{s}^{-1}$, so that $f/N = 0.4$. At the experiment start $t = 0$, the tank velocity is suddenly increased by the amount $\Delta\Omega$ producing a clockwise fluid rotation in the reference frame like in the non-rotating case.

Vertical density profiles are measured before and during the experiment by two motorised profilers equipped with conductivity probes. Velocity fields are measured by Particle Imaging Velocimetry in horizontal planes with three cameras covering a field of width 2 m centered at the radius $r_0 = 4.5\text{m}$ of the reference cap, spanning a quarter of the periphery, see figure 6.3.1(c) and (d). The flow is illuminated by a laser sheet, produced by a rapidly oscillating

mirror ($100Hz$) from a 6 watt continuous Yag laser located at the tank centre. The laser sheet is vertically scanned at 10 successive heights z , repeated in a periodic way. A set of 100 images (during typically $25s$) is obtained at each level. Each experiment is reproduced twice to scan either the lower wake either the upper layers where waves propagate. A few experiments with a fixed laser position are also performed to get continuous time series. The fluid is seeded by polystyrene particles of diameter $0.2mm$ sorted in density to provide a uniform concentration at different heights.

The Antarctic Circumpolar Current is characterised by a buoyancy frequency $N = 7 \times 10^{-4} s^{-1}$ and a velocity $U_0 = 10 cm/s$ in the deep ocean and a Coriolis parameter $f = 1.5 \times 10^{-4} s^{-1}$, so that $f/N = 0.2$ (see e.g. Nikurashin et al. (2013)). Our range of Froude numbers 0.31 to 1.25 then corresponds to a topographic height $h = U_0/(NFr)$ in the range $460 - 115m$, and a base diameter $1600 - 400m$, if we keep the same aspect ratio $d/h = 3.5$. Accounting for the ratio f/N twice lower than the experiment, a better similarity is however expected for a twice flatter topography, with base diameter $3200 - 800m$. Indeed the ratio $(f/N)(d/h)$ is generally the relevant similarity parameter to compare situations with different aspect ratios (this is exact within the hydrostatic approximation). Our experiments with rotation are therefore representative of the effect of circular sea mounts a few kilometres in diameter and a few hundred meters in height. The Reynolds number $U_0 h/\nu$ is in the range $6000 - 24000$, which is of course smaller than in the ocean but sufficient to get instabilities and turbulent processes.

6.4 RESULTS

6.4.1 LEE WAVES

The PIV images obtained from the three CCD cameras were processed using UVMAT to obtain the velocity fields and were merged together to form a single image of the entire test section. Owing to the curvature of the tank, the fields have to be transformed into polar coordinates in order to visualise the horizontal flow clearly. The transformed fields are re-scaled to approach a cartesian geometry, hence straightening the curved streamlines associated with the circular flow around the tank. Thus x is the clockwise angular displacement with respect to the cap centre re-scaled by its reference radius $R_c = 4.5m$, while $y = r - R_c$ is the shifted radius. A reference velocity is subtracted to the azimuthal velocity to extract the wave oscillations from the mean flow. This reference is obtained at each radius as the upstream velocity measured at $x = -72$ cm (it increases linearly with radius r).

The streamwise velocity u and cross-stream velocity v at a height of $z = 25$ cm (5 cm above the spherical cap) for experiments with single cap and without background rotation (A1-D1) are shown in figure 6.4.1. We can indeed see lee waves downstream of the spherical cap. The wave pattern is set after typically 100 s (the time of advection through the measured field for the smallest velocity $U_0 = 3$ cm/s), and it then remains quasi-steady during the whole experiment.

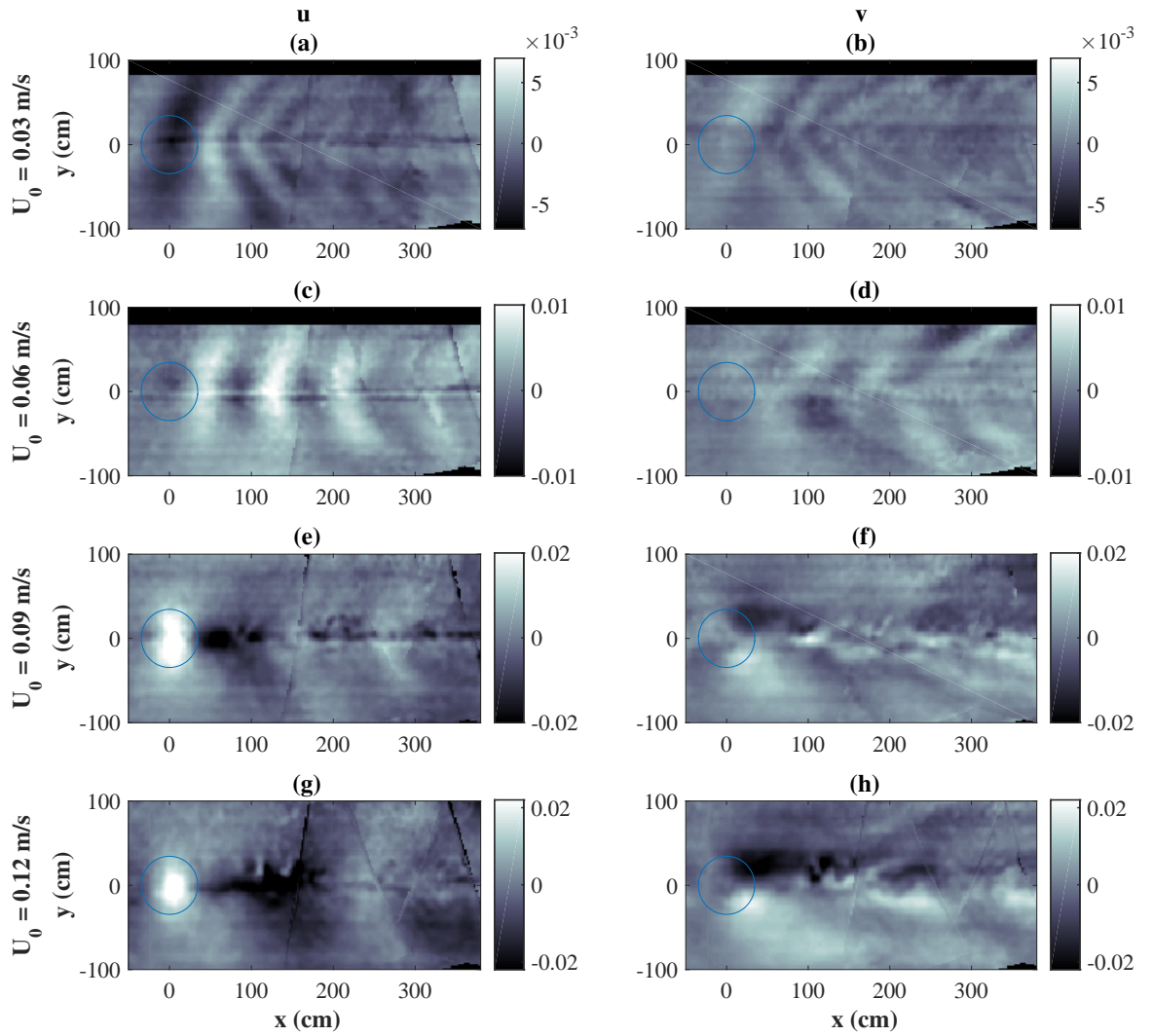


Figure 6.4.1: Horizontal cut showing the lee wave as a colour map of the stream-wise velocity perturbations for the experiments A1-D1 (no rotation) at a level $z = 25$ cm, time $t = 500$ s. The horizontal streak in the centre is due to the wake of a density probe. Oblique black lines mark the boundaries between the three camera views.

Exp. Name	U_0 (cm/s)	λ (cm)	ω (rad/s)	θ (deg)	h_s (cm)	d_s (cm)
A1	3.0	46	0.41	31	6.25	43
B1	6.0	86	0.43	24	12.5	58
C1	9.0	125	0.44	23	18.7	68
D1	12.0	170	0.44	22	20.0	69
A2	3.0	40	0.47	13	6.25	43
B2	6.0	80	0.47	13	12.5	58
C2	9.0	134	0.42	32	18.7	68
D2	12.0	190	0.40	37	20.0	69

Table 6.4.1: Calculated lee wave parameters from the experiments with single cap. The dominant wavelength λ was measured from the stream-wise velocity fields, the wave frequency ω is estimated as $2\pi U_0/\lambda$, the angle of the wavevector is deduced from the dispersion relation $\tan \theta = \sqrt{(N^2 - \omega^2)/(\omega^2 - f^2)}$, the estimated height of the spherical cap above the dividing streamline $h_s = Fr h$ and the corresponding diameter at the dividing streamline $d_s = 2\sqrt{(2R - h_s)h_s}$.

The mean velocity profile remains uniform during a time $2\pi R_c/U_0$ (equal to 500 s for $U_0 = 6$ cm/s), after which the lower velocity is perturbed upstream by the return of the wake perturbations after one revolution around the tank. Therefore the main measurements are performed in the time range 100–500 s. The lee wave structure in the absence of rotation is in reasonable agreement with the linear theory of Voisin (2007) for the wave emission of a spherical cap emerging from the horizontal plane of the dividing streamline defined above. The velocity perturbations calculated for $U_0 = 3$ and 6 cm/s by Dr. Bruno Voisin are shown in figure 6.4.2. However, significant nonlinear effects already occur even at the lower Froude number investigated ($Fr = 0.31$ for $U_0 = 3$ cm/s).

For experiments with background rotation for a single cap (A2-D2), the streamwise velocity u and cross-stream velocity v obtained are shown in figure 6.4.3 at a height of $z = 25$ cm. An asymmetry between the two sides is clearly visible in this case, with a stronger wake observed for $y > 0$ (figure 6.4.3). A fluid element impinging on the cap at $y > 0$ is first deviated away with positive transverse velocity v , then goes back to 0 with a positive streamwise velocity perturbation u (due to the lateral squeezing of the streamlines), and then comes back with $v < 0$. The velocity vector rotates clockwise in this process which fits with the natural behaviour of the inertia-gravity wave. The opposite rotation is forced on the other side, explaining the less efficient wave generation. In the case with background rotation no theory for stratified flow over an obstacle has been published to our knowledge.

The velocities were measured at different heights in the water column. The average stream

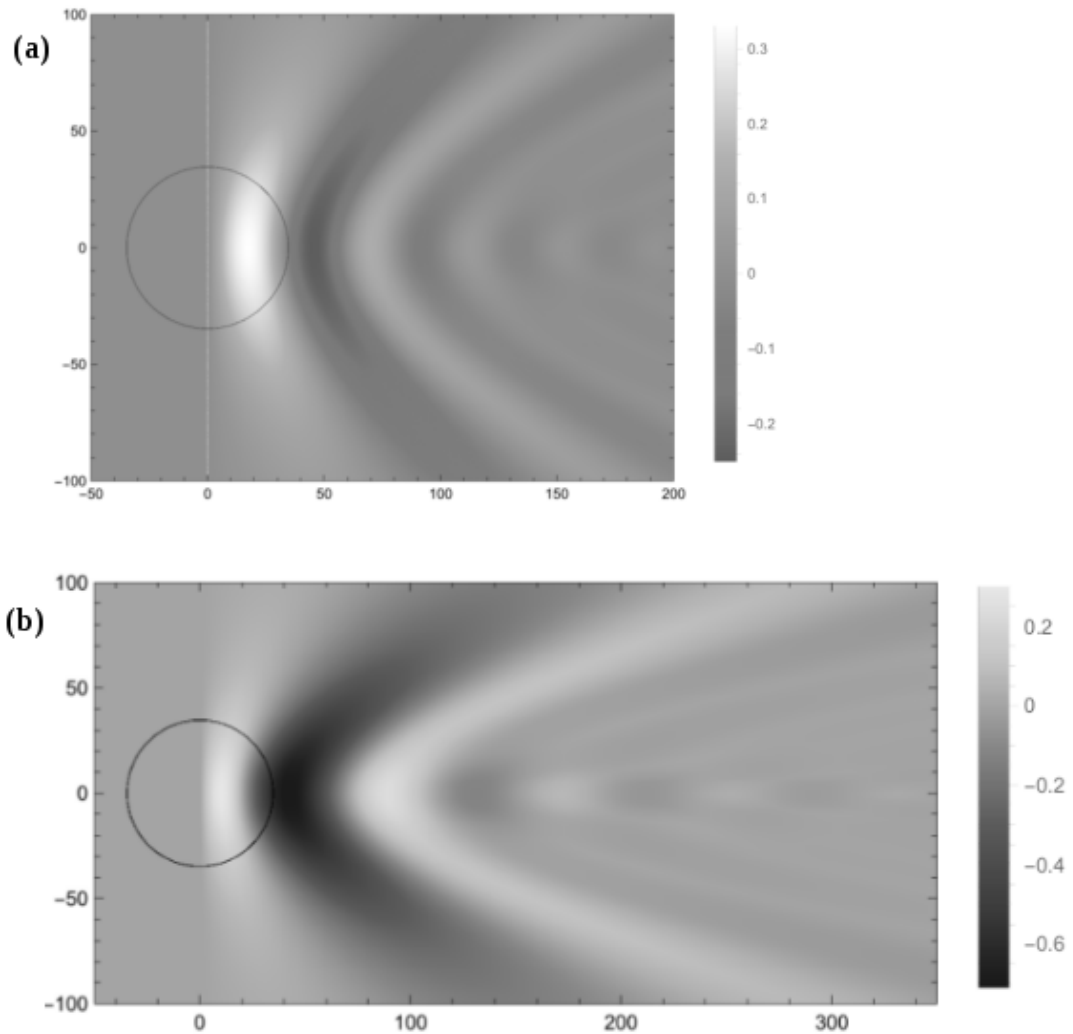


Figure 6.4.2: Perturbation velocity component u (stream-wise) for (a) $U_0 = 3$ cm/s and (b) $U_0 = 6$ cm/s, calculated by Dr. Bruno Voisin for our experimental configuration using his linear theory for stratified, non-rotating flow over a sphere presented in Voisin (2007).

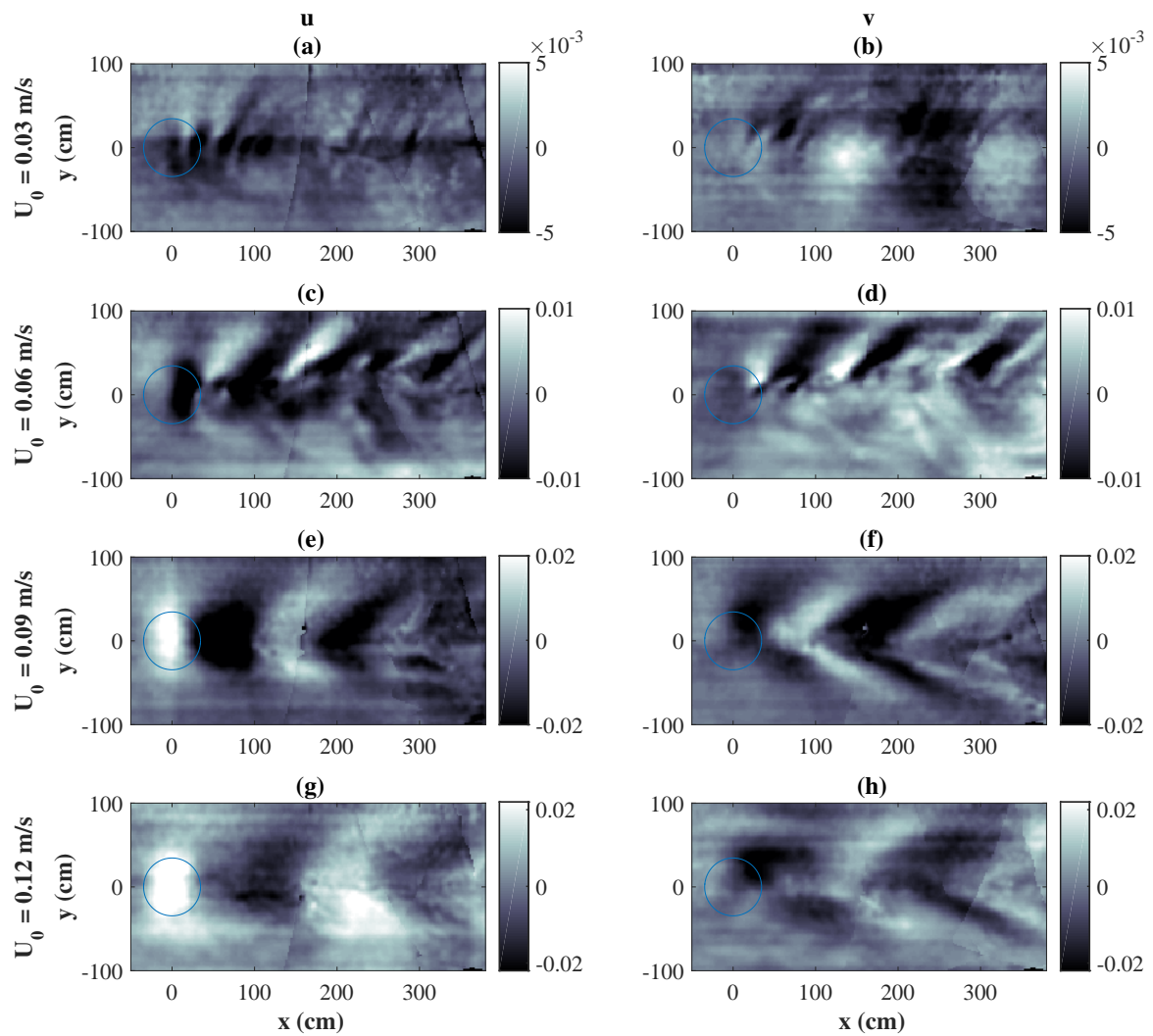


Figure 6.4.3: Same as in figure 6.4.1 but for experiments A2-D2 (with rotation).

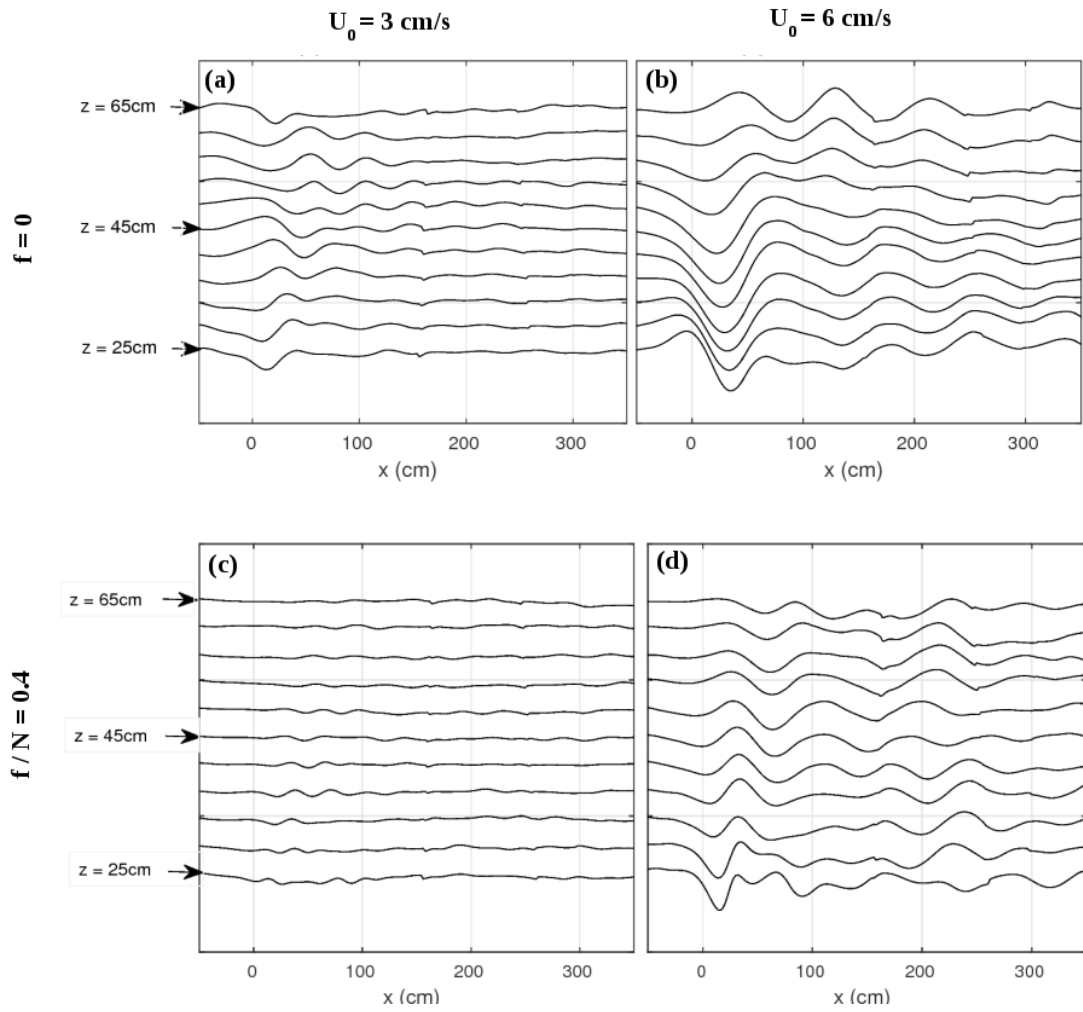


Figure 6.4.4: Profiles of the stream-wise velocity component along x at different levels z , for $U_0 = 3 \text{ cm/s}$ (left) and $U_0 = 6 \text{ cm/s}$ (right), with $f = 0$ (top) and $f/N = 0.4$ (bottom). The time t is ranging from 300 s to 570 s from top to bottom. The velocity is averaged in the range $y = -17$ to $+17 \text{ cm}$. Curves are shifted by 1 cm/s to distinguish the different levels.

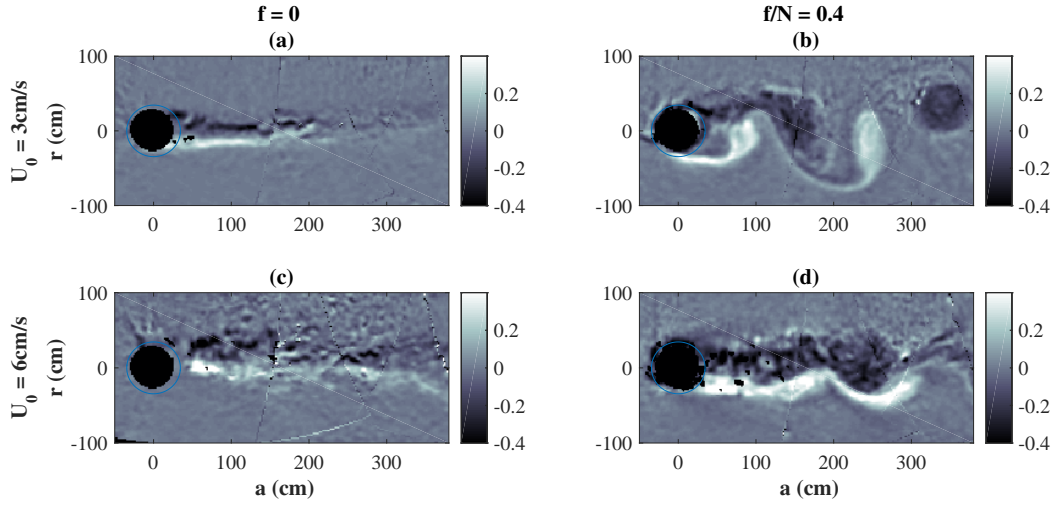


Figure 6.4.5: The vertical vorticity component (in s^{-1}) in the wake region for the experiments (a) A1, (b) A2, (c) B1 and (d) B2, horizontal cut at $z = 10$ cm, time $t = 400$ s.

wise velocities at different heights for experiments with $U_0 = 3$ cm/s and $U_0 = 6$ cm/s are shown in figure 6.4.4 for rotating and non-rotating cases.

The principal wavelength of the lee wave can be calculated from the distance between the two first minima on the stream-wise velocity profiles at $y = 0$. The calculated wavelengths for all the experiments with single cap are shown in table 6.4.1. We can see that the wavelengths increase with the increase in Froude number. This increase can be partly explained by the widening of the cap of height h_s which effectively emits the wave, according to the dividing streamline argument. Its diameter d_s is also shown in the tables 6.4.1.

However the ratio λ/d_s also increases with the Froude number, which shows that nonlinear effects are at stake. For the highest Froude numbers, a turbulent wake is produced over a height around $h = 20$ cm behind the obstacle and the wave emission occurs at the interface of this wake rather than at the obstacle itself. The intrinsic frequency $\omega \approx (2\pi/\lambda)U_0$ can also be calculated from the wavelength and is shown in the tables. The calculated values of ω are found to be close to N for each of the experiments, so that their wave vectors are close to horizontal. The angle θ of the wave-vector with respect to the horizontal, obtained by the dispersion relation $\omega/N = \cos \theta$, is also displayed in table 6.4.1.

6.4.2 WAKE OF EDDIES

According to the Froude number of the flow, the part of the cap below the dividing streamline height h_s blocks the mean flow and forces the mean flow to go around the cap. This results in a wake laterally delimited by two bands of opposite vorticity. The wake of eddies can be seen for the lower Froude numbers (for $U_0 = 3$ cm/s and $U_0 = 6$ cm/s), and they are shown in

figure 6.4.5 for the non-rotating and rotating cases. For the mean velocities of $U_0 = 9$ cm/s and $U_0 = 12$ cm/s, the part of the cap that is below the dividing streamlines are too small ($h - h_s = 1.3$ cm and 0 cm, respectively) to produce an effective wake of eddies.

In the absence of rotation (left hand side), the wake is fairly straight. By contrast, the background rotation favours a flow organisation into a Karman vortex street (right hand side) with periodic shedding of coherent vortices. The Strouhal number $S = f_s d_m / U_0$ can be calculated from the measured shedding frequency f_s and the obstacle diameter $d_m = 54$ cm taken at $z = 10$ cm, mid-height of the cap. With this definition we find that $S = 0.20$ for both cases $U_0 = 3$ cm/s and $U_0 = 6$ cm/s, which corresponds to the usual vortex shedding in the wake of a cylinder. For higher values of the velocity, $Fr > 1$, the periodic shedding disappears. Then the dividing streamline reaches the tank bottom $z = 0$, so that the whole obstacle height is involved in wave emission, with no remaining quasi two dimensional layer vortex shedding.

6.4.3 MULTIPLE CAPS EXPERIMENTS AND INDUCED DRAG

The experiments with multiple caps were performed in order to study the effect of topographic drag in the Antarctic Circumpolar Current. Eighteen identical spherical caps were placed in the arrangement shown in figure 6.3.2. Lee waves and vortices shed by each cap interact in a complex way, and we here discuss the global effect on the mean flow. We measured the mean stream-wise velocity in a domain 1×1 m² centered at $y = 0$ and $x = 3$ m, about 2 m away from the last row of caps to avoid local effects. The decay of the mean stream-wise velocity at different levels z for experiments B1-4 ($U_0 = 6$ cm/s) is shown in figure 6.4.6.

We can notice that the decay of the mean velocity for a single cap without background rotation is negligible for the duration of our experiment. However, with the addition of background rotation, a single cap can induce enough drag to reduce the mean velocity by about one-third in the duration of the experiment (900 s = 27 inertial periods). We also notice that the bottom friction effect influences throughout the water column with similar decay at each level.

For the cases with multiple caps, in the absence of rotation (bottom, left hand side in figure 6.4.6), the velocity is observed to decay at the lowest level $z = 10$ cm first, then to the levels $z = 13$ and 15 cm. The flow remains quasi-unchanged above the topography top, so the bottom friction effect hardly penetrates upward. The behaviour with background rotation is different (bottom, right hand side in figure 6.4.6), with a similar decay at each level at least in the early stage up to $t = 300$ s, showing that the bottom friction is efficiently transferred to the whole water column. An exponential decay time $\tau = 500$ s can be deduced from the plot. The decay however stalls in the upper layers in the late stage ($t > 300$ s).

It has been shown by Nikurashin and Ferrari (2010) that the internal waves generated by the topography can produce low frequency inertial oscillations through nonlinear interactions, and the inertial oscillations thus produced create a background shear that facilitates

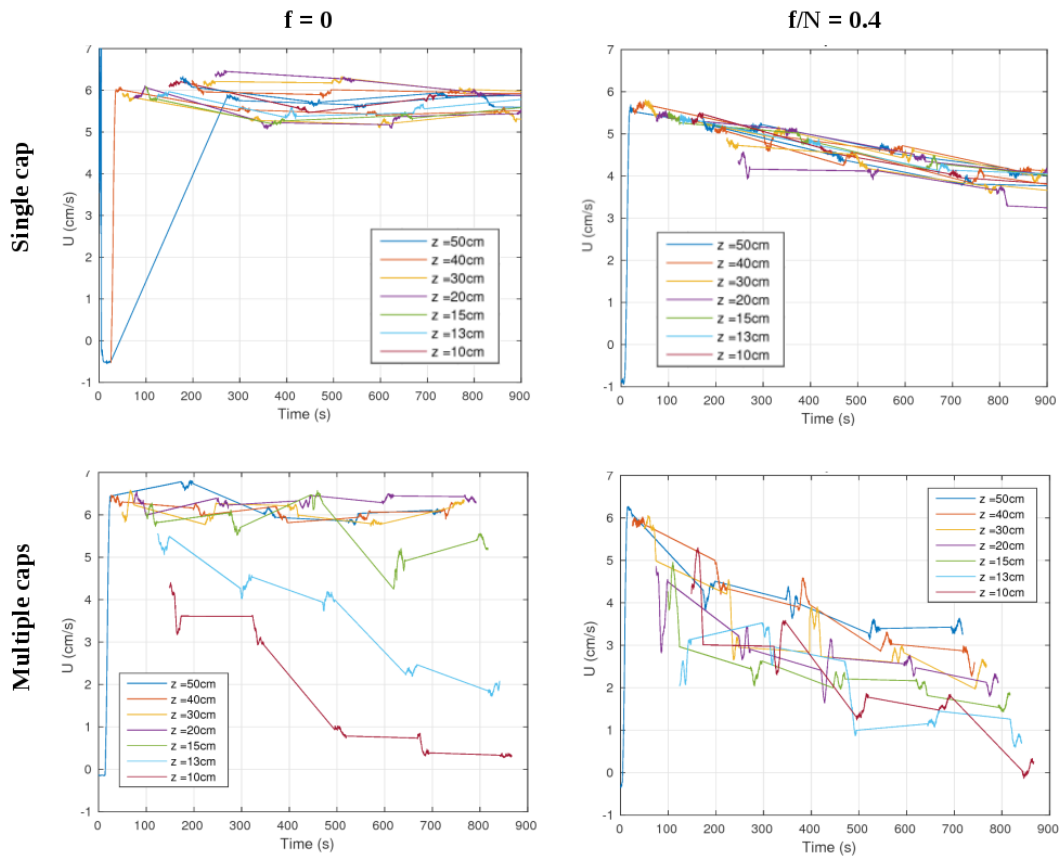


Figure 6.4.6: Decay of the mean stream-wise velocity in the experiments B1-4 ($U_0 = 6$ cm/s). The velocity is averaged in the range $y = [-0.5 \ 0.5]$ m and $x = [2.5 \ 3.5]$ m. At each level z , the curve is made of discontinuous set of time series measured when the laser sheet is positioned at this level, joined by straight lines.

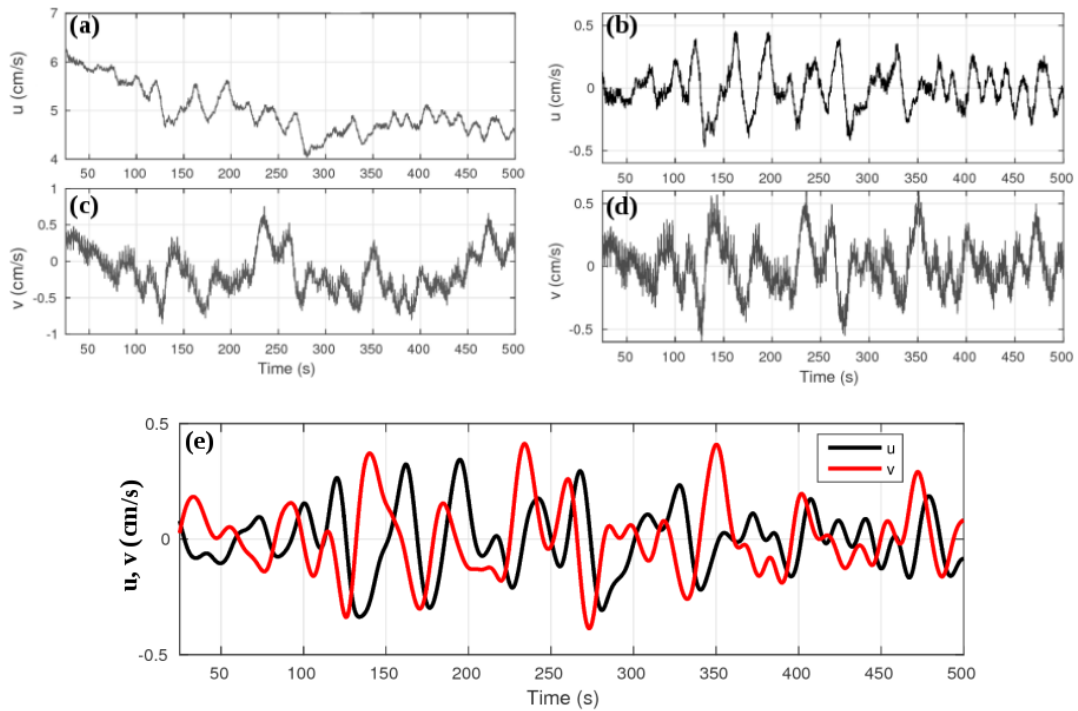


Figure 6.4.7: (a) Mean stream-wise velocity and (c) mean cross-stream velocity with time, in experiment B4 (multiple caps, with rotation and $U_0 = 6$ cm/s), measured at level $z = 60$ cm, averaged in the range $y = [-0.5 \ 0.5]$ m and $x = [2.5 \ 3.5]$ m. (b) Stream-wise velocity oscillations in experiment B4 at level $z = 60$ cm, obtained from the original signal after removing the linear trend of the mean velocity decay. (d) Cross-stream velocity oscillations at level $z = 60$ cm. (e) Stream-wise and cross-stream velocity oscillations filtered around the inertial frequency $f/(2\pi)$.

enhanced wave breaking.

Figure 6.4.7 shows the the stream-wise and cross-stream velocities in the experiment B4 (multiple caps, with rotation and $U_0 = 6$ cm/s). The mean velocities are shown in figures 6.4.7 (a) and (c). We can notice that the velocity decays for $t < 300$ s, and then remains more or less constant. Low frequency oscillations develop over the main decay as shown in figure 6.4.7 (b) and (d). Those contain a significant contribution of inertial oscillations, with amplitude about 0.25 cm/s.

The velocities of inertial oscillations are extracted in the figure of the figure 6.4.7 (e) using band-pass filtering of the signals (velocity components averaged in the 1×1 m² domain) around the inertial frequency $f/(2\pi)$ Hz. The two velocity components oscillate in quadrature with u in advance of a quarter period with respect to v , as expected for inertial oscillations.

6.5 CONCLUSIONS

The purpose of our experiment is to model the Antarctic Circumpolar Current in the laboratory and understand the topographic effects on the current. We modelled the ACC in the Coriolis rotating platform and introduced spherical caps as bottom topographies. Experiments were done with a single cap and multiple caps with and without background rotation for different values of Froude numbers.

Internal lee waves are emitted from the top part of the spherical cap while the bottom part makes the flow go around the cap creating a wake of eddies. The dividing streamline height is given by $h_c = R(1 - Fr)$ where R is the radius of curvature of the spherical cap. We notice that for lower Froude numbers the wake of eddies are clearly visible in the bottom part of the cap (below the dividing streamline) where as for higher Froude numbers it is not (dividing streamline height is below the cap height). This is in agreement with previous studies of stratified flow over an obstacle. For the rotating case, the lee waves emitted from a single cap are asymmetric with respect to the stream-wise axis.

The linear theory of Voisin (2007) was adapted to the case of a spherical cap. The results from the theory match well with the experimental observations for lee waves emitted from a single cap without background rotation. Further work is being done by Bruno Voisin and others at LEGI to make a better quantitative comparison.

The wake of the cap in the lower levels (below the dividing streamline) are characterised by a symmetric vortex dipole in the non-rotating case. In the case with rotation, vortex shedding was observed as a result of viscous boundary layer separation at the lee of the spherical cap. The decay of the mean flow was observed to be negligible for a single cap without rotation, while with rotation there is uniform decay at all levels for a single cap.

In the experiments with multiple caps, the internal waves from each cap are thought to interact and break. In the cases with background rotation, the nonlinear interactions of the internal waves generate inertial oscillations which further enhances wave breaking. The mean flow in the experiments with multiple caps decay just at the lower levels in the absence of

background rotation, whereas with background rotation, the decay is uniform throughout the fluid column. However, with background rotation, the decay rates drop at higher levels later in time, indicating the release of momentum by breaking lee waves at those levels.

One of the fundamental question in Southern Ocean dynamics is how the internal waves generated by the mean flow over the ocean topography transport momentum vertically and influence the mean flow itself. The present experiment was done only with horizontal laser sheets and hence we could not quantify the vertical momentum flux. Further experiments are being planned in LEGI with velocity measurements in a vertical plane, that will help in getting a clearer picture of the vertical transport of momentum. Three-dimensional numerical simulations are also underway in LEGI to study this problem in more detail.

7

Denouement

INTERNAL WAVES IN OCEANS play an important role by facilitating mixing and transport of energy and momentum over large distances. In spite of its importance in ocean dynamics, there are still many unanswered questions related to the physics of internal waves. In this thesis, we studied mainly one of those questions namely, the reflection of internal wave beams. Apart from the reflection, the last chapter of the thesis also describes the laboratory modelling of Antarctic Circumpolar Current to study the generation of lee waves over a three-dimensional topography.

The generation of internal waves in oceans and its role in ocean dynamics was explained briefly in the introduction (chapter 1). The importance of understanding the physics of internal waves and various ways in which internal waves are studied in a laboratory are also mentioned in that chapter, laying out the context of this thesis.

The interaction of internal waves with ocean bottom topography is an important process with varied dynamic importance in the ocean. Internal waves play a major role in promoting mixing in the ocean. A major share of the various physical processes affecting the interaction and dissipation of internal waves in deep ocean are close to the ocean bottom topography. Nonlinear interactions among internal waves facilitate the energy cascade from large scales to smaller scales and promote mixing. Nonlinear resonant interactions are one of the ways in which internal waves steepen and ultimately break to induce mixing. Many of these processes have a chance of occurring when internal waves interact with the bottom topography. The reflection of internal waves on the topography is one of those processes that facilitate nonlinear wave-wave interactions that can lead to energy transfers across scales. Reflection of internal waves from boundaries creates higher harmonics which can interact resonantly with the primary waves leading to energy cascade from the primary waves.

In chapter 3, we saw the nonlinear reflection of a finite-width internal gravity wave incident on a uniform slope, away from critical incidence, in a two-dimensional vertical plane. The reflection of a train of internal gravity waves on a slope, the generation of higher harmonics and the resonant interactions between the harmonics were discussed by Thorpe (1987). We revisit the theory of Thorpe (1987) in the presence of background rotation and apply it to a wave beam. The theoretical predictions are verified using numerical simulations. In the theory of Thorpe (1987), the amplitude of the second-order stream function resulting from the interaction of the incident and reflected waves is expressed as an indeterminate form at resonance. We show that the indeterminacy at resonance can actually be waived and that the amplitude of the second-order stream function is a linear function of the distance from the slope. It is therefore unbounded for a plane wave of infinite extent. We also showed that rotation does not qualitatively change the results obtained in the non rotating case. Numerical simulations of an incident wave of finite width were thus performed without background rotation to estimate the validity of the weakly nonlinear theory.

The reflection of internal wave beams in a two-dimensional vertical plane has been well studied and still is a hot topic of research. Our analysis is an extension of the theory presented by Thorpe (1987). Yet, we haven't included fluid viscosity in our model. This can be an interesting work for the future. We have used a free-slip boundary condition on the reflecting slope. The effect of bottom boundary layer when the slope has no-slip boundary condition on the resonant interactions can also be worth investigating. Indeed, the presence of a third dimension modifies the interaction process between the incident and reflected waves, even for normal incidence to the slope. However, for internal wave beams with very long lateral extent behaves like a two-dimensional (in vertical plane) wave beam.

Chapter 4 describes the reflection of a three-dimensional internal wave beam of finite lateral width. Results from laboratory experiment and three-dimensional numerical simulations were used to study the reflection. The initial purpose of the laboratory experiment was to investigate the resonant interactions among the wave and higher harmonics as predicted by Thorpe (1987). However, the laboratory experiment revealed that for the wave amplitude used, the reflected wave and the second harmonic wave are considerably weaker compared to the incident wave, and there is a strong induced mean flow (contrary to the predictions of Thorpe (1987)) in the interaction region which refracts the incident wave beam and leads it to break at the slope. The results of the experiment were published in Grisouard (2010), however, the generation of the strong mean flow was a mystery. Later, more experiments and three-dimensional numerical simulations were done to investigate further by Grisouard et al. (2013) and found that a finite-width (in lateral direction) internal wave beam induced a recirculating (in the horizontal plane) Eulerian mean flow. Bordes et al. (2012) have also performed laboratory experiments and found that a propagating internal wave beam of finite lateral extent produces a strong horizontally recirculating mean flow even before reflection. Kataoka and Akylas (2015) used asymptotic analysis to derive a coupled set of equations to model this recirculating mean flow induced by an internal wave beam.

We have used results from the experiment presented in Grisouard (2010) and Grisouard

et al. (2013), and performed numerical simulations with various wave beam widths, wave amplitudes and fluid viscosities to understand the wave induced mean flow. We find that the strong mean flow found in the interaction region in the experiments is a combination of two mean flow structures namely, a spatially periodic Eulerian mean flow (as predicted by Thorpe (1987)) and a growing jet-like mean flow. The former is produced by the nonlinear interaction between the incident and reflected wave beam and does not grow in time. The latter is forced by wave-wave interaction of a single wave beam as found in the studies of Bordes et al. (2012) and Kataoka and Akylas (2015), and grows in time, eventually dominating the spatially periodic mean flow. The wave-wave interaction that forces the jet-like mean flow is caused by lateral spatial variations in the wave field due to the diffraction of the wave beam in the horizontal plane (this is evident from the equations of Kataoka and Akylas (2015) too). The effects of lateral width of the wave beam, wave amplitude and fluid viscosity were also discussed. We performed an energy budget of the process to estimate the flux of energy from the incident wave to the mean flow and higher harmonics. These results are also described in the chapter.

The effect of background rotation on the reflection of a finite width internal wave beam is discussed in chapter 5. Numerical simulations with four different Coriolis frequencies were performed to study the influence of Coriolis force on the generation of mean flow. The angle of propagation of the wave beam was kept constant (same as the cases in chapter 4) in all those simulations by varying the wave frequency accordingly, so that the geometry of the reflection is the same. We found that the mean flow is diminished with the presence of background rotation. In the presence of background rotation, the zonal momentum is deflected by the Coriolis force to lateral direction in order to force wave motions in that direction. The forcing of lateral wave motions decreases the forcing of the induced mean flow. We also performed the energy budget and found that most of the energy of the incident wave is dissipated in the domain with only very little (less than 10%) transfer to the mean flow or higher harmonics.

The three-dimensional internal wave beams have gathered attention only recently. Therefore, there are still many questions remaining on their dynamics. Three-dimensional instabilities of internal wave beams are being investigated by Kataoka and Akylas (2016). The theory proposed by Kataoka and Akylas (2015) are being extended to the case with background rotation by Fan and Akylas (2016) and Fan et al. (2017). The author of the present thesis is also collaborating with Felix Beckebanze, Utrecht University in deriving a steady state solution for the wave induced mean flow. The effect of background rotation should be investigated in more detail too, with further theoretical analysis.

In chapter 6, the laboratory experiment to model the Antarctic Circumpolar Current is described. The experiment was performed in the Coriolis platform at LEGI in order to study the interaction of a mean current on a mountain (spherical cap) with and without background rotation. We observed the generation of lee waves from the top part of the spherical cap and a wake of eddies from the bottom part, in agreement with previous studies of stratified rotating flow over an obstacle. However, we found that with increase of the mean flow velocity, the attached boundary layer on the spherical cap increases the essential size of the obstacle

leading to increase in the wavelength of emitted lee waves. In the case with rotation, the generated lee waves are observed to be asymmetric in lateral direction and in the wake of eddies, vortex shedding was observed as a result of viscous boundary layer separation at the lee of the spherical cap. We also performed experiments with several spherical caps to study the drag caused by a random topography on ACC. We find that in the absence of background rotation, the mean flow decay just at the lower levels whereas with background rotation, the decay is uniform throughout the fluid column.

The physics of Antarctic Circumpolar Current has a very high significance in ocean dynamics. The experiments we performed measured only velocity fields in a horizontal plane. This makes it difficult to observe vertical transport of momentum by the waves. More laboratory experiments and three-dimensional numerical simulations are being planned at LEGI to further study these processes.

A1

NHM model

Non-hydrostatic Ocean model for the Earth Simulator (NHOES) was initially written by Nori Aiki (Nagoya University, Japan). A prototype of the model was used by Nori Aiki in [Aiki and Yamagata \(2004\)](#) and [Aiki et al. \(2006\)](#). Later, Bach Lien Hua and Sylvie Le Gentil (IFREMER, France) made significant improvements in its visualisations and user interface. The model is based on MITgcm albeit with some key differences. NHOES has two versions, NHM (Non-hydrostatic ocean Model) and NRM (Non-hydrostatic Rectangular ocean Model). For the results presented in this thesis, we have been using NHM.

The basic formulation is based on non-hydrostatic, incompressible Boussinesq equations discretised with Arakawa's C-grid as presented in [Marshall et al. \(1997\)](#). Some of the differences of NHM with MITgcm (as given in the README file of NHM) are:

- parallelisation is the first priority in coding
- non-hydrostatic pressure is solved by a bi-conjugate gradient stabilised method (BiCGSTAB2)
- free sea surface solved by splitting external/internal modes
- vector-invariant form is adopted for momentum equations
- a leap-frog scheme is used for time integrations
- three-dimensional biharmonic operator for the subgrid-scale mixing
- all binary output (snapshot and restart files) can be done in either the NetCDF or GrADS format
- Flux Corrected Transport scheme for the advection of passive tracers

- horizontal grids are in generalised curvilinear coordinates
- bottom topography can be represented by the partial step scheme

The main program file is `nh_main.F90`. It calls for different routines defined in other files for defining constants, setting up the grid and the topography, allocating memory for various variables, initialising the variables and beginning the time marching cycle.

The following are the variables solved in the model.

u,v,w	velocities in x, y and z axes
T	passive tracer (equal to density ρ)
p_{hy}	hydrostatic pressure
p_{nh}	non-hydrostatic pressure
p_s	surface pressure

The equations solved and the corresponding files where it is solved in the source code are given below.

$$\frac{\partial T}{\partial t} = \underbrace{-u \frac{\partial T}{\partial x} - v \frac{\partial T}{\partial y} - w \frac{\partial T}{\partial z}}_{\text{tracer updated in nh_next_tracer.F90}} + F^T \quad (\text{A1.1})$$

see `nh_fctf.F90`

where F^T is a forcing term on the tracer advection equation.

$$\underbrace{\rho = T}_{\text{see nh_density.F90}} \quad (\text{A1.2})$$

$$\underbrace{p_{hy} = \frac{g}{\rho_0} \int_z^0 (\rho - \rho_0) dz}_{\text{set in nh_hydrostatic.F90}} \quad (\text{A1.3})$$

$$\frac{\partial u}{\partial t} = -\frac{\partial p_{nh}}{\partial x} - \frac{\partial p_s}{\partial x} - \underbrace{\frac{\partial p_{hy}}{\partial x} - u \frac{\partial u}{\partial x} - v \frac{\partial u}{\partial y} - w \frac{\partial u}{\partial z} + fv + F^u}_{=G_u \text{ set in nh_momentum.F90 before moving to equation A1.7}} \quad (\text{A1.4})$$

set in `nh_vorticity.F90`

after executing equation A1.7, velocity updated in `nh_next_velocity.F90`, before moving to equation A1.8

where F^u is a forcing term on x-momentum equation.

$$\frac{\partial v}{\partial t} = -\frac{\partial p_{nh}}{\partial y} - \frac{\partial p_s}{\partial y} - \underbrace{\frac{\partial p_{hy}}{\partial y} - u \frac{\partial v}{\partial x} - v \frac{\partial v}{\partial y} - w \frac{\partial v}{\partial z} - fu + F^v}_{=G_v \text{ set in nh_momentum.F90 before moving to equation A1.7}} \quad (\text{A1.5})$$

after executing equation A1.7, velocity updated in nh_next_velocity.F90, before moving to equation A1.8

where F^v is a forcing term on y-momentum equation.

$$\frac{\partial w}{\partial t} = -\frac{\partial p_{nh}}{\partial z} - \underbrace{-u \frac{\partial w}{\partial x} - v \frac{\partial w}{\partial y} - w \frac{\partial w}{\partial z} + F^w}_{=G_w \text{ set in nh_momentum.F90 before moving to equation A1.7}} \quad (\text{A1.6})$$

not solved when USE_CONTI is turned on, except that G_w is used in equation A1.7

where F^w is a forcing term on z-momentum equation.

$$\left(\frac{\partial^2}{\partial x^2} + \frac{\partial^2}{\partial y^2} \right) (p_{nh} + p_s) + \frac{\partial^2}{\partial z^2} p_{nh} = \underbrace{\frac{\partial}{\partial x} G_u + \frac{\partial}{\partial y} G_v + \frac{\partial}{\partial z} G_w}_{\text{set in nh_poisson.F90}} \quad (\text{A1.7})$$

solved in nh_scg.F90 before moving to the time stepping part of equations A1.4 and A1.5

$$w = -\frac{\partial}{\partial x} \left(\int_{-H_b}^z u dz \right) - \frac{\partial}{\partial y} \left(\int_{-H_b}^z v dz \right) \quad (\text{A1.8})$$

set in nh_incompressible.F90 when USE_CONTI is turned on

References

- Aiki, H., Takahashi, K., and Yamagata, T. (2006). The red sea outflow regulated by the indian monsoon. *Continental Shelf Research*, 26(12):1448–1468.
- Aiki, H. and Yamagata, T. (2004). A numerical study on the successive formation of meddy like lenses. *J. Geophys. Res.*, 109:(C6).
- Alford, M. H. (2003a). Improved global maps and 54-year history of wind-work on ocean inertial motions. *Geophysical Research Letters*, 30:1424.
- Alford, M. H. (2003b). Redistribution of energy available for ocean mixing by long range propagation of internal waves. *Nature*, 423:159–162.
- Baines, P. G. (1982). On internal tide generation models. *Deep-Sea Res.*, 29:307–338.
- Baines, P. G. (1998). *Topographic effects in stratified flows*. Cambridge University Press.
- Bell, T. H. (1975a). Lee waves in stratified flows with simple harmonic time dependence. *J. Fluid Mech.*, 67:705–722.
- Bell, T. H. (1975b). Topographically generated internal waves in the open ocean. *J. Geophys. Res.*, 80:320–327.
- Benielli, D. and Sommeria, J. (1998). Excitation and breaking of internal gravity waves by parametric instability. *Journal of Fluid Mechanics*, 374:117–144.
- Bordes, G., Venaille, A., Joubaud, S., Odier, P., and Dauxois, T. (2012). Experimental observation of a strong mean flow induced by internal gravity waves. *Physics of Fluids*, 24:086602.
- Boyer, D., Davies, P., Holland, W., Biolley, F., and Honji, H. (1987). Stratified rotating flow over and around isolated three-dimensional topography. *Philosophical Transactions of the Royal Society of London A: Mathematical, Physical and Engineering Sciences*, 322(1564):213–241.
- Brandt, A. and Rottier, J. (2015). The internal wavefield generated by a towed sphere at low froude number. *Journal of Fluid Mechanics*, 769:103–129.

-
- Bretherton, F. P. (1969a). Momentum transport by gravity waves. *Quarterly Journal of the Royal Meteorological Society*, 95(404):213–243.
- Bretherton, F. P. (1969b). On the mean motion induced by internal gravity waves. *J. Fluid Mech.*, 36:785–803.
- Brighton, P. (1978). Strongly stratified flow past three-dimensional obstacles. *Quarterly Journal of the Royal Meteorological Society*, 104(440):289–307.
- Bühler, O. and Jacobson, T. E. (2001). Wave-driven currents and vortex dynamics on barred beaches. *J. Fluid Mech.*, 449:313–339.
- Cacchione, D., Pratson, L. F., and Ogston, A. (2002). The shaping of continental slopes by internal tides. *Science*, 296(5568):724–727.
- Cacchione, D. and Wunsch, C. (1974). Experimental study of internal waves over a slope. *J. Fluid Mech.*, 66:223–239.
- Chalamalla, V. K., Gayen, B., Scotti, A., and Sarkar, S. (2013). Turbulence during the reflection of internal gravity waves at critical and near-critical slopes. *J. Fluid Mech.*, 729:47–68.
- Dalziel, S. B., Patterson, M. D., Caulfield, C. P., and Brun, S. L. (2011). The structure of low-froude-number lee waves over an isolated obstacle. *Journal of Fluid Mechanics*, 689:3–31.
- Dauxois, T., Joubaud, S., Odier, P., and Venaille, A. (2017). Instabilities of internal gravity wave beams. *arXiv preprint arXiv:1702.07762*.
- Dauxois, T. and Young, W. R. (1999). Near-critical reflection of internal waves. *J. Fluid Mech.*, 390:271–295.
- d’Hieres, G. C., Davies, P., and Didelle, H. (1989). A laboratory study of the lift forces on a moving solid obstacle in a rotating fluid. *Dynamics of atmospheres and oceans*, 13(1-2):47–75.
- Donohue, K., Tracey, K., Watts, D., Chidichimo, M., and Chereskin, T. (2016). Mean antarctic circumpolar current transport measured in drake passage. *Geophysical Research Letters*.
- Drazin, P. G. (1961). On the steady flow of a fluid of variable density past an obstacle. *Tellus*, 13(2):239–251.
- Echeverri, P., Flynn, M., Winters, K. B., and Peacock, T. (2009). Low-mode internal tide generation by topography: an experimental and numerical investigation. *Journal of Fluid Mechanics*, 636:91–108.
- Egbert, G. and Erofeeva, S. (2014). Mapping m2 internal tides using a data-assimilative reduced gravity mode. In *AGU Fall Meeting Abstracts*.

- Egbert, G. and Ray, R. (2000). Significant dissipation of tidal energy in the deep ocean inferred from satellite altimeter data. *Nature*, 405:775–778.
- Egbert, G. D. (1997). Tidal data inversion: Interpolation and inference. *Progress in Oceanography*, 40(1):53–80.
- Ekman, V. W. (1904). On dead water. norw. n. polar exped. 1893-1896. Sci Results, XV, Christiana, Ph.D. thesis.
- Eriksen, C. C. (1982). Observation of internal waves reflection off sloping bottom. *J. Geophysical Research*, 87:525–538.
- Eriksen, C. C. (1998). Internal wave reflection and mixing at fieberling guyot. *Journal of Geophysical Research: Oceans*, 103(C2):2977–2994.
- Etling, D. (1989). On atmospheric vortex streets in the wake of large islands. *Meteorology and Atmospheric Physics*, 41(3):157–164.
- Etling, D. (1990). Mesoscale vortex shedding from large islands: a comparison with laboratory experiments of rotating stratified flows. *Meteorology and Atmospheric Physics*, 43(1-4):145–151.
- Fan, B. and Akylas, T. (2016). Effect of background rotation on the evolution of 3d internal gravity wave beams. In *APS Meeting Abstracts*.
- Fan, B. et al. (2017). *On three-dimensional internal wavepackets, beams, and mean flows in a stratified fluid*. PhD thesis, Massachusetts Institute of Technology.
- Garabato, A. C. N., Polzin, K. L., King, B. A., Heywood, K. J., and Visbeck, M. (2004a). Widespread intense turbulent mixing in the southern ocean. *Science*, 303(5655):210–213.
- Garabato, N., Polzin, K. L., King, B. A., Heywood, K. J., and Visebeck, M. (2004b). Widespread intense turbulent mixing in the southern ocean. *Science*, 303:210–213.
- Garrett, C. and Kunze, E. (2007). Internal tide generation in the deep ocean. *Anu. Rev. Fluid Mech.*, 39:57–87.
- Gerkema, T. (2006). Internal-wave reflection from uniform slopes: higher harmonics and coriolis effects. *Nonlinear Processes in Geophysics*, 13(3):265.
- Gerkema, T. and Shrira, V. (2005a). Near-inertial waves on the “nontraditional” β plane. *Journal of Geophysical Research: Oceans*, 110(C1).
- Gerkema, T. and Shrira, V. I. (2005b). Near-inertial waves in the ocean: beyond the ‘traditional approximation’. *Journal of Fluid Mechanics*, 529:195–219.

-
- Gerkema, T. and Zimmerman, J. T. F. (2008). An introduction to internal waves. Lecture notes, Royal NIOZ, Texel.
- Görtler, H. (1943). Über eine schwingungserscheinung in flüssigkeiten mit stabiler dichteschichtung. *ZAMM-Journal of Applied Mathematics and Mechanics/Zeitschrift für Angewandte Mathematik und Mechanik*, 23(2):65–71.
- Gostiaux, L. (2006). *Étude expérimentale des ondes de gravité internes en présence de topographie. Émission, propagation, réflexion*. PhD thesis, Ecole normale supérieure de lyon-ENS LYON.
- Gostiaux, L., Dauxois, T., Didelle, H., Sommeria, J., and Viboud, S. (2006). Quantitative laboratory observations of internal wave reflections on ascending slopes. *Physics of Fluids*, 18:056602.
- Gostiaux, L., Didelle, H., Mercier, S., and Dauxois, T. (2007). A novel internal waves generator. *Experiments in Fluids*, 42:123–130.
- Greenslade, M. (2000). Drag on a sphere moving horizontally in a stratified fluid. *Journal of Fluid Mechanics*, 418:339–350.
- Gregg, M. (1998). Estimation and geography of diapycnal mixing in the stratified ocean. *Physical processes in lakes and oceans*, pages 305–338.
- Grisouard, N. (2010). *Réflexions et réfractions non linéaires d'ondes internes de gravité*. PhD thesis, PhD thesis (in French), University of Grenoble, France.
- Grisouard, N., Leclair, M., Gostiaux, L., and Staquet, C. (2013). Large scale energy transfer from an internal gravity wave reflecting on a simple slope. *IUTAM Symposium Procedia*, 8:119–128.
- Helland-Hansen, B. and Nansen, F. (1909). The norwegian sea, its physical oceanography. based on the norwegian researches 1900-1904. Technical Report 390, Report on Norwegian fishery and marine-investigations, vol. 2, Bergen, Norway.
- Hopfinger, E., Flor, J.-B., Chomaz, J.-M., and Bonneton, P. (1991). Internal waves generated by a moving sphere and its wake in a stratified fluid. *Experiments in Fluids*, 11(4):255–261.
- Hosegood, P. and van Haren, H. (2004). Near-bed solibores over the continental slope in the faeroe-shetland channel. *Deep Sea Research Part II: Topical Studies in Oceanography*, 51(25):2943–2971.
- Hunt, J. C. R. and Snyder, W. H. (1980). Experiments on stably and neutrally stratified flow over a model three-dimensional hill. *J. Fluid Mech.*, 96:671–704.

- Javam, A., Imberger, J., and Armfield, S. W. (2000). Numerical study of internal wave-wave interactions in a stratified fluid. *J. Fluid Mech.*, 415:65–87.
- Kataoka, T. and Akylas, T. (2013). Stability of internal gravity wave beams to three-dimensional modulations. *Journal of Fluid Mechanics*, 736:67–90.
- Kataoka, T. and Akylas, T. (2015). On three-dimensional internal gravity wave beams and induced large-scale mean flows. *J. Fluid Mech.*, 769:621–634.
- Kataoka, T. and Akylas, T. (2016). Three-dimensional instability of internal gravity wave beams. In *VIIIth International Symposium on Stratified Flows*, volume 1.
- Lamb, K. (2004). Nonlinear interaction among internal wave beams generated by tidal flow over supercritical topography. *Geophysical Research Letters*, 31(9).
- Ledwell, J. R., Watson, A. J., and Law, C. S. (1993). Evidence for slow mixing across the pycnocline from an open-ocean tracer-release experiment. *Nature*, 364:701–703.
- Lefauve, A., Muller, C., and Melet, A. (2015). A three-dimensional map of tidal dissipation over abyssal hills. *Journal of Geophysical Research: Oceans*, 120(7):4760–4777.
- Lighthill, M. J. (1978). *Waves in Fluids*. Cambridge University Press.
- Longuet-Higgins, M. S. (1953). Mass transport in water waves. *Philosophical Transactions of the Royal Society of London A: Mathematical, Physical and Engineering Sciences*, 245(903):535–581.
- Longuet-Higgins, M. S. (1969). On the transport of mass by time-varying ocean currents. In *Deep Sea Research and Oceanographic Abstracts*, volume 16, pages 431–447. Elsevier.
- Longuet-Higgins, M. S. (1970). Longshore currents generated by obliquely incident sea waves: 1. *Journal of geophysical research*, 75(33):6778–6789.
- MacCready, P. (2014). Ocean science: Links between surface and abyss. *Nature Geoscience*, 7(8):554–555.
- Marshall, J., Adcroft, A., Hill, C., Perelman, L., and Heisey, C. (1997). A finite-volume, incompressible navier stokes model for studies of the ocean on parallel computers. *Journal of Geophysical Research: Oceans*, 102(C3):5753–5766.
- McPhee-Shaw, E. E. and Kunze, E. (2002). Boundary layer intrusions from a sloping bottom: A mechanism for generating intermediate nepheloid layers. *Journal of Geophysical Research: Oceans*, 107(C6).
- Mercier, M. J., Vasseur, R., and Dauvois, T. (2011). Resurrecting dead-water phenomenon. *Nonlinear Processes in Geophysics*, 18:193–208.

-
- Miles, J. W. and Huppert, H. E. (1968). Lee waves in a stratified flow. part 2. semi-circular obstacle. *Journal of Fluid Mechanics*, 33(4):803–814.
- Mowbray, D. and Rarity, B. (1967a). The internal wave pattern produced by a sphere moving vertically in a density stratified liquid. *Journal of Fluid Mechanics*, 30(3):489–495.
- Mowbray, D. and Rarity, B. (1967b). A theoretical and experimental investigation of the phase configuration of internal waves of small amplitude in a density stratified liquid. *Journal of Fluid Mechanics*, 28(1):1–16.
- Muller, P. and Briscoe, M. (2000). Diapycnal mixing and internal waves. *Oceanography*, 13:98–103.
- Muller, P., Holloway, G., Henyey, F., and Pomphrey, N. (1986). Nonlinear interactions among internal gravity waves. *Reviews of Geophysics*, 24:493–536.
- Munk, W. H. (1966). Abyssal recipes. *Deep-Sea Res.*, 2:361–376.
- Munk, W. H. and Wunsch, C. (1998). Abyssal recipes II : Energetics of tidal and wind mixing. *Deep-Sea Res.*, 45:1976–2009.
- New, A. (1988). Internal tidal mixing in the bay of biscay. *Deep Sea Research Part A. Oceanographic Research Papers*, 35(5):691–709.
- Nikurashin, M., Ferrai, R., Grisouard, N., and Polzin, K. (2014). The impact of finite-amplitude bottom topography on internal wave generation in the southern ocean. *Journal of Phys. Oceano.*, 44:2938–2950.
- Nikurashin, M. and Ferrari, R. (2010). Radiation and dissipation onf internal waves generated by geostrophic motions impinging on small scale topography: Theory. *Journal of Phys. Oceano.*, 40:1055–1074.
- Nikurashin, M. and Ferrari, R. (2011). Global energy conversion rate from geostrophic flows into internal lee waves in the deep ocean. *Geophysical Research Letters*, 38(8).
- Nikurashin, M. and Ferrari, R. (2013). Overturning circulation driven by breaking internal waves in the deep ocean. *Geophysical Research Letters*, 40(12):3133–3137.
- Nikurashin, M., Vallis, G. K., and Adcroft, A. (2013). Routes to energy dissipation for geostrophic flows in the southern ocean. *Nature Geoscience*, 6(1):48–51.
- Nowlin, W. D. and Klinck, J. M. (1986). The physics of the antarctic circumpolar current. *Reviews of Geophysics*, 24(3):469–491.
- Orsi, A. H., Whitworth, T., and Nowlin, W. D. (1995). On the meridional extent and fronts of the antarctic circumpolar current. *Deep Sea Research Part I: Oceanographic Research Papers*, 42(5):641–673.

- Osborn, T. (1980). Estimates of the local rate of vertical diffusion from dissipation measurements. *Journal of Physical Oceanography*, 10(1):83–89.
- Pairaud, I., Staquet, C., Sommeria, J., and Mahdizadeh, M. M. (2010). Generation of harmonics and sub-harmonics from an internal tide in a uniformly stratified fluid: numerical and laboratory experiments. In *IUTAM Symposium on Turbulence in the Atmosphere and Oceans*, pages 51–62. Springer.
- Peacock, T. and Weidman, P. (2005). The effect of rotation on conical wave beams in a stratified fluid. *Experiments in fluids*, 39(1):32–37.
- Phillips, O. M. (1966). *Dynamics of the upper ocean*. Cambridge University Press.
- Pingree, R. and New, A. (1989). Downward propagation of internal tidal energy into the bay of biscay. *Deep Sea Research Part A. Oceanographic Research Papers*, 36(5):735–758.
- Pingree, R. and New, A. (1991). Abyssal penetration and bottom reflection of internal tidal energy in the bay of biscay. *Journal of Physical Oceanography*, 21(1):28–39.
- Polzin, K. L., Toole, J. M., Ledwell, J. R., and Schmitt, R. W. (1997). Spatial variability of turbulent mixing in the abyssal ocean. *Science*, 276:93–96.
- Polzin, K. L., Toole, J. M., and Schmitt, R. W. (1995). Fine scale parametrizations of turbulent dissipation. *Journal of Phys. Oceano.*, 25:306–328.
- Richards, K., Smeed, D., Hopfinger, E., and d’Hières, G. C. (1992). Boundary-layer separation of rotating flows past surface-mounted obstacles. *Journal of Fluid Mechanics*, 237:343–371.
- Rodenborn, B., Kiefer, D., Zhang, H. P., and Swinney, H. L. (2011). Harmonic generation by reflecting internal waves. *Physics of Fluids*, 23:026601.
- Scales, J. A. and Snieder, R. (1999). What is a wave? *Nature.*, 401:739–740.
- Schär, C. and Durran, D. R. (1997). Vortex formation and vortex shedding in continuously stratified flows past isolated topography. *Journal of the atmospheric sciences*, 54(4):534–554.
- Scorer, R. (1949). Theory of waves in the lee of mountains. *Quarterly Journal of the Royal Meteorological Society*, 75(323):41–56.
- Scott, R., Goff, J., Naveira Garabato, A., and Nurser, A. (2011). Global rate and spectral characteristics of internal gravity wave generation by geostrophic flow over topography. *Journal of Geophysical Research: Oceans*, 116(C9).
- Sheppard, P. (1956). Airflow over mountains. *Quarterly journal of the Royal Meteorological society*, 82(354):528–529.

-
- Sloyan, B. M. (2005). Spatial variability of mixing in the southern ocean. *Geophys. Res. Lett.*, 32:L18603.
- St. Laurent, L., Naveira Garabato, A. C., Ledwell, J. R., Thurnherr, A. M., Toole, J. M., and Watson, A. J. (2012). Turbulence and diapycnal mixing in drake passage. *Journal of Physical Oceanography*, 42(12):2143–2152.
- Staquet, C. and Sommeria, J. (2002). Internal gravity waves: From instabilities to turbulence. *Annu. Rev. Fluid Mech.*, 34:559–593.
- Stocker, T., Qin, D., Plattner, G.-K., Alexander, L., Allen, S., Bindoff, N., Bréon, F.-M., Church, J., Cubasch, U., Emori, S., Forster, P., Friedlingstein, P., Gillett, N., Gregory, J., Hartmann, D., Jansen, E., Kirtman, B., Knutti, R., Kumar, K. K., Lemke, P., Marotzke, J., Masson-Delmotte, V., Meehl, G., Mokhov, I., Piao, S., Ramaswamy, V., Randall, D., Rhein, M., Rojas, M., Sabine, C., Shindell, D., Talley, L., Vaughan, D., and Xie, S.-P. (2013). Technical summary. in: *Climate change 2013: The physical science basis. contribution of working group I to the fifth assessment report of the intergovernmental panel on climate change. Technical report*, Cambridge University Press, Cambridge, United Kingdom and New York, NY, USA.
- Sutherland, B. R. (2001). Finite-amplitude internal wavepacket dispersion and breaking. *Journal of Fluid Mechanics*, 429:343–380.
- Sutherland, B. R. (2010). *Internal gravity waves*. Cambridge University Press.
- Tabaei, A. and Akylas, T. (2003). Nonlinear internal gravity wave beams. *Journal of Fluid Mechanics*, 482:141–161.
- Tabaei, A., Akylas, T. R., and Lamb, K. G. (2005). Nonlinear effects in reflecting and colliding internal wave beams. *J. Fluid Mech.*, 526:217–243.
- Teoh, S. G., Ivey, G. N., and Imberger, J. (1997). Laboratory study of the interaction between two internal wave rays. *J. Fluid Mech.*, 336:91–122.
- Thorpe, S. (2000). The effects of rotation on the nonlinear reflection of internal waves from a slope. *Journal of physical oceanography*, 30(8):1901–1909.
- Thorpe, S. (2001). On the reflection of internal wave groups from sloping topography. *Journal of physical oceanography*, 31(10):3121–3126.
- Thorpe, S. A. (1968). On the shape of progressive internal waves. *Philosophical Transactions of the Royal Society of London A: Mathematical, Physical and Engineering Sciences*, 263(1145):563–614.
- Thorpe, S. A. (1975). The excitation, dissipation and interaction of internal waves in the deep ocean. *J. Geophys. Res.*, 80:328–338.

- Thorpe, S. A. (1987). On the reflection of a train of finite-amplitude internal waves from a uniform slope. *J. Fluid Mech.*, 178:279–302.
- Thorpe, S. A. (1997). On the interactions of internal waves reflecting from slopes. *J. Fluid Mech.*, 27:2072.
- Vallis, G. K. (2017). *Atmospheric and oceanic fluid dynamics*. Cambridge University Press.
- Voisin, B. (2007). Lee waves from a sphere in a stratified flow. *Journal of Fluid Mechanics*, 574:273–315.
- Vosper, S., Castro, I., Snyder, W., and Mobbs, S. (1999). Experimental studies of strongly stratified flow past three-dimensional orography. *Journal of Fluid Mechanics*, 390:223–249.
- Waterman, S., Naveira Garabato, A. C., and Polzin, K. L. (2013). Internal waves and turbulence in the antarctic circumpolar current. *Journal of Physical Oceanography*, 43(2):259–282.
- Whitworth III, T. (1983). Monitoring the transport of the antarctic circumpolar current at drake passage. *Journal of Physical Oceanography*, 13(11):2045–2057.
- Wunsch, C. (1998). The work done by the wind on the oceanic general circulation. *Journal of Physical Oceanography*, 28(11):2332–2340.
- Zhou, Q. and Diamessis, P. (2015). Lagrangian flows within reflecting internal waves at a horizontal free-slip surface. *Physics of Fluids*, 27:126601.